Springer Theses
Recognizing Outstanding Ph.D. Research

Lianwei Li

Studies on "Perfect" Hyperbranched Chains Free in Solution and Confined in a Cylindrical Pore

Springer

Springer Theses

Recognizing Outstanding Ph.D. Research

For further volumes:
http://www.springer.com/series/8790

Aims and Scope

The series "Springer Theses" brings together a selection of the very best Ph.D. theses from around the world and across the physical sciences. Nominated and endorsed by two recognized specialists, each published volume has been selected for its scientific excellence and the high impact of its contents for the pertinent field of research. For greater accessibility to non-specialists, the published versions include an extended introduction, as well as a foreword by the student's supervisor explaining the special relevance of the work for the field. As a whole, the series will provide a valuable resource both for newcomers to the research fields described, and for other scientists seeking detailed background information on special questions. Finally, it provides an accredited documentation of the valuable contributions made by today's younger generation of scientists.

Theses are accepted into the series by invited nomination only and must fulfill all of the following criteria

- They must be written in good English.
- The topic should fall within the confines of Chemistry, Physics, Earth Sciences, Engineering and related interdisciplinary fields such as Materials, Nanoscience, Chemical Engineering, Complex Systems and Biophysics.
- The work reported in the thesis must represent a significant scientific advance.
- If the thesis includes previously published material, permission to reproduce this must be gained from the respective copyright holder.
- They must have been examined and passed during the 12 months prior to nomination.
- Each thesis should include a foreword by the supervisor outlining the significance of its content.
- The theses should have a clearly defined structure including an introduction accessible to scientists not expert in that particular field.

Lianwei Li

Studies on "Perfect" Hyperbranched Chains Free in Solution and Confined in a Cylindrical Pore

Doctoral Thesis accepted by
University of Science and Technology of China,
Hefei, People's Republic of China

Springer

Author
Dr. Lianwei Li
Department of Chemistry
The University of Chicago
Chicago, IL
USA

Supervisor
Prof. Chi Wu
University of Science and Technology
of China
Hefei
People's Republic of China

ISSN 2190-5053 ISSN 2190-5061 (electronic)
ISBN 978-3-319-06096-5 ISBN 978-3-319-06097-2 (eBook)
DOI 10.1007/978-3-319-06097-2
Springer Cham Heidelberg New York Dordrecht London

Library of Congress Control Number: 2014935981

Printed on acid-free paper

Springer is part of Springer Science+Business Media (www.springer.com)

Parts of this thesis have been published in the following journal articles:

1. **Lianwei Li**,* Xu Wang, Jinxian Yang, Xiaodong Ye,* and Chi Wu, "Degradation Kinetics of Model Hyperbranched Chains with both Uniform Subchains and Controlled Location of Cleavable Disulfide Linkages", *Macromolecules* **2014**, *47*, 650.
2. **Lianwei Li**,* Xu Wang, Chen He, and Weidong He,* "Association, Emulsifying and Solubilization Properties of Amphiphilic Hyperbranched Poly(acrylic acid) Grafted with Polystyrene (HB-PAA-*g*-PS)", *J. Polym. Sci., Polym. Chem.* **2013**, *52*, 128.
3. **Lianwei Li**,* Yuyuan Lu,* Lijia An, and Chi Wu, "Experimental and Theoretical Studies of Scaling of Sizes and Intrinsic Viscosity of Hyperbranched Chains in Good Solvents", *J. Chem. Phys.* **2013**, *138*, 114908.
4. Chi Wu,* and **Lianwei Li**, "Unified Description of Transportation of Polymer Chains with Different Topologies through a Small Cylindrical Pore", *Polymer* **2013**, *54*, 1463. (Cover Story)
5. **Lianwei Li**,* Jianfeng Zhou, and Chi Wu, "Intrachain Folding and Interchain Association of Hyperbranched Chains with Long Uniform Subchains Made of Amphiphilic Diblock Copolymers", *Macromolecules* **2012**, *45*, 9391.
6. **Lianwei Li**, Chen He, Weidong He, and Chi Wu,* "How Does a Hyperbranched Chain Pass through a Nanopore?", *Macromolecules* **2012**, *45*, 7583.
7. Chen He, Weidong He,* **Lianwei Li**, Wenxing Jiang, Jing Tao, Jing Yang, Long Chen, Xuesong Ge, and Shengqi Chen, "Controlling the Formation of Long-Subchain Hyperbranched Polystyrene from Seesaw-Type AB_2 Macromonomers: Solvent Polarity and Solubility", *J. Polym. Sci., Polym. Chem.* **2012**, *50*, 3214.
8. **Lianwei Li**, Chen He, Weidong He,* and Chi Wu,* "Formation Kinetics and Scaling of "Defect-Free" Hyperbranched Polystyrene Chains with Uniform Subchains Prepared from Seesaw-type Macromonomers", *Macromolecules* **2011**, *44*, 8195.
9. Chen He, **Lianwei Li**, Weidong He,* and Chi Wu,* 'Click' Long Seesaw-Type A~~B~~A Chains Together into Huge Defect-Free Hyperbranched Polymer Chains with Uniform Subchains", *Macromolecules* **2011**, *44*, 6233.

(*: Corresponding author)

Supervisor's Foreword

This Ph.D. thesis study has solved a longstanding problem in polymer physics: "how does a hyperbranched chain pass through a cylindrical pore smaller than its size under an elongation flow field?" The question was asked by the Nobel Laureate, the late Prof. de Gennes in 1970s but has never been seriously addressed in real experiments. In order to answer this classic question, it started from the development of a novel polymerization strategy of using a seesaw-type A~~~~B~~~~A macromonomer to prepare a set of narrowly distributed "defect-free" hyperbranched chains with different overall molar masses and controllable uniform subchain lengthes.

Armed with these model hyperbranched chains, Dr. Lianwei Li has then unearthed how the critical (minimum) flow rate, at which a hyperbranched chain can pass through the pore, is dependent on the overall molar mass and the subchain length, which is different from the prediction made by the late Prof. de Gennes. The experimental results led to a unified description of polymer chains with different topologies passing through a small cylindrical pore, which enables us to separate polymer chains by their topologies instead of sizes in ultrafiltration. In addition, this thesis study also reveals how the chain structure of amphiphilic hyperbranched block and graft copolymers affect their solution properties, including the establishments of several classic scaling laws that relate the chain size and the intrinsic viscosity to the overall molar mass and the subchain length, respectively; the intrachain folding and the interchain association of hyperbranched chains as well as their emulsification ability, solubilization efficiency, and degradation behavior.

This thesis study is highly original and its results significantly deepen our understanding of hyperbranched polymers. It is not exaggerated to state that many results in this thesis will be classic. I am truly delighted and I feel very lucky to have Lianwei as one of my Ph.D. students because he was a highly self-motivated student and has the making of the first-class researcher. It was him who taught me something new during this thesis study. This thesis has paved a way for further developments of a range of analytical instruments that can separate and characterize polymer chains by their topologies instead of sizes.

Hefei, February 2014 Prof. Chi Wu

Acknowledgments

Many people contributed in different ways to this thesis and I express my gratitude to all of them. During the past 5 years in Hefei, I always enjoyed the great working environment, and the cooperative and fun atmosphere.

First of all, I want to thank my supervisor Prof. Chi Wu for giving me the opportunity to work in his group. Five years ago, when I knew nothing about polymer physics, I was lucky enough to get the opportunity to study in the best lab under the guidance of the best polymer physicist in USTC. It is his rigorous trainings, careful guidance, and strong support that enabled me to grow rapidly in research capacity and interest. Moreover, it is the private discussion with him that led me to rethink about my career aspiration and future direction. His unrestrained motivation and diligence for scientific research also impressed me deeply.

I am also especially indebted to Dr. Guangzhao Zhang, Dr. Weidong He, Dr. Fan Jin, Dr. Xiaodong Ye, and Dr. Guangming Liu for their vast experience, helpful discussion, continual support in my research work and daily life. I am also grateful to Miss Jing Sun and Miss Lu Liu who helped us to deal with a lot of laboratory chores and provided us an absolutely academic environment.

I especially treasure the opportunity to have met many wonderful colleagues who eventually became very close friends. I also want to give my sincere thanks to them because they are the source of my happiness in the past 5 years in Hefei.

Finally, I am also indebted to my family for their endless love and strong moral support during my pursuit of a higher degree. They are: Zhangming Li (father), Chunli Fan (mother), Luqing Zhang (grandpa), Wenzhen Ren (grandma), and Mo Zhu (wife). Without the constant and patient support of my loving family, none of this work could have taken place!

Hefei, October 2013 Dr. Lianwei Li

Contents

Chapter 1
Introduction and Background

1.1 Comparison Between Hyperbranched Polymers and Their Linear Analogues

Hyperbranched polymers have unique properties in solution, melt and bulk due to their branched and relatively compact structure in comparison with linear counterparts. Therefore, they have received much attention in the last few decades due to some potential applications in biomedicines, energy storages and polymer blends, to name but a few [1–5]. The highly branched and dense but irregular structure can also leads to excellent solubility, compared to linear polymers, low solution viscosity, modified melt rheology, and high level of terminal end group functionality [6].

It has been known that the molecular parameters, such as monomer nature, overall molar mass, polydispersity, branching degree and distribution of subchain lengths, strongly affect the final macroscopic properties of polymers. Therefore, great research interest has been paid to the synthesis of various well-defined polymers with different topologies, such as cyclic [7–13], star branched [14–16], mikto-star [17–19], and H-shaped [20, 21] polymers, and the study on their structure-property relationship. In contrast, to establish the structure-property relationship of hyperbranched polymers, a series of narrowly distributed samples (standards) with a well-defined structure have to be prepared before any possible study.

Compared with their analogues dendrimers or other polymer chains with simple chain topologies, hyperbranched polymers are usually prepared in a one-pot synthesis [22–27] and various properties of the prepared hyperbranched polymers generally have one common and significant characteristic of polydispersity, such as the overall molar mass, chain configuration and subchain length, which greatly hinders the preparation of appropriate hyperbranched samples and the corresponding study of the their structure-property correlation.

L. Li, *Studies on "Perfect" Hyperbranched Chains Free in Solution and Confined in a Cylindrical Pore*, Springer Theses, DOI: 10.1007/978-3-319-06097-2_1,

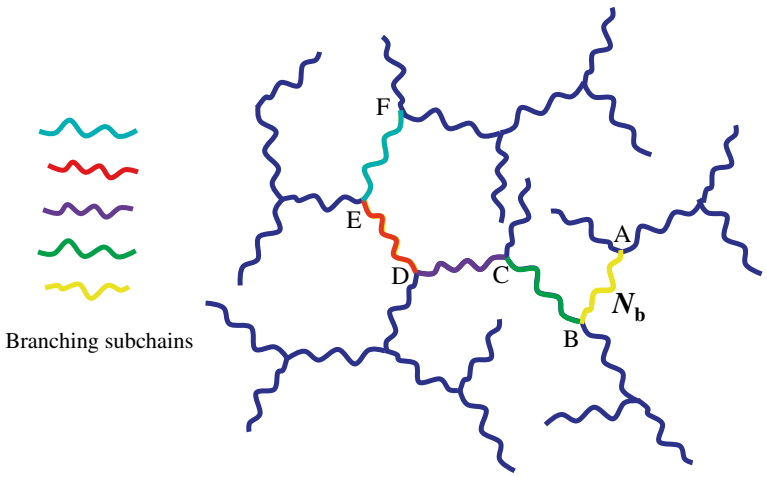

Fig. 1.1 Schematic illustration of a "perfect" hyperbranched chain, where *A*, *B*, *C*, *D*, *E*, and *F* represent different branching points, and N_b represents the degree of polymerization between neighboring branching points

1.2 What is a "Perfect" Hyperbranched Structure?

Before starting the study on the related structure-property relationship of hyperbranched polymers, an important question one has to answer is: *what is a "**perfect**" hyperbranched structure*? Note that for an ideal or the so-called "perfect" hyperbranched chain structure, it should have an identical number of strands that are connected onto each branching point, resulting in *uniform subchains* between *any two neighboring branching points* [28, 29]. As shown in Fig. 1.1, the branching subchain lengths between AB, BC, CD, DE and EF are completely equal. However, the preparation of such "perfect" hyperbranched polymers with uniform and long subchains is rather difficult if not impossible, which explains why only few related structure-property studies have been reported so far [30–32].

1.3 Structural Defects of the Resultant Hyperbranched Structures Prepared by Previous Synthetic Methods

Up to now, the synthetic methods for preparing hyperbranched polymers can be roughly divided into chain-growth- and step-growth-based polymerization methods. For chain-growth-based polymerization methods, hyperbranched polymers can be prepared by either self-condensing vinyl or ring-opening polymerization (SCVP [26, 33–36] and SCROP [37, 38]). In contrast, poly-condensation is used as the one of the most important step-growth-based polymerization methods

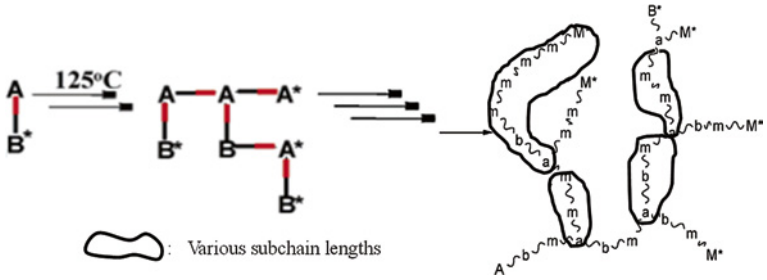

Fig. 1.2 Schematic of synthesis of hyperbranched polymers by SCVP or SCROP methods

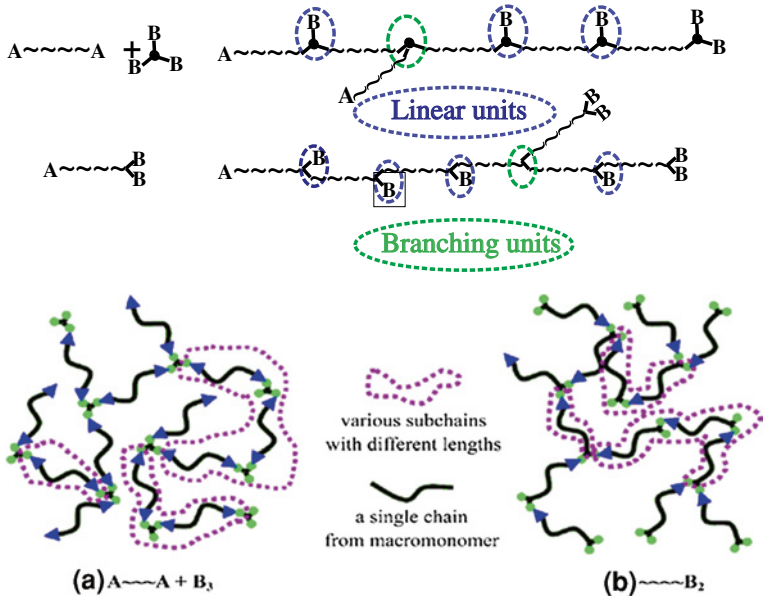

Fig. 1.3 Comparison of topological structures of a randomly branched chain and a hyperbranched chain prepared by using different types of macromonomers

[1, 23, 30–32, 39–56]. The SCVP initially reported by Fréchet et al. [57] is fairly versatile, in which hyperbranched chains are formed via polymerization of vinyl macromonomers with an initiating group. While in SCROP, a polymerizable cyclic group is used instead of a vinyl group. However, the hyperbranched structures prepared by these methods have one fatal structural defect, namely, an extremely broad distribution of the branching subchain length, as shown in Fig. 1.2.

As for step-growth-based polymerization methods, Fig. 1.3 shows two typical approaches in the preparation of hyperbranched chains: (A) co-polycondensation [49–56] and (B) self-polycondensation [1, 23, 30–32, 40–48]. The co-polycondensation

between A_2 and B_3 is one of the most well-known adopted synthetic strategies. However, as shown in Fig. 1.3, these two mostly used approaches unavoidably result in subchains with different lengths because of some unreacted B-groups; namely, each unreacted B group extends the subchain by one macromonomer length. In principle, the subchain length can range from one macromonomer length to infinity. Therefore, the hyperbranched structures prepared by those mentioned synthetic methods are not "perfect" due to the broad distribution of the subchain length.

1.4 Existing Important Issues for the Study on Hyperbranched Polymers

1.4.1 Difficulty in the Preparation of "Perfect" Hyperbranched Samples

As mentioned before, to clearly establish a structure-property relationship of hyperbranched polymers, one has to prepared at least two sets of narrowly distributed samples (standards); namely, in the first set, the hyperbranched samples should have a similar overall molar mass but different subchain lengths; and in the second set, the hyperbranched samples should have an identical subchain length but different overall molar masses, which are rather difficult in polymer chemistry. Preparing a series of "perfect" hyperbranched samples is *the first priority* before any possible structure-property study.

1.4.2 Does Hyperbranched Structure Still Hold the Fractal Nature?

It is well known that linear chain owns the simplest chain topology and the characteristic of self-similar objectives, namely, there exists a classical scaling law between the chain molar mass and chain size. Moreover, both theoretical and experimental studies have revealed that cyclic polymer is also fractal objective, just like linear chain [58].

It has been proved that, as analogues of hyperbranched polymers, dendrimer-like polymers are not a self-similar objective, i.e., the classic scaling laws between their sizes (R), intrinsic viscosities ($[\eta]$) and molar masses (M) are not valid for dendrimer-like polymers, which is partially because the hydrodynamic radius (R_h) is not proportional to the radius of gyration (R_g) [59–61]. There exists a maximum in the plot of $[\eta]$ versus M, i.e., $[\eta]$ first increases with the number of generation (G) and then decreases after G reaches a certain value, as shown in Fig. 1.4 [59].

However, whether such classical mass-size scaling law is valid or not for "perfect" hyperbranched chains, and how the subchain length and branching degree of hyperbranched chains affect such a mass-size scaling law are still uncertain. Note

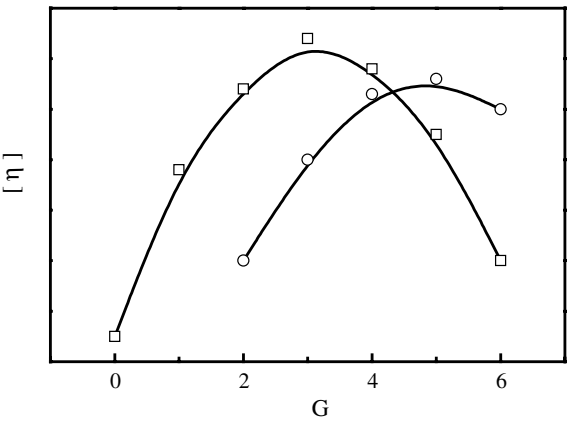

Fig. 1.4 Generation (G) dependence of intrinsic viscosity ([η]) of dendrimenrs [59]

that randomly hyperbranched chains are even more complicated than dendrimers, and to the best of our knowledge, the fractal nature of "perfect" hyperbranched polymers has not been theoretically or experimentally addressed so far.

On the other hand, even if we can prepare such "perfect" hyperbranched polymers, first one has to note that the accurate determination of the molecular parameters of these hyperbranched polymers is not a trivial task. Because of their densely branched structure, their overall molecular density is increased compared to their linear analogues in a good solvent, and the well-known method for the determination of the molar mass distribution of polymers, such as size exclusion chromatography (SEC) with differential refractive index detection (RI) or UV detection and subsequent calibration with a linear polymer standard, can lead to strong deviations from the actual values of molar mass. A comprehensive comparison between different interpretations of the SEC chromatograms of hyperbranched poly(etheramide) using polystyrene and poly(ethylene oxide) as a calibration standard, as well as the method of the universal calibration, has been carried out in order to find the best adequate method for processing the SEC results [62]. The comparison was made on the basis of the molar masses obtained by SEC coupled to RI and static light-scattering detector (MALLS, multi-angle laser light scattering), the combination of which is known to give absolute molar mass values also for complex macromolecular architectures. The deviations between the values obtained by these three methods are extremely high, as shown in Fig. 1.5. Even the data of universal calibration does not get close to the real molar mass values, although the intrinsic viscosity is incorporated into this calculation, taking into account the influence of the molecular density, according to the famous Flory-Fox viscosity equation [63, 64].

A more important one is that, it had been repeatedly overlooked that SEC separates polymer chains by their hydrodynamic volumes, not by their molar masses. Namely, for non-linear polymer chains, each retentive fraction in principle contains polymer chains with a similar hydrodynamic volume but not necessarily with a similar molar mass. Presumably, it is due to difficulties and limitations in both the sample preparation and experimental methods so that less attention has been paid to this very important point so far.

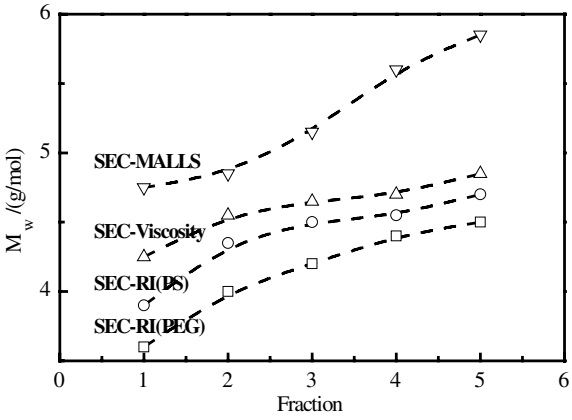

Fig. 1.5 Deviation of the molar mass values for hyperbranched poly (etheramide) determined by different SEC-interpretation methods: (*square*) SEC-RI detection and polyethylene oxide standard; (*cycle*) SEC-RI detection and polystyrene standard; (*triangle*) of-line SEC-viscosity detection and universal calibration; (*inverted triangle*) SEC-MALLS (static light-scattering detection) [62]

1.4.3 Hyperbranched Structure-Dependent Solution Properties

As we know, compared with di- or triblock copolymers, linear multiblock [65–70] copolymers generally have richer phase behavior and more excellent mechanical performance due to the stronger interchain entanglement and the formation of special "loop" structure [71, 72]. Generally, the possible phase behavior of amphiphilic linear multiblock chains in solution can be divided into single-chain folding, single-chain association, and multi-chain association states, as shown in Fig. 1.6. The final state of amphiphilic mutiblock chains mainly depend on the solvophobic/solvophilic balance, polymer concentration, solvent selectivity, and relative and absolute block lengths [65–70]. Experimentally, these three states have been recently successively observed by our group [73, 74] and Liu' group [75, 76].

Compared to linear multiblock copolymers, the study on the phase behavior of hyperbranched multiblock copolymers has received less attention due to the lack of model samples. To the best of our knowledge, only a handful of work reported the related results [44, 77]. Namely, Hutchings et al. comparatively studied the phase behaviour of hyperbranched block copolymer hyper-$(PS\text{-}PI)_n$ and its linear precursor PS-PI-PS [44]. The TEM results indicated that the tendency of phase separation was strongly suppressed by the branching structure, as shown in Fig. 1.7; unfortunately, the structure of the studied hyperbranched samples were still not as "perfect" as we defined before [44].

On the other hand, amphiphilic graft [78, 79] copolymers also present interesting phase behavior in solution. In the aspect of preparation of "star-like" or graft polymers, hyperbranched/dendritic chains are usually acted as a multi-sites

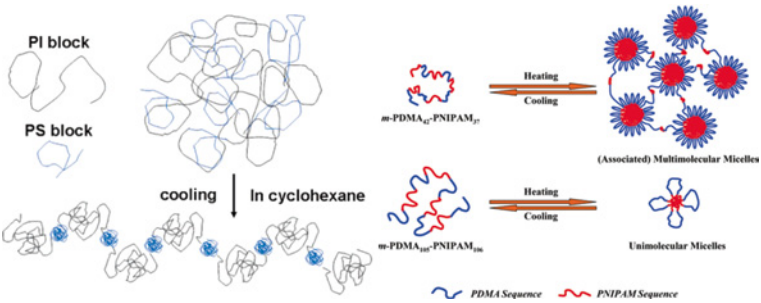

Fig. 1.6 Schematic illustration of three possible states of linear multiblock copolymer chains in a selective solvent: single-chain folding, single-chain association and multi-chain association

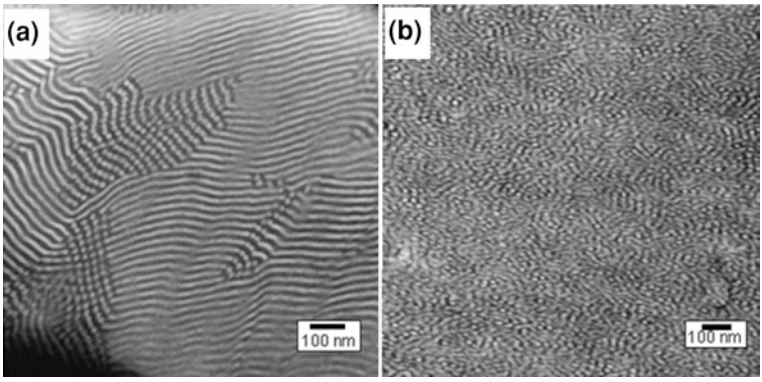

Fig. 1.7 Transmission electron micrographs (*TEM*) of (**a**) linear PS–PI–PS triblock copolymer (macromonomer) and (**b**) PS–PI–PS triblock copolymer HyperBlock [44]

functional core to produce grafting chains via "graft-onto" or "graft-from" strategy. However, the as-prepared "star-like" amphiphilic or double-hydrophobic/hydrophilic polymers are generally made of a very small core and much longer grafting chains, because the hyperbranched/dendritic cores are mainly prepared from small-molecular polymerizable monomer, instead of long polymer chains (macromonomers). [80–83] One can image that the hyperbranched topology, instead of star topology, will finally govern the physical properties of graft copolymers in solution if the branched core size is much larger than the grafting chain size.

Our group has been engaged in the solution properties of amphiphilic copolymers, especially for PS- and PAA-based amphiphilic polyelectrolytes for many years [84–89], and our previous results indicated the significant influence of the topological structure of amphiphilic polymer chains on their properties in dilute and semi-dilute solution. However, to our knowledge, there has been no theoretical or experimental study on how the phase behavior and solution properties of these novel amphiphilic hyperbranched block and graft copolymers are related to their topological structures, presumably also

because it is rather difficult, if not impossible, to prepare narrowly distributed "perfect" amphiphilic hyperbranched copolymer chains with well-defined and controllable subchain length and composition. Therefore, for amphiphilic hyperbranched block and graft copolymers, whether the branching effect can further improve relevent properties is still unknown and to be explored.

References

1. Hawker CJ, Chu F, Pomery PJ, Hill DJT (1996) Macromolecules 29:3831
2. Chen Y, Shen Z, Pastor-Pérez L, Frey H, Stiriba S-E (2004) Macromolecules 38:227
3. Liu CH, Gao C, Yan DY (2006) Macromolecules 39:8102
4. Cao Q, Liu P (2007) J Mater Sci 42:5661
5. Yang Y, Xie X, Yang Z, Wang X, Cui W, Yang J, Mai Y-W (2007) Macromolecules 40:5858
6. Voit BI, Lederer A (2009) Chem Rev 109:5924
7. Rique-Lurbet L, Schappacher M, Deffieux A (1994) Macromolecules 27:6318
8. Schappacher M, Deffieux A (1995) Macromolecules 28:2629
9. Benmouna M, Khaldi S, Bensafi A, Maschke U (1997) Macromolecules 30:1168
10. Tezuka Y, Komiya R, Washizuka M (2002) Macromolecules 36:12
11. Schulz M, Tanner S, Barqawi H, Binder WH (2010) J Polym Sci Pol Chem. 48:671
12. Xu J, Ye J, Liu S (2007) Macromolecules 40:9103
13. Lonsdale DE, Monteiro MJ (2010) Chem Commun 46:7945
14. Hietala S, Strandman S, Järvi P, Torkkeli M, Jankova K, Hvilsted S, Tenhu H (2009) Macromolecules 42:1726
15. Hietala S, Mononen P, Strandman S, Järvi P, Torkkeli M, Jankova K, Hvilsted S, Tenhu H (2007) Polymer 48:4087
16. Plummer R, Hill DJT, Whittaker AK (2006) Macromolecules 39:8379
17. Shi G-Y, Sun J-T, Pan C-Y (2011) Macromol Chem Phys 212:1305
18. Wu Z, Liang H, Lu J (2010) Macromolecules 43:5699
19. Khanna K, Varshney S, Kakkar A (2010) Macromolecules 43:5688
20. Pitet LM, Chamberlain BM, Hauser AW, Hillmyer MA (2010) Macromolecules 43:8018
21. Gungor E, Durmaz H, Hizal G, Tunca U (2008) J Polym Sci Pol Chem. 46:4459
22. Turner SR, Voit BI, Mourey TH (1993) Macromolecules 26:4617
23. Ghosh A, Banerjee S, Komber H, Lederer A, Häussler L, Voit B (2010) Macromolecules 43:2846
24. Scheel AJ, Komber H, Voit BI (2004) Macromol Rapid Comm 25:1175
25. Yang H, Xu J, Pispas S, Zhang G (2013) *RSC Advances*
26. Hawker CJ, Frechet JMJ, Grubbs RB, Dao J (1995) J Am Chem Soc 117:10763
27. Xu J (2009) Macromolecules 42:6893
28. Zimm BH, Stockmayer WH (1949) J Chem Phys. 17:1301
29. de Gennes PG (1968) Biopolymers 6:715
30. Trollsås M, Hedrick JL (1998) Macromolecules 31:4390
31. Choi J, Kwak S-Y (2003) Macromolecules 36:8630
32. Trollsas M, Kelly MA, Claesson H, Siemens R, Hedrick JL (1999) Macromolecules 32:4917
33. Peleshanko S, Gunawidjaja R, Petrash S, Tsukruk VV (2006) Macromolecules 39:4756
34. Tsarevsky NV, Huang J, Matyjaszewski K (2009) J Polym Sci Pol Chem. 47:6839
35. Wang W-J, Wang D, Li B-G, Zhu S (2010) Macromolecules 43:4062
36. Zhou Z, Yan D (2010) Sci China Chem 53:2429
37. Liu M, Vladimirov N, Fréchet JMJ (1999) Macromolecules 32:6881
38. Magnusson H, Malmström E, Hult A (1999) Macromol Rapid Comm 20:453
39. Konkolewicz D, Gray-Weale A, Perrier SB (2009) J Am Chem Soc 131:18075

40. Trollsas M, Atthoff B, Claesson H, Hedrick JL (1998) Macromolecules 31:3439
41. Zhu Z, Pan C (2007) Macromol Chem Phys 208:1274
42. Vanjinathan M, Shanavas A, Raghavan A, Nasar AS (2007) J Polym Sci Pol Chem 45:3877
43. Hutchings LR, Dodds JM, Roberts-Bleming SJ (2006) Macromol Symp 240:56
44. Hutchings LR (2008) Soft Matter 4:2150
45. Clarke N, Luca ED, Dodds JM, Kimani SM, Hutchings LR (2008) Eur Polym J 44:665
46. Hutchings LR, Dodds JM, Roberts-Bleming SJ (2005) Macromolecules 38:5970
47. Kong L-Z, Sun M, Qiao H-M, Pan C-Y (2010) J Polym Sci Pol Chem 48:454
48. Li J, Sun M, Bo Z (1084) J Polym Sci Pol Chem 2007:45
49. Adam M, Delsanti M, Munch JP, Durand DJ (1809) Physique Paris 1987:48
50. Unal S, Yilgor I, Yilgor E, Sheth JP, Wilkes GL, Long TE (2004) Macromolecules 37:7081
51. Unal S, Ozturk G, Sisson K, Long TE (2008) J Polym Sci Pol Chem 46:6285
52. Liu D, Zeng S, Hu Q, Yi C, Xu Z (2010) Polym Bull 64:877
53. Fornof AR, Glass TE, Long TE (2006) Macromol Chem Phys 207:1197
54. Oguz C, Unal S, Long TE, Gallivan MA (2007) Macromolecules 40:6529
55. Kong J, Schmalz T, Motz G, Müller AHE (2011) Macromolecules 44:1280
56. Emrick T, Chang H-T, Fréchet JMJ (1999) Macromolecules 32:6380
57. Fréchet JMJ, Henmi M, Gitsov I, Aoshima S, Leduc MR, Grubbs RB (1080) Science 1995:269
58. Takano A, Ohta Y, Masuoka K, Matsubara K, Nakano T, Hieno A, Itakura M, Takahashi K, Kinugasa S, Kawaguchi D, Takahashi Y, Matsushita Y (2011) Macromolecules 45:369
59. Mourey TH, Turner SR, Rubinstein M, Frechet JMJ, Hawker CJ, Wooley KL (1992) Macromolecules 25:2401
60. Lu YY, Shi TF, An LJ, Wang ZG (2012) Europhys Lett 97:64003
61. Lu Y, Shi T, An L, Jin L, Wang Z-G (2010) Soft Matter 6:2619
62. Lederer A, Voigt D, Clausnitzer C, Voit B (2002) J Chromatogr A 976:171
63. Rubinstein M, Colby RH (2003) Polymer Physics. Oxford University Press, New York
64. Teraoka I (2002) Polymer solutions: an introduction to physical properties. Wiley, New Jersey
65. Halperin A (1991) Macromolecules 24:1418
66. Spontak RJ, Fung JC, Braunfeld MB, Sedat JW, Agard DA, Ashraf A, Smith SD (1996) Macromolecules 29:2850
67. Hlavata D, Horak Z, Lednicky F, Hromadkova J, Pleska A, Zanevskii YV (2001) J Polym Sci Pol Phys 39:931
68. You YZ, Zhou QH, Manickam DS, Wan L, Mao GZ, Oupicky D (2007) Macromolecules 40:8617
69. Hugouvieux V, Axelos MAV, Kolb M (2008) Macromolecules 42:392
70. Hadjiantoniou NA, Krasia-Christoforou T, Loizou E, Porcar L, Patrickios CS (2010) Macromolecules 43:2713
71. Eastwood EA, Dadmun MD (2001) Macromolecules 34:740
72. Eastwood EA, Dadmun MD (2002) Macromolecules 35:5069
73. Hong L, Zhu F, Li J, Ngai T, Xie Z, Wu C (2008) Macromolecules 41:2219
74. Zhang Q (2008) Macromolecules 41:2228
75. Hu J, Ge Z, Zhou Y, Zhang Y, Liu S (2010) Macromolecules 43:5184
76. Ge Z, Zhou Y, Tong Z, Liu S (2011) Langmuir 27:1143
77. Konkolewicz D, Poon CK, Gray-Weale A, Perrier S (2010) Chem Commun 47:239
78. Chen H, Li J, Ding Y, Zhang G, Zhang Q, Wu C (2005) Macromolecules 38:4403
79. Hao J, Yuan G, He W, Cheng H, Han CC, Wu C (2002) Macromolecules 2010:43
80. Dworak A, Kowalczuk-Bleja A, Trzebicka B, Walach W (2002) Polym Bull 49:9
81. Kowalczuk-Bleja A, Sierocka B, Muszyński J, Trzebicka B, Dworak A (2005) Polymer 46:8555
82. Zhang C, Zhou Y, Liu Q, Li S, Perrier Sb, Zhao Y (2011) *Macromolecules 44:*2034
83. Kali G, Szesztay M, Bodor A, Iván B (2007) Macromol Chem Phys 208:1388
84. Hu T, Wu C (2001) Macromolecules 34:6802

85. Li L, Yang J, Zhou J (2013) Macromolecules 46:2808
86. Li L, Zhou J, Wu C (2012) Macromolecules 45:9391
87. Qiu X, Wu C (1997) Macromolecules 30:7921
88. Wu C, Qiu X (1998) Phys Rev Lett 80:620
89. Zhang G, Winnik FM, Wu C (2003) Phys Rev Lett 90:035506

Chapter 2
Our Main Goals

The core of this work lies on developing a novel Seesaw-type macromonomer strategy for the preparation of "perfect" hyperbranched model samples with uniform subchains and the investigation on their related solution properties. More specifically, the main goals of this work are as follows:

1. Through our well-designed Seesaw-type AB_2 macromonomer, prepare a series of Seesaw-type macromonomers and "perfect" hyperbranched homopolymers and copolymers with uniform and controllable subchain length.
2. Using various characterization methods, accurately determine the molecular parameters of the prepared narrowly distributed hyperbranched samples and clarify the fractal property of "perfect" hyperbranched polymers.
3. Investigate on the deformation property of "perfect" hyperbranched chains; more specifically, using our developed ultrafiltration technique to explore how the branching effect affects the critical flow which hyperbranched chains need to crawl through a cylindrical nanopore.
4. Study the solution behavior of amphiphilic hyperbranched block and graft copolymers, and answer how the branching effect affects their phase behavior in dilute and semidilute solutions.
5. Expand our Seesaw-type macromonomer strategy to the preparation of model hyperbranched hetero-subchain copolymers with two different controllable and uniform subchains and study how the chain parameters affect the related properties.
6. Prepare novel "perfect" degradable hyperbranched model samples with uniform subchains and controlled locations of cleavable disulfide linkages simultaneously; and elucidate how the branching effect affects their degradation property.

L. Li, *Studies on "Perfect" Hyperbranched Chains Free in Solution and Confined in a Cylindrical Pore*, Springer Theses, DOI: 10.1007/978-3-319-06097-2_2,

Chapter 3
Seesaw-Type Macromonomer Strategy: A Versatile Approach for the Preparation of "Perfect" Hyperbranched Polymers

In this chapter, we will mainly discuss our recently developed Seesaw-type macromonomer strategy and how to use this strategy to construct various Seesaw-type macromonomers [1–7]. The part of preparation of hyperbranched (co)polymers will be given in the next chapter.

3.1 Comparison Between Seesaw-Type Macromonomer Strategy and Other Synthetic Strategies

Figure 3.1 shows a typical schematic of structure comparison of Y-type and our Seesaw-type AB_2 macromonomers and the resultant hyperbranched polymers. As shown, instead of putting two reactive B groups on one end (Y-type), we attach them, respectively, at two ends of our macromonomer and move the reactive A group to the middle, i.e., a Seesaw-type B~~~~A~~~~B chain, where ~~~~ represents a polymer chain [6, 7]. Further using the condensation reaction between A and B groups from different macromonomers, large hyperbranched chain can be produced. In this way, each resultant hyperbranched chain, no matter how large it is, contains no more than one unreacted A group if it does not undergo an intrachain cyclization with one of B groups inside. During the self-polycondensation, macromonomers continuously react and add to the branched chain, finally leading to large hyperbranched chains with uniform subchains; and *the most important thing* is that each branching subchain is exactly made of *half a* macromonomer. For such formed large hyperbranched chains, one possible "defect" (self-looping) has nearly no effect on their properties. This is why we can still name them as "perfect" ones.

It should be emphasized that such formed chains are different from dendrimers. Previously, Hedrick et al. [8, 9] used this approach to synthesize hyperbranched chains, starting with short B~A~B oligomers containing 5–20 monomer units. Their resultant hyperbranched polymers are too small to be accurately characterized by laser light scattering (LLS), presumably because they used a relatively lower efficient esterification.

L. Li, *Studies on "Perfect" Hyperbranched Chains Free in Solution and Confined in a Cylindrical Pore*, Springer Theses, DOI: 10.1007/978-3-319-06097-2_3,

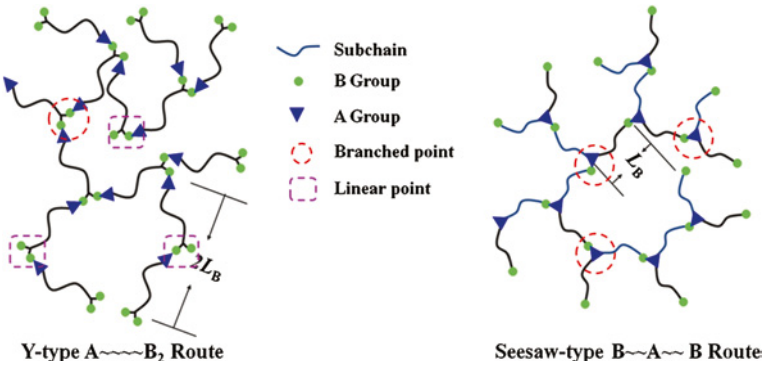

Fig. 3.1 Schematic of structure comparison of Y-type and Seesaw-type AB_2 macromonomer and the corresponding hyperbranched polymers

To the best of our knowledge, no one has tried to use such kind of Seesaw-type B~~~~A~~~~B chains to prepare "perfect" hyperbranched polymers with long and uniform subchains and seriously study their related properties.

3.2 Preparation of Seesaw-Type Macromonomers by Controlled/Living Polymerization

It should be mentioned that the type of Seesaw-type macromonomer is not only limited to homopolymer chains, but also can expand to copolymer chains if it is possible from the perspective of polymer chemistry, namely, the macromonomer can be homopolymer, triblock copolymer and diblock copolymer, as shown in Fig. 3.2.

In order to prepare various kinds of Seesaw-type macromonomers, we firstly synthesized two kinds of functional Seesaw-type initiators. Figure 3.3 shows how the functional initiators I and II are prepared. Their high purities were further confirmed by ^{1}H NMR characterization (Fig. 3.4). Initiator I was used to construct macromonomer homopolymers and triblock copolymers, and initiator II was used to construct macromonomer diblock copolymers, respectively. Using these two initiators, we have prepared a number of Seesaw-type macromonomer homopolymers and copolymers with different block components and lengths.

3.2.1 Preparation of Seesaw-Type Macromonomer Homopolymers

First, let's focus on the preparation of the simplest Seesaw-type macromonomer: polystyrene homopolymer (Fig. 3.5) [6, 7]. Using initiator I with one alkyne

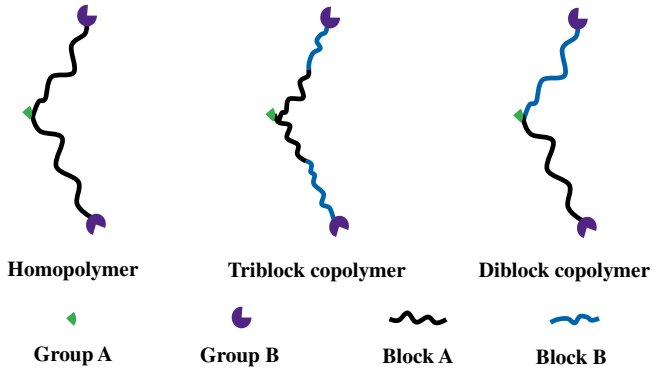

Fig. 3.2 Schematic illustration of three types of Seesaw-type macromonomers: homopolymer, triblock copolymer and diblock copolymer

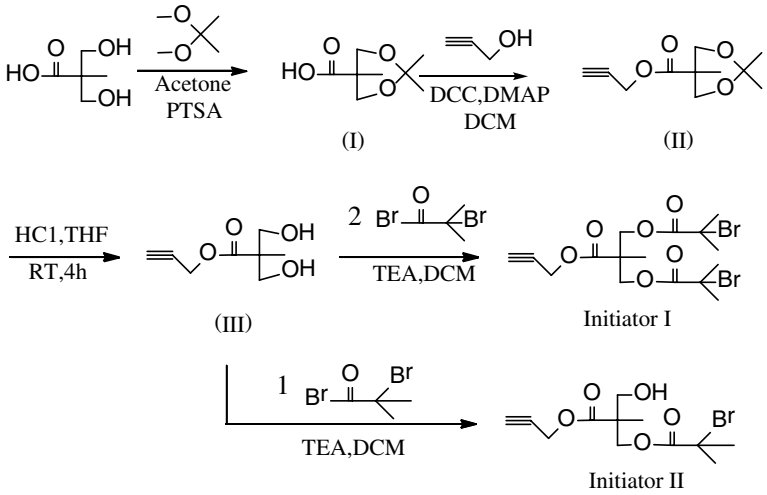

Fig. 3.3 Schematic synthesis of two kinds of Seesaw-type functional initiators

and two bromine groups, we successfully prepared and characterized a series of Seesaw-type polystyrene homopolymers with controlled chain lengths by a combination of the activators regenerated by electron transfer for atom transfer radical polymerization (ARGET ATRP) and azidation reaction. In our study, both normal ATRP and ARGET ATRP were tested. Initiator I was prepared and used as an initiator due to its high efficiency [10]. The two terminal bromo functional groups were converted to two azide end groups via their reaction with NaN_3 [11–13].

It has been known that chains with some highly reactive end-groups are required to prepare well-defined polymer materials made of telechelic or block chains. In ATRP, side reactions induced by outer sphere electron-transfer (OSET) not only reduce the functionality of polymer chains, but also limit the chain length

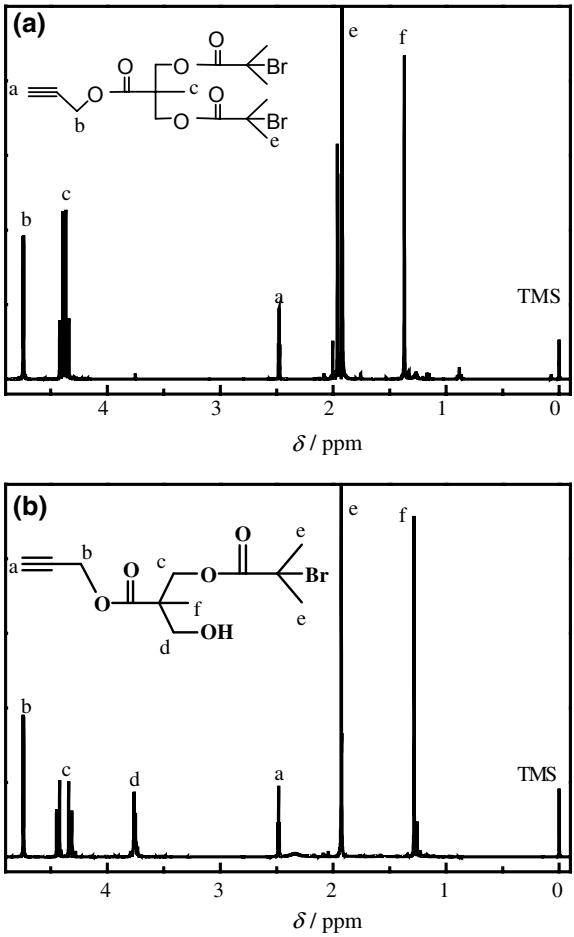

Fig. 3.4 ^{1}H NMR spectra of **a** Initiator I, and **b** Initiator II

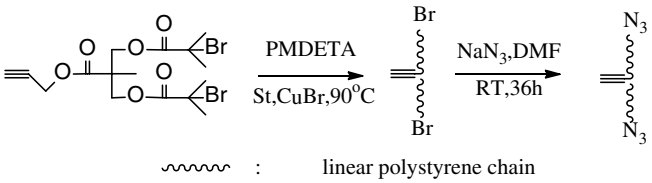

Fig. 3.5 Schematic synthesis of Seesaw-type macromonomer polystyrene homopolymer

attainable with some monomers [14–17]. Although much effort has been devoted to improving the end-group functionality of polymer chains synthesized by ATRP, the results reported in literatures were inconsistent. Datta et al. [17] found that poly(ethyl acrylate) made with bpy as a ligand contained more remaining bromine end-groups than that prepared with PMDETA. However, Matyjaszewski

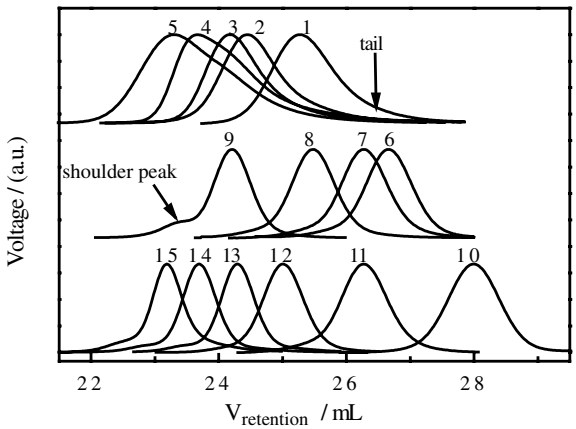

Fig. 3.6 SEC curves of linear polystyrene macromonomers prepared via ATRP using bpy, PMDETA, ME_6TREN as ligand, respectively, and *curve 1–5*, *6–9*, *10–15* correspond to entry *1–5*, *6–9*, *10–15* in Table 3.1

Table 3.1 Characterization of linear PSt prepared by normal and ARGET ATRP

Entry	Ligand	Molar ratios					M_n^c	M_w/M_n^c
		PBMP	St	CuBr	Ligand	$Sn(EH)_2$	g/mol	
1	bpy	1	500	2	4	0	1.32×10^4	1.22
2	bpy	1	1,000	2	4	0	2.33×10^4	1.25
3	bpy	1	1,000	2	4	0	2.71×10^4	1.27
4	bpy	1	1,000	2	4	0	3.38×10^4	1.35
5	bpy	1	1,000	2	4	0	4.36×10^4	1.46
6	PMDETA	1	500	2	2	0	5.80×10^3	1.08
7	PMDETA	1	500	2	2	0	7.90×10^3	1.09
8	PMDETA	1	500	2	2	0	1.43×10^4	1.09
9	PMDETA	1	1,000	2	2	0	3.71×10^4	1.13
10	ME_6TREN	1	100	0.1	1	1	3.30×10^3	1.07
11	ME_6TREN	1	200	0.1	1	1	7.60×10^3	1.09
12	ME_6TREN	1	300	0.1	1	1	1.87×10^4	1.13
13	ME_6TREN	1	500	0.1	1	1	3.10×10^4	1.11
14	ME_6TREN	1	1,000	0.1	1	1	4.50×10^4	1.13
15	ME_6TREN	1	1,000	0.1	1	1	6.21×10^4	1.15

[a] The polymerization temperature of Entry 1–5, 6–9, and 10–15 is 110, 90 and 90 ℃, respectively
[b] The polymerization of entry 1–9 and 10–15 was proceeding in bulk and in anisole (0.75 volume equiv. vs. monomer), respectively
[c] The number-average molar mass and molar mass distribution were determined by SEC on the basis of a conventional linear PSt calibration

et al. [14–16] showed that a more reducing catalytic system, such as PMDETA and Me_6TREN, could increase the chain end-group functionality. Here we compared the ATRP by using bpy, PMDETA and Me_6TREN, respectively, as a ligand.

The polymerization conditions and results are summarized in Fig. 3.6 and Table 3.1. All the results indicate that using CuBr-Me_6TREN-$Sn(EH)_2$ as a

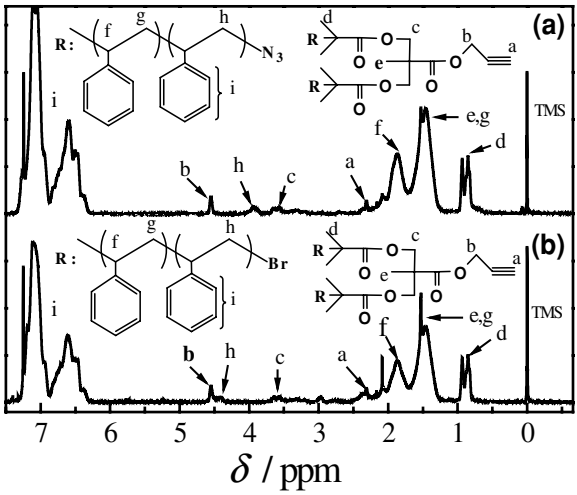

Fig. 3.7 Comparison of ^{1}H NMR spectra of **a** Alkyne-(PSt-azide)$_2$ and **b** Alkyne-(PSt-bromine)$_2$ (Entry 10 in Table 3.1)

catalyst, the polymerization is better controlled. When bpy is used as a ligand, the reaction temperature should be relatively higher because the CuBr-bpy complex has a higher redox potential than the CuBr-PMDETA and Cu-Me$_6$TREN complexes. The width of molar mass distribution rapidly increases as the macromonomers become longer. The SEC curves clearly show a long low-molar-mass tail; presumably due to the serious chain termination at the relatively higher reaction temperature. The CuBr-PMDETA system leads to a narrow molar mass distribution, slightly broadening as the chains are getting longer. There is a shoulder on the left of the SEC curve, marked by an arrow in Fig. 3.6, when the average molar mass reaches 3–4 $\times$ 10^4 g/mol, presumably due to the increase of solution viscosity and some side reactions induced by CuBr [14–16]. The ARGET ATRP was carried out in anisole using Me$_6$TREN as a ligand and Sn(EH)$_2$ as a reductant, resulting in the longest macromonomers with the narrowest molar mass distribution. Our results reveal that lowering the CuBr concentration can effectively reduce side reactions. Thus, linear polystyrene macromonomer chains [alkyne-(PSt-bromine)$_2$] with different degrees of polymerization (*DP*) used in our study are all prepared by the ARGET ATRP method.

Further, Alkyne-(PSt-azide)$_2$ were prepared by an efficient substitution reaction of bromine in alkyne-(PSt-bromine)$_2$ with NaN_3 in DMF for 36 h [11, 12]. Figure 3.7 shows a comparison of two ^{1}H NMR spectra of macromonomers alkyne-(PSt-bromine)$_2$ and alkyne-(PSt-azide)$_2$. Besides the broad aromatic and aliphatic regions of styrene monomer and some signals from the initiator, two signals (H_h), originating from each end of the chain, are visible in their ^{1}H NMR spectra. The signal of the proton located at the chain end changes from 3.80–4.10 ppm (H_h in Fig. 3.7b) to 4.30–4.50 ppm (H_h in Fig. 3.7a), indicating a successful substitution. We estimated the average azide chain-end functionality (f) of the chains prepared by ARGET ATRP to be ~99 % from the area ratio of the H_h and H_b peaks in Fig. 3.7a, i.e., f = Functionality (%) = 100(H_h/H_b), which indicates that the loss of terminal

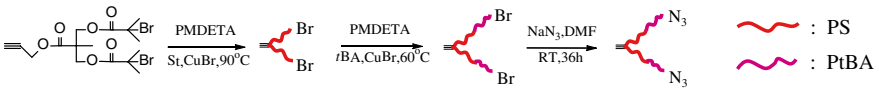

Fig. 3.8 Schematic synthesis of Seesaw-type macromonomer P*t*BA-PS-P*t*BA triblock copolymer

bromine group is negligible and the azidation reaction was nearly complete, resulting in a set of narrowly distributed and highly functional linear Seesaw-type polystyrene macromonomer homopolymers (azide~~~~alkyne~~~~azide) with different lengths.

Armed with these polystyrene macromonomers and using versatile "click" chemistry, we further prepared a series of "perfect" hyperbranched polystyrenes and studied their solution properties. This part of work will be discussed in the next chapter.

3.2.2 Preparation of Seesaw-Type Macromonomer Triblock Comopolymers

Similar to the synthetic process of macromonomer polystyrene homopolymer, we have also synthesized Seesaw-type macromonomer triblock copolymer [1]. This is because we have been interested in the phase behaviors of long linear multi-block copolymer chains in selective solvents for many years [18, 19]. Therefore, we intentionally prepared Seesaw-type macromonomer triblock copolymers to construct hyperbranched block copolymers and study their solution properties.

The preparation procedure of narrowly distributed Seesaw-type macromonomer triblock copolymers, poly(*tert*-butyl acrylate)-polystyrene-poly(*tert*-butyl acrylate) (P*t*BA-PS-P*t*BA), with one alkyne group in the center of the PS block and one azide group at the end of each P*t*BA block is similar to that of macromonomer polystyrene homopolymers. The schematic synthesis of P*t*BA-PS-P*t*BA triblock copolymer is shown in Fig. 3.8. The corresponding *DP* values were calculated from area ratio of corresponding peaks in ^{1}H NMR spectrum, as shown in Fig. 3.9, and the molecular parameters of our obtained triblock copolymers macromonomer P*t*BA-PS-P*t*BA with different St and *t*BA molar contents and molar masses are summarized in Table 3.2.

In a typical ATRP process, the molar concentrations of CuBr-PMDETA catalyst and initiator are usually similar. However, such an equivalency unexpectedly leads to an uncontrollable ATRP process of *t*BA monomer. Figure 3.10 shows how the CuBr-PMDETA catalyst molar concentration affects the molar mass and polydispersity index (M_w/M_n) of the resultant triblock copolymers P*t*BA-PS-P*t*BA. Namely, M_w/M_n increases with the CuBr-PMDETA catalyst concentration, indicating the side reactions. After decreasing the catalyst/initiator molar ratio to 1/5, we obtained narrowly distributed triblock copolymer P*t*BA-PS-P*t*BA, but the corresponding polymerization rate is low. Our results reveal that for the acrylate-derived monomers, lowering the CuBr-PMDETA concentration can effectively

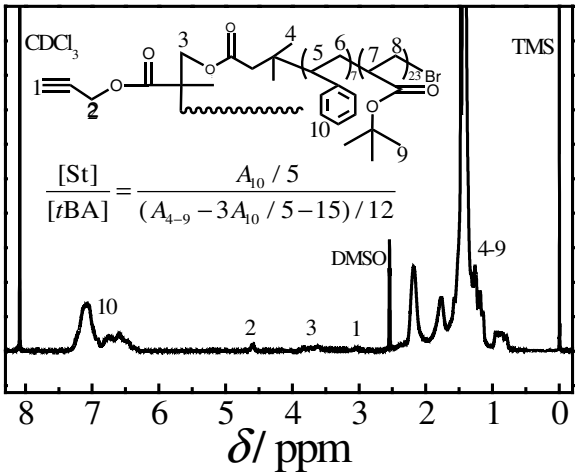

Fig. 3.9 Typical ^{1}H NMR spectrum of triblock copolymer P*t*BA$_{23}$-PS$_{14}$-P*t*BA$_{23}$

Table 3.2 Characterization of linear P*t*BA-PS-P*t*BA triblock copolymers (macromonomers) prepared by ATRP

Macromonomer[a]	M_n/(g/mol)[b]	M_w/M_n[b]
P*t*BA$_{23}$-PS$_{14}$-P*t*BA$_{23}$	7.7×10^3	1.11
P*t*BA$_{36}$-PS$_{55}$-P*t*BA$_{36}$	1.60×10^4	1.19

[a] Degrees of polymerization (*DP*), subscripts are calculated from ^{1}H NMR spectra
[b] Relative number-average molar mass (M_n) and polydispersity index (M_w/M_n) are measured by size excluded chromatography and calibrated by polystyrene standards

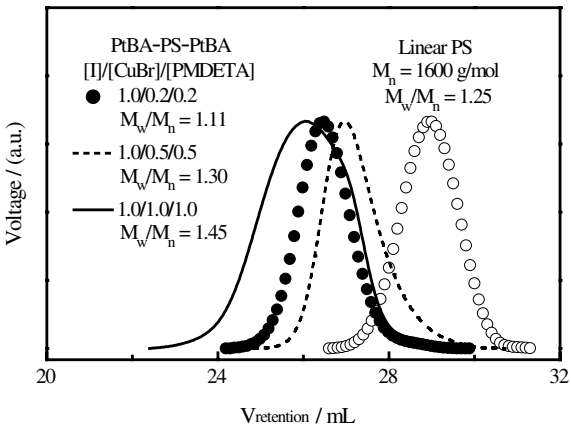

Fig. 3.10 SEC curves of triblock copolymer P*t*BA-PS-P*t*BA prepared with different CuBr-PMDETA catalyst concentrations

reduce the complexation between CuBr and alkyne groups when the initiator contains an alkyne group. Therefore, triblock macromonomers used in the current study are all prepared by ATRP method with a catalyst/initiator ratio of 1/5.

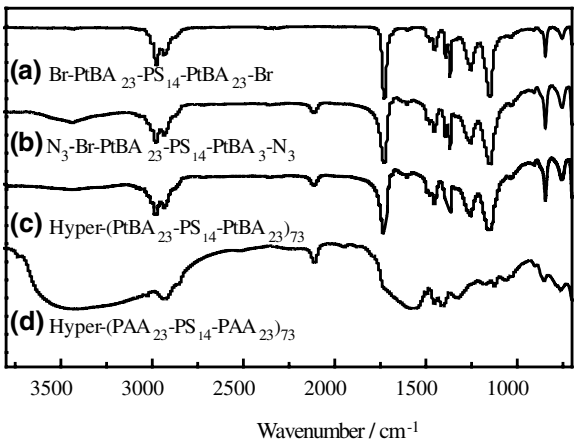

Fig. 3.11 IR spectra of P*t*BA$_{23}$-PS$_{14}$-P*t*BA$_{23}$, where **a** *before* and **b** *after* azidation; **c** *after* "clicking" reaction to form hyperbranched block copolymer hyper-(P*t*BA$_{23}$-PS$_{14}$- P*t*BA$_{23}$)$_{73}$; and **d** *after* hydrolysis of *tert*-butyl groups to form hyperbranched block copolymer hyper-(PAA$_{23}$-PS$_{14}$- PAA$_{23}$)$_{73}$

Further azidation of P*t*BA-PS-P*t*BA was carried by an efficient substitution reaction of bromine groups with NaN_3 in DMF for 36 h. The successful installation of two azide groups was reflected in the appearance of a N=N=N anti-symmetric stretch near ~2,090 cm^{-1} upon the conversion of Br-P*t*BA-PS-P*t*BA-Br to N_3-P*t*BA-PS-P*t*BA-N_3 (Fig. 3.11). Thus, we successfully obtained Seesaw-type macromonomer N_3-P*t*BA-PS-P*t*BA-N_3 with different block lengths.

3.2.3 Preparation of Seesaw-Type Macromonomer Diblock Comopolymers

It is worth noting that previously prepared two kinds of Seesaw-type macromonomers are limited to vinyl monomers which can only undergo living radical polymerization, but the degradable cyclic monomers which can undergo ring-opening polymerization (ROP) can not be incorporated into our prepared macromonomers and hyperbranched polymers. It should be noted that a combination of vinyl and cyclic monomers can extend our synthetic strategy to prepare hyperbranched polymers with two different types of monomers so that a hyperbranched copolymer chain can contain two kinds of controllable and uniform amphiphilic subchains that have various applications. Especially, those hyperbranched copolymers with one kind of biodegradable subchains are biomedically useful. However, it is rather a challenge to obtain such a kind of hyperbranched copolymer, if not impossible.

Therefore, we further developed an approach to solve such a challenging problem. Namely, we intentionally prepared a B~~~A----B Seesaw-type diblock macromonomer precursor, where ~~~ and ---- respectively represent polystyrene (PS) and poly(ε-caprolactone) (PCL) blocks. Using such a special diblock macromonomer, we have successfully prepared hetero-subchain hyperbranched copolymers with two kinds of controllable uniform long subchains.

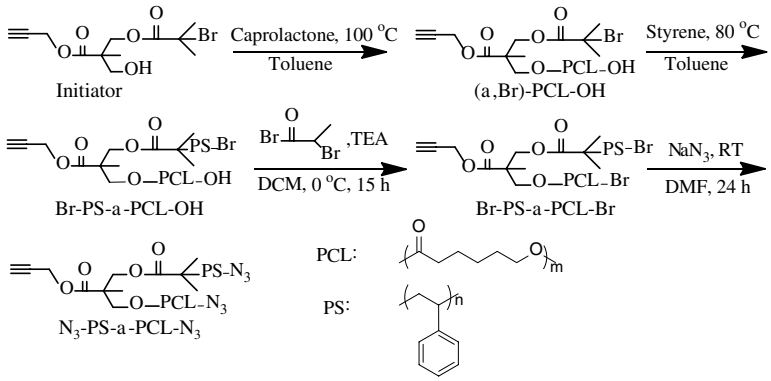

Fig. 3.12 Schematic of synthesis of Seesaw-type macromonomer diblock N_3-PS-*b*-PCL-N_3

To prepare B~~~A----B, we started with a tri-functional initiator (initiator II) with one alkyne (-≡-), one hydroxyl (–OH) and one bromine groups (–Br) to first initiate the polymerization of the ε-caprolactone and then the polymerization of styrene by successive ROP and ATRP processes, resulting in two diblock macromonomers (Br-PS-≡-PCL-OH) with an identical PCL block but two PS blocks with different lengths. Further bromination and azidation led to two N_3-PS-≡-PCL-N_3 precursors. The schematic synthesis is shown in Fig. 3.12.

The absolute *DP*s of the PCL and PS blocks were determined by ^{1}H NMR (Fig. 3.13a), where the characteristic peaks located at ~4.00 ppm ("d") and ~3.65 ppm ("d") are attributed to the protons of $–CH_2OOC–$ and $–CH_2–OH$ on the chain backbone and end of each PCL block, respectively. Therefore, *DP* of the PCL block is the area ratio (*A*) of the two peaks, i.e.,

$$DP_{\mathrm{PCL}} = (A_{\mathrm{d}} + A_{d'}) \big/ A_{\mathrm{d}'} \tag{3.1}$$

Similarly, we have *DP* of the PS block as the area ratio of the peak (a) and peaks (d and d′),

$$DP_{\mathrm{PS}} = (2DP_{\mathrm{PCL}}A_a)/(5(A_{\mathrm{d}} + A_{d'})) \tag{3.2}$$

Further conversion of precursor Br-PS_{39}-≡-PCL_{28}-OH into Br-PS_{39}-≡-PCL_{28}-Br in a 15-fold excess amount of bromination agent, 2-bromopropionyl bromide, with respect to the hydroxyl groups was reflected in the disappearance of the proton signals (~3.65 ppm, "d′" in Fig. 3.13a) of the $–CH_2–OH$ located at the end of the PCL block. The substitution extent was over 95 %. Note that both of the bromines located at the PS and PCL block ends are bonded to secondary carbon atoms, avoiding possible different reactivities between the two bromines. Figure 3.13b shows that

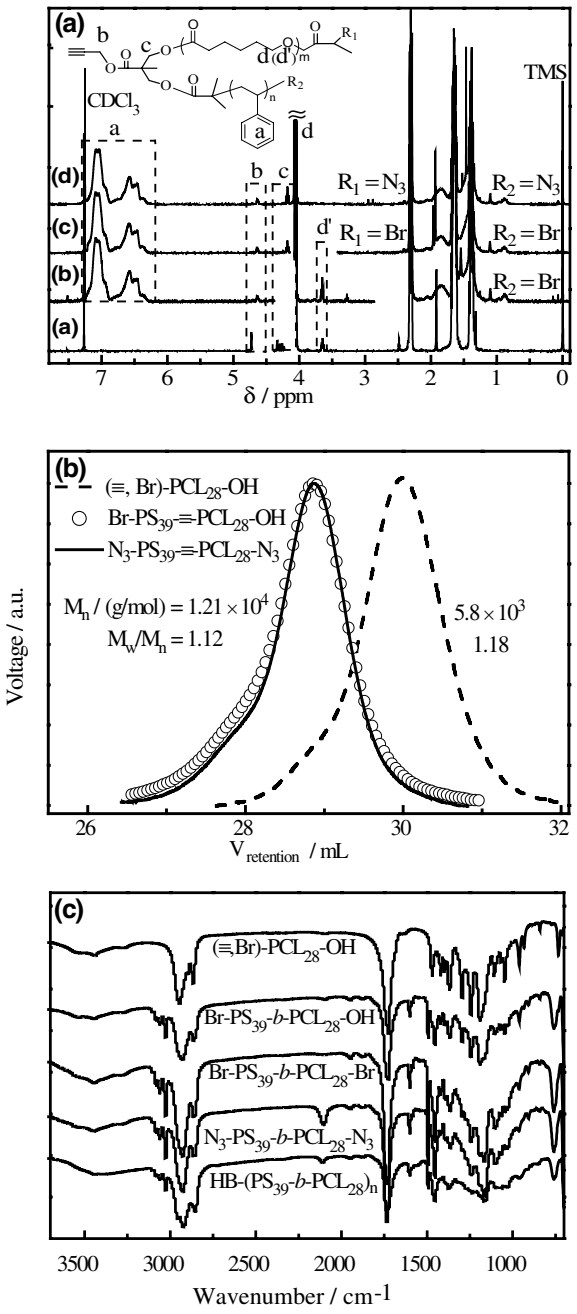

Fig. 3.13 Characterization of macromonomer precursors with different chain ends: **a** ^{1}H NMR spectra of (*a*) (≡,Br)-PCL$_{28}$-OH, (*b*) Br-PS$_{39}$-≡-PCL$_{28}$-OH, (*c*) Br-PS$_{39}$-≡-PCL$_{28}$-Br and (*d*) N$_3$-PS$_{39}$-≡-PCL$_{28}$-N$_3$; **b** GPC curves; and **c** FT-IR spectra

(≡,Br)-PCL$_{28}$-OH and Br-PS$_{39}$-≡-PCL$_{28}$-OH are narrowly distributed and there is no obvious bi-radical termination; namely, both ROP and ATRP processes are well-controlled.

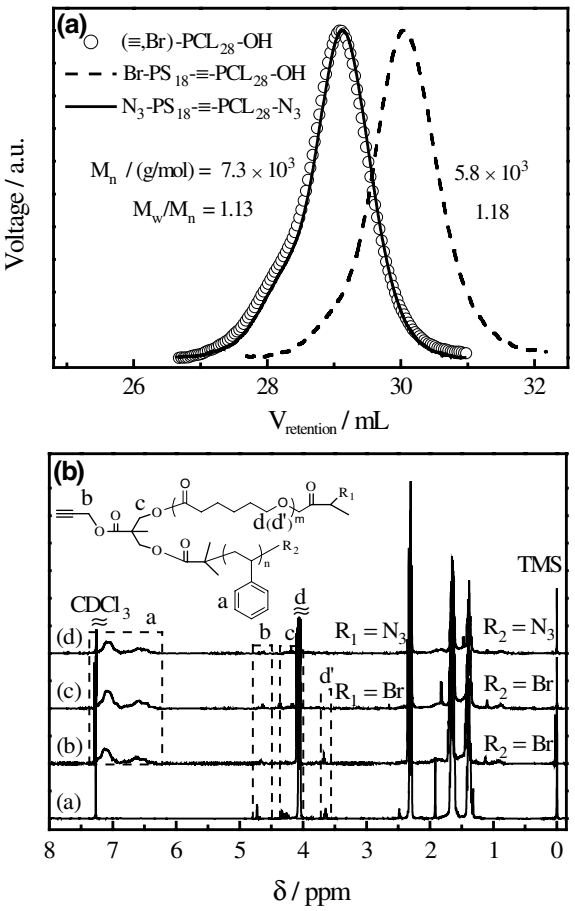

Fig. 3.14 Characterization of macromonomer precursors with different chain ends: **a** GPC curves and **b** ^{1}H NMR spectra of (*a*) (≡,Br)-PCL$_{28}$-OH, (*b*) Br-PS$_{18}$-≡-PCL$_{28}$-OH, (*c*) Br-PS$_{18}$-≡-PCL$_{28}$-Br and (*d*) N$_3$-PS$_{18}$-≡-PCL$_{28}$-N$_3$

Further substitution of each bromine end by an azide moiety resulted in our final precursor macromonomer N$_3$-PS$_{39}$-≡-PCL$_{28}$-N$_3$. The successful substitution of the bromines was reflected in the strong N=N=N asymmetrical stretching vibration (~2100 cm^{-1}) (Fig. 3.13c). On the other hand, Fig. 3.13b shows no obvious difference between the elution curves of Br-PS$_{39}$-≡-PCL$_{28}$-OH and N$_3$-PS$_{39}$-≡-PCL$_{28}$-N$_3$, indicating no side reaction.

In order to find how the PS subchain length and the overall chain molar mass affect the properties of such prepared hyperbranched copolymers HB-(PS-*b*-PCL)$_n$, we further made a diblock copolymer presursor (N$_3$-PS$_{18}$-≡-PCL$_{28}$-N$_3$) with an identical PCL block but a shorter PS block, and its characterization result is shown in Fig. 3.14. In the next chapter, we will further discuss the preparation of hyperbranched hetero-subchain copolymers by using such kind of macromonomers as precursors.

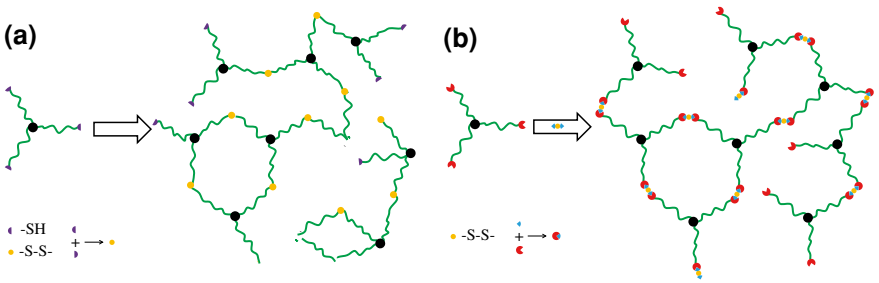

Fig. 3.15 Schematic illustration of the topological structures of disulfide-functionalized hyperbranched chains prepared by two different approaches: **a** Homo-polymerization of telechelic precursors with thiol end groups, and **b** Co-polymerization of disulfide-functionalized precursors

3.2.4 Preparation of Seesaw-Type Macromonomer Homopolymers with Clevable Disulfide Linkage

It is well-known that disulfide bonds can be cleaved into thiol groups in the presence of various reducing agents, such as thiols, phosphines and zinc dust; and the resulting thiol groups can reversibly reform disulfide bonds upon oxidation. Therefore, the thiol-disulfide exchange reaction has been widely used in various applications, such as drug delivery [20], gene transfection [21], and construction of self-healing materials [22, 23]. Meanwhile, a number of disulfide-functionalized polymer structures have been prepared, namely, linear (diblock [20, 24–26] and multiblock [27]), cyclic [27], comb-like [28, 29], hyperbranched [21, 30–34] and cross-linking [35–37] structures.

Generally, two main approaches have been used to introduce disulfide linkage into the polymer backbone: (1) homo-polymerization of telechelic precursors with two thiol moieties (Fig. 3.15a) [38, 39]; (2) co-polymerization of disulfide-functionalized precursors (Fig. 3.15b) [21, 30–32]. However, the distributions of the subchain length and disulfide bond location of hyperbranched polymers prepared by these two approaches will be only partly controllable [30, 40, 41]. To the best of our knowledge, it remains a challenge to prepare model hyperbranched polymers with uniform subchains and controlled locations of cleavable linkages simultaneously. Therefore, we further applied our Seesaw-type macromonomer strategy to synthesize model hyperbranched polystyrene chains with uniform subchains and controllably located cleavable disulfide linkages.

First, Seesaw-type macromonomer ≡-S-S-$(PS\text{-}N_3)_2$ with one disulfide linkage at the chain center was firstly prepared by ATRP and azidation substitution reaction [2]. The Schematic illustration of synthesis of disulfide-functionalized Seesaw-type initiator and linear polystyrene macromonomer ≡-S-S-$(PS\text{-}N_3)_2$ is shown in Fig. 3.16. Further interchain “clicking” coupling

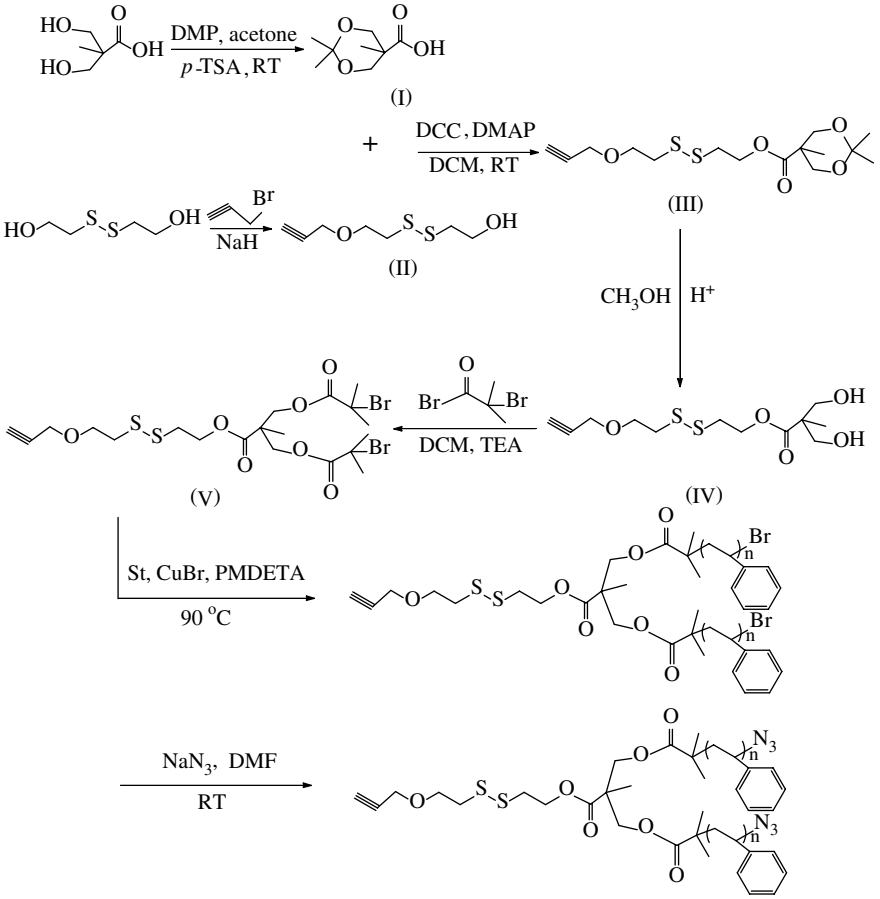

Fig. 3.16 Schematic illustration of the synthesis of disulfide-functionalized seesaw-type initiator and linear polystyrene macromonomer ≡-S-S-(PS-N_3)$_2$

of macromonomers ≡-S-S-(PS-N_3)$_2$ led to disulfide-functionalized hyperbranched polystyrene chains.

As shown in Fig. 3.16, disulfide-functional initiator was prepared through a five-step synthesis. Figures 3.17 and 3.18 confirm the high purity of the initiator and the intermediate compounds. As calculated in Fig. 3.17, the integral area ratio of peak (*a*), peak (*i*) and peak (*d*+*e*) is 1.00/3.10/4.09, in consistency with its theoretical ratio of 1.00/3.00/4.00. Using this functional initiator, Seesaw-type polystyrene macromonomer ≡-S-S-(PS-Br)$_2$ was successfully prepared by ATRP, and its typical ^{1}H NMR spectrum is shown in Fig. 3.19.

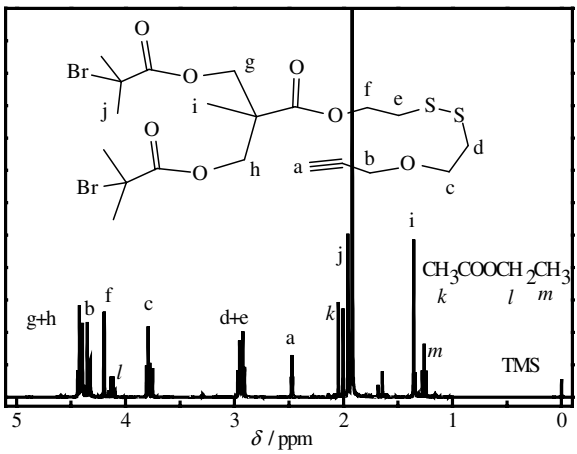

Fig. 3.17 ^{1}H NMR spectrum of disulfide-functionalized initiator

Figures 3.20, 3.21 and 3.22 show how the monomer conversion, number average molar mass (M_n), polydispersity index (M_w/M_n) and SEC curves of polystyrene evolved during the ATRP process. As shown in Fig. 3.20, the plot of semi-logarithmic of ln(1/(1-conversion)) versus t presents a linear relation, indicating the polymerization meets the required criteria of a living system. Figure 3.21 shows that the experimental M_n increases linearly with the conversion, and the M_w/M_n rapidly decreases with the conversion and reaches a minimum of ~1.14 at the end of polymerization, indicating the whole ATRP process is well-controlled, which is also reflected in the symmetric and narrowly distributed elution curves (Fig. 3.22).

In a typical ATRP process, the molar ratio of CuBr to halogen atom on initiator is normally 1.0/1.0, while the ratio in our study is controlled to be 1.0/0.5. In addition, the monomer conversion was intentionally controlled below 60 %, which is because both the CuBr concentration and monomer conversion are the key factors to attain polymer chains with high end-group functionalities. In principle, lowering both the CuBr concentration and monomer conversion can effectively reduce the chain termination and other side reactions [15, 42].

Further azidation substitution reaction of ≡-S-S-(PS-Br)$_2$ by sodium azide in DMF led to macromonomer ≡-S-S-(PS-N$_3$)$_2$. The successful installation of azide groups was reflected in the appearance of a N=N=N anti-symmetric stretching absorption band near ~2,090 cm^{-1} in FT-IR spectra (Fig. 3.23). Using such a novel Seesaw-type macromonomer ≡-S-S-(PS-N$_3$)$_2$, we prepared degradable hyperbranched polystyrene chains with uniform subchains and controlled locations of cleavable disulfide linkages. We will discuss this part of work in the next chapter.

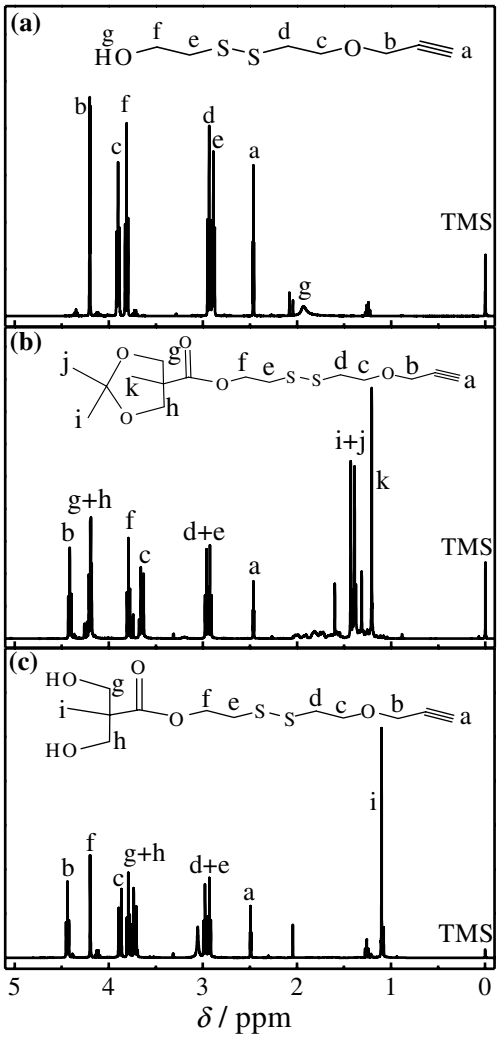

Fig. 3.18 ^{1}H NMR spectra of the intermediate compounds (II–IV) in $CDCl_3$

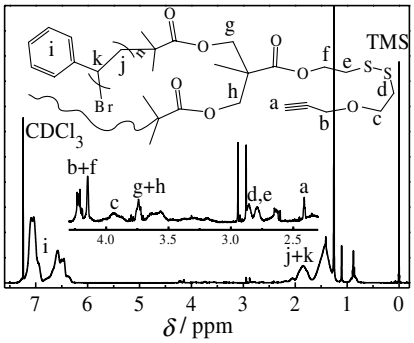

Fig. 3.19 ^{1}H NMR spectrum of disulfide-functionalized ≡-S-S-(PS-Br)$_2$

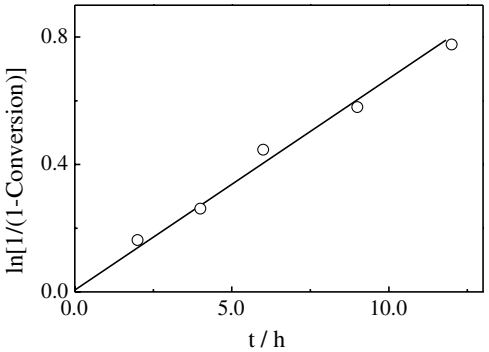

Fig. 3.20 *a* Kinetic plot of semi-logarithmic of ln(1/(1-Conversion)) versus reaction time (*t*) during the ATRP process. Reaction conditions: [styrene]/[initiator]/[CuBr]/[PMDETA] = 150/1/1/1; $T = 90$ °C; bulk

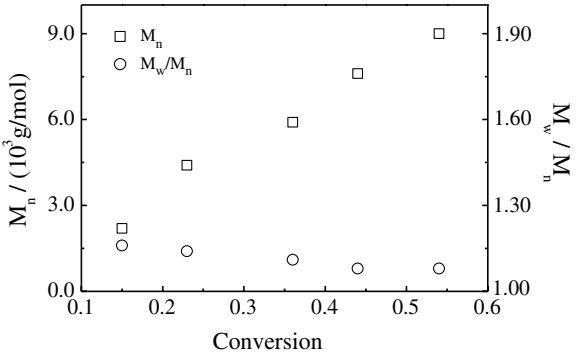

Fig. 3.21 Monomer conversion dependence of number average molar mass (M_n) and polydispersity index (M_w/M_n) of macromonomer ≡-S-S-(PS-Br)$_2$ during the ATRP process

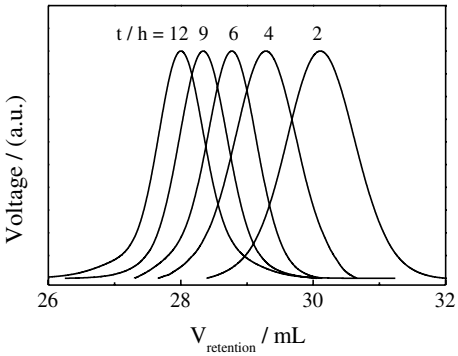

Fig. 3.22 Reaction time (t) dependent SEC curves of macromonomer ≡-S-S-(PS-Br)$_2$ during the ATRP process

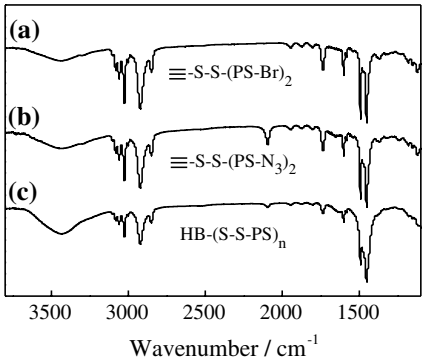

Fig. 3.23 IR spectra of a ≡-S-S-(PS-Br)$_2$, b ≡-S-S-(PS-N$_3$)$_2$, and c HB-(S-S-PS)$_n$

References

1. Li L, Zhou J, Wu C (2012) Macromolecules 45:9391
2. Li L, Wang X, Yang J, Ye X, Wu C (2014) Macromolecules (in press)
3. Li L, Wang X, He C, He W (2014) J Polym Sci Polym Chem 52:128
4. Li L, Lu Y, An L, Wu C (2013) J Chem Phys 138:114908
5. He C, He W-D, Li L-W, Jiang W-X, Tao J, Yang J, Chen L, Ge X-S, Chen S-Q (2012) J Polym Sci Polym Chem 50:3214
6. Li L, He C, He W, Wu C (2011) Macromolecules 44:8195
7. He C, Li L-W, He W-D, Jiang W-X, Wu C (2011) Macromolecules 44:6233
8. Trollsås M, Hedrick JL (1998) Macromolecules 31:4390
9. Trollsas M, Kelly MA, Claesson H, Siemens R, Hedrick JL (1999) Macromolecules 32:4917
10. Liu Q, Zhao P, Chen Y (2007) J Polym Sci Polym Chem 45:3330
11. Golas PL, Matyjaszewski K (2007) QSAR Comb Sci 26:1116
12. Qin A, Lam JWY, Tang BZ (2010) Macromolecules 43:8693
13. Lodge TP (2009) Macromolecules 42:3827
14. Lutz JF, Borner HG, Weichenhan K (2005) Macromol Rapid Comm 26:514

15. Lutz JF, Matyjaszewski K (2005) J Polym Sci Polym Chem 43:897
16. Jakubowski W, Kirci-Denizli B, Gil RR, Matyjaszewski K (2008) Macromol Chem Phys 209:32
17. Datta H, Bhowmick AK, Singha NK (2007) J Polym Sci Polym Chem 45:1661
18. Hong L, Zhu F, Li J, Ngai T, Xie Z, Wu C (2008) Macromolecules 41:2219
19. Zhang Q (2008) Macromolecules 41:2228
20. Wang W, Sun H, Meng F, Ma S, Liu H, Zhong Z (2012) Soft Matter 8:3949
21. Jiang X, Liu J, Xu L, Zhuo R (2011) Macromol Chem Phys 212:64
22. Canadell J, Goossens H, Klumperman B (2011) Macromolecules 44:2536
23. Yoon JA, Kamada J, Koynov K, Mohin J, Nicolaÿ R, Zhang Y, Balazs AC, Kowalewski T, Matyjaszewski K (2011) Macromolecules 45:142
24. Tsarevsky NV, Matyjaszewski K (2002) Macromolecules 35:9009
25. Wang Y-C, Wang F, Sun T-M, Wang J (1939) Bioconjug Chem 2011:22
26. Ko NR, Yao K, Tang C, Oh JK (2012) J Polym Sci Polym Chem 51:3071
27. Whittaker MR, Goh Y-K, Gemici H, Legge TM, Perrier S, Monteiro MJ (2006) Macromolecules 39:9028
28. Yuan L, Liu J, Wen J, Zhao H (2012) Langmuir 28:11232
29. Zhang M, Liu H, Shao W, Miao K, Zhao Y (2013) Macromolecules 46:1325
30. Tsarevsky NV, Huang J, Matyjaszewski K (2009) J Polym Sci Polym Chem 47:6839
31. Xu J, Tao L, Liu J, Bulmus V, Davis TP (2009) Macromolecules 42:6893
32. Yang W, Pan C-Y (2009) Macromol Rapid Commun 30:2096
33. Yan J-J, Hong C-Y, You Y-Z (2011) Macromolecules 44:1247
34. Jiang X, Zhang M, Li S, Shao W, Zhao Y (2012) Chem Commun 48:9906
35. Kamada J, Koynov K, Corten C, Juhari A, Yoon JA, Urban MW, Balazs AC, Matyjaszewski K (2010) Macromolecules 43:4133
36. Steinhauer W, Keul H, Moller M (2011) Polym Chem
37. Zhang Q, Aleksanian S, Noh SM, Oh JK (2013) Polym Chem 4:351
38. Choi J, Kwak S-Y (2003) Macromolecules 36:8630
39. Liu M, Vladimirov N, Fréchet JMJ (1999) Macromolecules 32:6881
40. Rikkou-Kalourkoti M, Matyjaszewski K, Patrickios CS (2012) Macromolecules 45:1313
41. Tsarevsky NV, Matyjaszewski K (2005) Macromolecules 38:3087
42. Tsarevsky NV, Braunecker WA, Matyjaszewski K (2007) J Organomet Chem 692:3212

Chapter 4
Preparation of "Perfect" Hyperbranched Homopolymers and Copolymers by "Click" Chemistry

In the previous chapter, we discussed the design strategy and synthetic detail of various Seesaw-type macromonomers, including homopolymers, triblock copolymers and diblock copolymers. Armed with these novel Seesaw-type macromonomers, a number of "perfect" hyperbranched homopolymers and copolymers could be prepared through the versatile interchain "click" coupling. More specifically, we prepared hyperbranched homopolymers [1–4], hyperbranched block copolymers [5], hyperbranched graft copolymers [6] and hyperbranched hetero-subchain copolymers. Figure 4.1 shows the topological structure schematic of these hyperbranched (co)polymers. In this chapter, we'll turn to discuss the synthetic detail of these "perfect" hyperbranched (co)polymers.

4.1 Preparation of Hyperbranched Polystyrene Homopolymers

First, using linear azide~~PSt~~alkyne~~PSt~~azide macromonomers with different lengths, we prepared and characterize a series of large hyperbranched polystyrene homopolymers with uniform subchains by "click" chemistry (Fig. 4.2). The self-polycondensation kinetics was monitored by a combination of size exclusion chromatography (SEC) with a refractive index (RI) detector and a multi-angle laser light scattering (MALLS) detector, and a stand-alone laser light scattering (LLS).

The fractionation of each resultant broadly distributed hyperbranched polystyrene sample by precipitation led to a set of "perfect" narrowly distributed hyperbranched polystyrene chains with uniform subchains but different overall molar masses. We have, *for the first time*, experimentally elucidated their formation kinetics and established scaling laws between their size and overall mass. Armed with such prepared hyperbranched chains, we will be able to further study correlations between their microscopic structures and macroscopic properties. In this section, we will focus on the formation kinetics section, and the fractal properties of these "perfect" hyperbranched polystyrenes will be discussed in the next chapter.

L. Li, *Studies on "Perfect" Hyperbranched Chains Free in Solution and Confined in a Cylindrical Pore*, Springer Theses, DOI: 10.1007/978-3-319-06097-2_4,

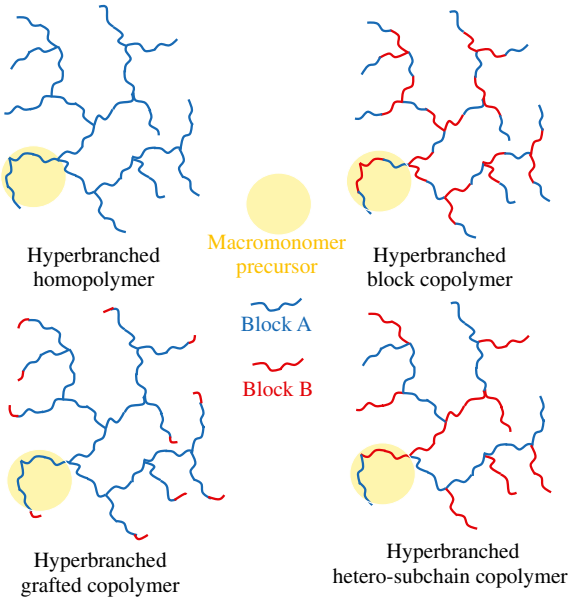

Fig. 4.1 Schematic of the topological structures of the hyperbranched polymers prepared from various kinds of Seesaw-type macromonomers

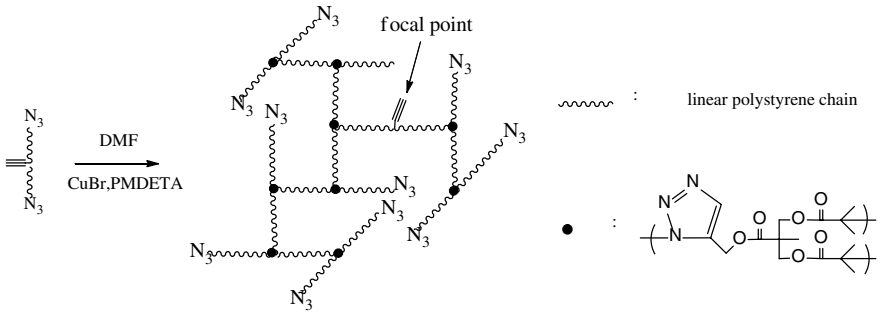

Fig. 4.2 Schematic of synthesis of hyperbranched polystyrene homopolymers by "click" chemistry

To obtain large hyperbranched polystyrene chains, the alkyne-azide "click" cycloaddition was used in our study because of its high efficiency and low susceptibility to side reactions without oxygen [7–9]. DMF was used as solvent in the self-poly-condensation of alkyne-(PSt-azide)$_2$ after the removal of oxygen at 35 °C with a catalyst of CuBr-PMDETA. We first investigated how the initial molar mass and concentration of alkyne-(PSt-azide)$_2$ affect the kinetics of the self-polycondensation of linear Seesaw-type polystyrene macromonomers.

Note that it is better to describe the self-polycondensation in terms of the average degree of polycondensation (*DP*) [10–13], instead of the number and weight

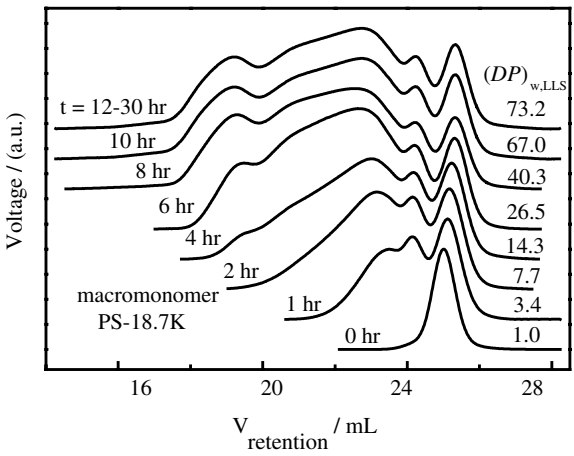

Fig. 4.3 Reaction time dependence of SEC curves of hyperbranched polystyrenes obtained from polycondensation of PS-18.7K, where $C_o = 0.15$ g/mL

average molar mass (M_n and M_w), because initial macromonomers have different lengths, where DP is defined as the number of macromonomers chemically coupled together inside each hyperbranched polystyrene chain; namely $(DP)_n = M_{n,\text{hyperbranched}}/M_{n,\text{macromonomer}}$ and $(DP)_w = M_{w,\text{hyperbranched}}/M_{w,\text{macromonomer}}$. We prefer to use $(DP)_w$ to describe the polycondensation kinetics because it is the weight average molar mass that was measured in SEC-RI or SEC-MALLS.

For the convenience of discussion, we rename polystyrene macromonomers with molar masses of 7.6×10^3, 18.7×10^3 and 45.0×10^3 g/mol as PS-7.6K, PS-18.7K and PS-45K to reflect their molar masses, respectively. Figure 4.3 shows SEC curves of hyperbranched polymers obtained from the self-polycondensation of PS-18.7K in DMF at 35 °C after different reaction times. As the reaction proceeds, the macromonomer peak becomes smaller and the large hyperbranched polymer peaks are emerging after a few hours, as shown by the shoulder with a retention volume less than 20 mL. However, there still exist about 10 % initial macromonomers estimated from its peak area and the whole area of GPC trace. However, it is known that SEC-RI-PSt-calibration is not able to effectively distinguish polymer chains with a similar hydrodynamic size but different topologic structures. Therefore, a large deviation from the true molar mass could occur in the high molar mass range, leading to a notable change in $(DP)_w$. To avoid such a problem, we further used a combination of SEC and MALLS as well as our stand-alone static LLS to characterize the absolute weight-average molar mass of each hyperbranched sample to obtain the true $(DP)_w$ and M_w/M_n. The results are summarized in Figs. 4.4, 4.5, 4.6 and 4.7.

Figure 4.4 shows that large hyperbranched PSt chains are formed and their final average degree of self-polycondensation $(DP)_w$ increases from 40 to 81 as the initial molar mass of macromonomers decreases from 4.50×10^4 to 7.60×10^3 g/mol, presumably due to the two following reasons: (1) The functional end groups on longer initial chains are much less reactive because they are wrapped inside individual coiled chains; and (2) the total concentration of the functional end groups is less for a given weight concentration (g/mL), also reflecting in its relatively lower reaction rate.

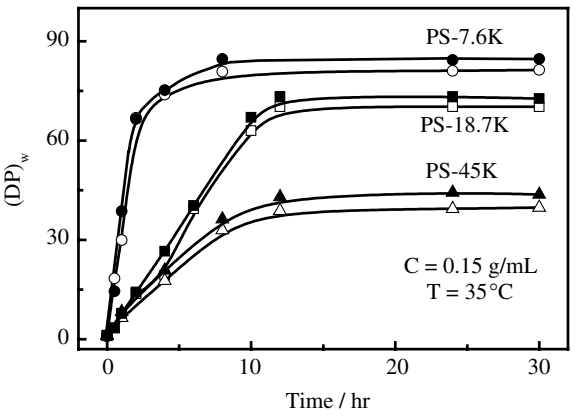

Fig. 4.4 Macromonomer length dependence of $(DP)_w$ of hyperbranched polystyrenes, where *filled* and *hollow symbols* represent results from stand-alone static LLS and SEC-MALLS, respectively

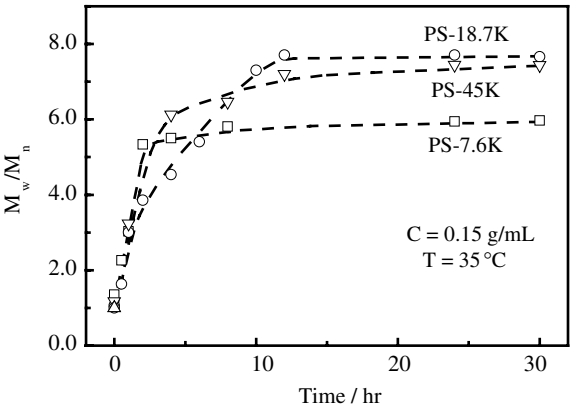

Fig. 4.5 Reaction time dependence of polydispersity index (M_w/M_n) of hyperbranched polystyrenes prepared with different initial macromonomers

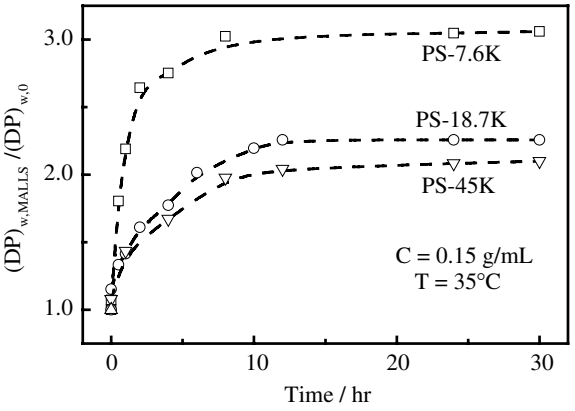

Fig. 4.6 Reaction time dependence of $(DP)_{w,SEC\text{-}MALLS}/(DP)_{w,SEC\text{-}RI}$ of hyperbranched polystyrenes, where $(DP)_{w,SEC\text{-}MALLS}$ and $(DP)_{w,SEC\text{-}RI}$ were respectively measured using a combination of SEC with a RI and a MALLS detector

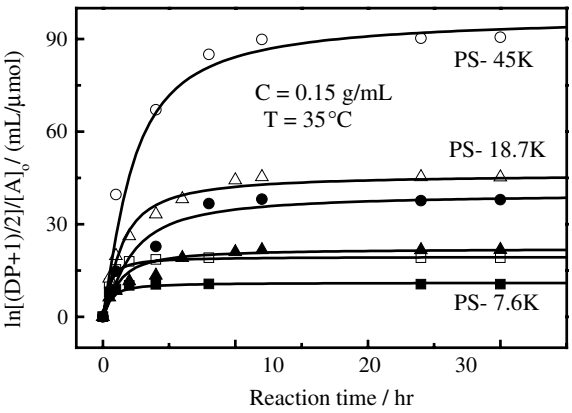

Fig. 4.7 Reaction time dependence of $\ln[(DP + 1)/2]/[A]_o$ for macromonomers with different lengths, where *filled symbols*, *hollow symbols* and *lines*, respectively, represent experimental $(DP)_n$ $(DP)_w$ and fitting curves using Eq. 4.5 with $k_{AB,0} = 1.2 \times 10^5$ and 2.8×10^5 mL/(mol h) for $(DP)_n$ and $(DP)_w$, respectively

Figure 4.5 shows that the polydispersity index (M_w/M_n) (determined by MALLS detector) increases with the reaction time. It is known that in the self-polycondensation process, hyperbranched chains with more azide groups are ready to react with macromonomers but more difficult to react with each other because there is only one hiding A group inside each hyperbranched chain. However, the coupling between two hyperbranched chains in the later stage of reaction makes M_w to increase much fast than M_n. This is why M_w/M_n quickly raises to 5.8–7.7.

Figure 4.6 shows the ratio of $(DP)_{w,SEC\text{-}MALLS}/(DP)_{w,SEC\text{-}RI}$ of hyperbranched polystyrenes rapidly increases to 3.1 (PS-7.6K), 2.3 (PS-18.7K) and 2.1 (PS-45K), respectively, with the reaction time. The deviation of $(DP)_{w,SEC\text{-}MALLS}$ away from $(DP)_{w,SEC\text{-}RI}$ clearly shows that SEC with the conventional universal polystyrene calibration leads to a much under-estimated molar mass for large hyperbranched chains. Therefore, it should be avoided in the study of branched chains because they have a much smaller hydrodynamic volume than their linear counterparts with a similar molar mass. In other words $(DP)_{w,SEC\text{-}MALLS}/(DP)_{w,SEC\text{-}RI}$ reflects the hydrodynamic volume difference between hyperbranched and linear chains; namely $(DP)_{w,SEC\text{-}MALLS}/(DP)_{w,SEC\text{-}RI}$ increases with the compactness of hyperbranched chains.

Next, let us analyze the reaction kinetics of the interchain coupling of different macromonomers. On the basis of Fig. 4.4 and considering the nature of the self-polycondensation, we can assume that it follows the 2nd-order kinetics, i.e.,

$$-\mathrm{d}[A]/\mathrm{d}t = k_{AB}[A][B] \tag{4.1}$$

where [A] and [B] represent the molar concentrations of alkyne and azide groups, respectively; $[B]_o = 2[A]_o$ at $t = 0$; $[B] = [B]_o - ([A]_o - [A]) = [A]_o + [A]$ at $t = t$ so that Eq. 4.1 is rewritten as

$$-\mathrm{d}[A]/\mathrm{d}t = k_{AB}([A]_o + [A])[A] \tag{4.2}$$

where [A] can be replaced by DP because $DP = [A]_o/[A]$ by its definition. Finally, we have

$$\ln \frac{DP+1}{2} = [A]_0 \int_0^t k_{AB}\, dt \tag{4.3}$$

It shows that at $t = 0$, $DP = 1$; and $t \gg 1$, DP approaches an infinite if k_{AB} is a constant, i.e., resulting in one infinitely large hyperbranched polymer chain, which is chemically reasonable. However, our results reveal that the reaction slows down and DP approaches a constant when $t \gg 1$, presumably due to a decrease of the reactivity of the alkyne group inside each hyperbranched chain. At the initial stage, most of the alkyne groups are on linear macromonomers so that they can easily react with each other and with the azide groups on the periphery of a hyperbranched chain. As the reaction proceeds, the number of macromonomers decreases. When most of initial macromonomers are consumed, further polycondensation mostly involves the intrachain cyclization or the self-looping. It would be rather difficult for one alkyne group entrapped inside one hyperbranched chain to react with the azide groups on another chain. Note that the self-looping has no contribution to our experimentally measured values of DP. Considering such a physical nature, we assume that

$$k_{AB} = k_{AB,0} \frac{1}{1+(\beta t)^2} \tag{4.4}$$

where $k_{AB,0}$ is the initial rate constant at $t = 0$ and β is a constant, so that Eq. 4.4 is rewritten as

$$\ln \frac{DP+1}{2} = \frac{[A]_0 k_{AB,0}}{\beta} \arctan(\beta t) \tag{4.5}$$

It describes our experimental results well; namely, $DP = 1$ at $t = 0$; and $DP = k_{AB,0}\pi/(2\beta)$ at $t \gg 1$. In principle, we can obtain $[A]_o k_{AB,0}$ from the initial slope; $k_{AB,0}\pi/(2\beta)$ from the plateau value at $t \gg 1$; and β from a combination of $[A]_o k_{AB,0}$ and $k_{AB,0}\pi/(2\beta)$ since we know $[A]_0$.

However, we are not able to practically determine the accurate initial slope ($[A]_o k_{AB,0}$) because of a limited number of data points. Physically, it is reasonable to assume that $k_{AB,0}$ should be much less dependent on the initial concentration and length of macromonomers because it only reflects the initial reaction rate between A and B. Therefore, we are able to first use the iteration to estimate the average value of $k_{AB,0}$ for three different macromonomers used and then fix it in the fitting of our experimental data with Eq. 4.5, as shown in Fig. 4.7. In this way, β is the only adjustable parameter in the fitting. It is clear that Eq. 4.5 represents our experimental data well for both $(DP)_w$ and $(DP)_n$.

Table 4.1 summarizes the fitting results of β for different macromonomers when $(DP)_n$ and $(DP)_w$ are respectively used. β decreases as the macromonomer becomes longer. Note that physically, $1/\beta$ is the time at which k_{AB} decreases to 50 % of its initial value. The decrease of β means that it takes a longer time for the

Table 4.1 Calculated values of β for macromonomers with different initial lengths

Macromonomer	$[A]_o$	β/h^{-1} from $(DP)_n$	β/h^{-1} from $(DP)_w$
	μmol/mL	$k_{AB,0} = 1.2 \times 10^5$ mL/(mol h)	$k_{AB,0} = 2.8 \times 10^5$ mL/(mol h)
PS-7.6K	19.7	1.71	2.25
PS-18.7K	8.00	0.85	0.95
PS-45K	3.33	0.47	0.45

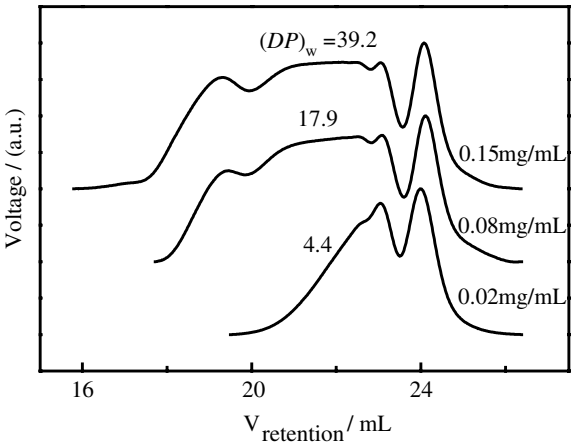

Fig. 4.8 Initial macromonomer concentration dependence of SEC curves of the resultant hyperbranched polystyrene samples after 48-h self-poly-condensation of PS-45K at 35 °C

reaction between A and B on longer macromonomer chains to slow down, which is physically reasonable because most of the reaction occurs between macromonomers and hyperbranched chains except at the very initial stage wherein linear azide~~~~alkyne~~~~azide macromonomers react with each other.

Figure 4.8 shows that the macromonomer peak slightly shift to the right, toward a larger retention volume, and its relative height decreases during the reaction, clearly indicating the occurence of self-cyclization of individual macromonomer chains. Further, Fig. 4.9 shows how the average degree of self-polycondensation (DP) obtained using a combination of SEC and LLS varies with the reaction time (t) when different initial macromonomer (PS-45K) concentrations are used. The lines in Fig. 4.9 are calculated using Eq. 4.5. It shows that for a given ratio of [macromonomer]:[CuBr]:[PMDETA] = 1:2:2, both the initial reaction rate and final degree of the self-polycondensation increase with the initial macromonomer concentration, agreeing well with the prediction of Eq. 4.5. It is worth-noting that Eq. 4.5 also shows that both the initial rate and final degree of the self-polycondensation are related to β. On the other hand, Fig. 4.7 and Table 4.1 show that β is related to the molar mass (length) of macromonomer used. As mentioned before, $1/\beta$ reflects the time at which k_{AB} decreases to 50 % of its initial value; namely, $k_{AB} = k_{AB,0}/2$ at $t = 1/\beta$, where $k_{AB,0}$ is a constant. Let us assume that the reaction rate is mainly controlled by diffusion, related to the interchain distance (L) and the translational diffusion coefficient (D). As expected, L increases as the

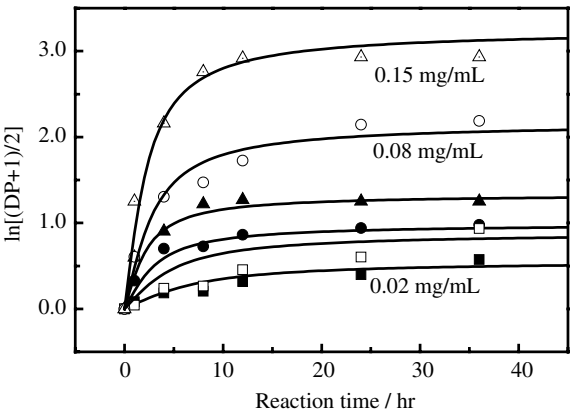

Fig. 4.9 Reaction time dependence of $\ln[(DP + 1)/2]$ with different initial PS-45K concentrations, where *filled* and *hollow symbols*, and *lines* respectively represent experimental $(DP)_n$ $(DP)_w$ and fitting curves using Eq. 4.5, where the values of $k_{AB,0}$ are previously determined

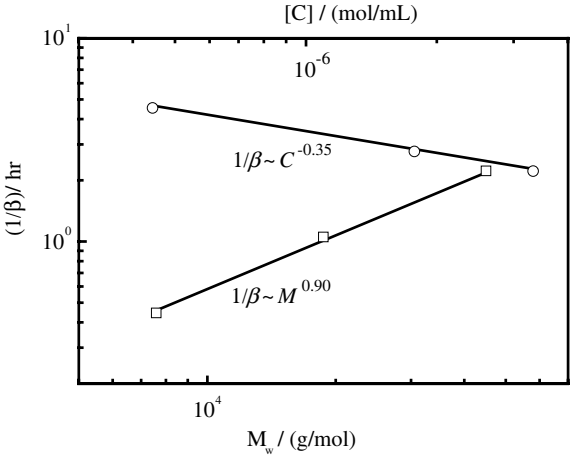

Fig. 4.10 Macromonomer's molar concentration ([C]) and weight average molar mass (M_w) dependence of $1/\beta$ obtained from reaction time dependent $(DP)_w$ in Figs. 4.7 and 4.9

initial macromonomer concentration (C_0) decreases, i.e., $L \sim C_0^{-1/3}$. Therefore, it should take a longer time for one macromonomer to react with another when C_0 decreases. On the other hand, it has been well known that D is scaled to the molar mass of a polymer chain as $D \sim M^{-\alpha}$ with $\alpha = 0.5$–0.6, depending on the solvent quality. Therefore, it is rather difficult for an azide group on one hyperbranched chain to react with the alkyne group hidden inside another hyperbranched chain. The reaction should mainly occur between macromonomers (in the very initial stage) and between one macromonomers and one hyperbranched chain.

Figure 4.10 shows two scalings: $1/\beta \sim [C]^{-0.35}$ and $\sim M_w^{0.90}$, where we have converted the weight concentration (C) in Fig. 4.7 to the molar concentration ([C]) by $[C] = C/M_w$. It is also worth-noting that in Fig. 4.4 we varied the molar mass of macromonomer but fixed its initial weight concentration (C). Therefore, we have to convert C to [C] and introduce an additional $M_w^{-0.35}$ into the scaling; namely, the exponent (0.90) on M_w should be reduced to 0.55. A combination of both the

$[C]$ and M_w dependence of $1/\beta$ finally leads to $1/\beta \sim [C]^{-0.35} M_w^{0.55}$, indicating that $1/\beta$ is related to both the interchain distance and diffusion.

This part of work clearly demonstrates that, in the preparation process of "perfect" polystyrene homopolymer chains, the "click" reaction rate of the self-polycondensation of alkyne-(PSt-azide)$_2$ increases with the initial concentration of macromonomers but is less influenced by the macromonomer's length. The kinetics is the second order but with a time-dependent rate constant: $k_{AB} = k_{AB,0}/[1 + (\beta t)^2]$, where $k_{AB,0}$ is the rate constant at $t = 0$ and $1/\beta$ is the time at which k_{AB} becomes half of $k_{AB,0}$. The whole interchain "click" process is governed by the interchain distance and diffusion, simultaneously.

4.2 Preparation of Hyperbranched Block Copolymers

Using Seesaw-type of triblock copolymers, poly(*tert*-butyl acrylate)-polystyrene-poly(*tert*-butyl acrylate) (P*t*BA-PS-P*t*BA), with one alkyne group in the center of the PS block and one azide group at the end of each P*t*BA block as precursors, we further prepared a series of narrowly distributed amphiphilic hyperbranched block copolymers hyper-(PAA$_{23}$-PS$_{14}$-PAA$_{23}$)$_n$ for the study of solution properties of amphiphilic hyperbranched copolymer chains in dilute and semedilute solutions by a combination of "click" chemistry, precipitation fractionation and hydrolyzation of *t*BA into AA, where the subscripts denote the degrees of polymerization of each block. Similarly, we also prepared narrowly distributed hyper-(P*t*BA$_{36}$-PS$_{55}$-P*t*BA$_{36}$)$_n$ with a much higher styrene weight fraction for the study of the intrachain folding [5] (Fig. 4.11).

Figure 4.12 shows the $(DP)_w$ of hyper-(P*t*BA$_{23}$-PS$_{14}$-P*t*BA$_{23}$)$_n$ increases with the concentration of Seesaw-type P*t*BA$_{23}$-PS$_{14}$-P*t*BA$_{23}$ triblock precursor, which is similar to our previous studies of polystyrene homopolymers [3, 4], presumably because of a higher concentration of reactive end group and a shorter average interchain distance. Figure 4.12 also shows that with an optimal precursor concentration (~0.35 g/mL), we obtained a hyperbranched block copolymer with $(DP)_w \sim 13$ and $M_w/M_n \sim 5$, sufficiently good for further precipitation fractionation.

Figure 4.13 shows four relatively narrowly distributed hyperbranched block copolymers ($M_w/M_n < 1.40$) resulted from the precipitation fractionation. The ^{1}H NMR and UV spectra (not shown) revealed that their styrene contents are nearly identical. After coupling linear triblock copolymer chains together, the intensity related to the azide stretching still partially remains (Fig. 3.11c) because only no more than half of the azide end groups are consumed in the "clicking" reaction. The de-protection of *tert*-butyl groups is reflected in the broad carboxylic-OH stretching peak (~3,700–2,600 cm^{-1}) and the shifting of the carbonyl stretching peak (~1,730 cm^{-1}) to a lower wave number (Fig. 3.11d), indicating that the hydrolysis of *tert*-butyl groups is nearly complete. Note that the previous experimental studies [14, 15] have

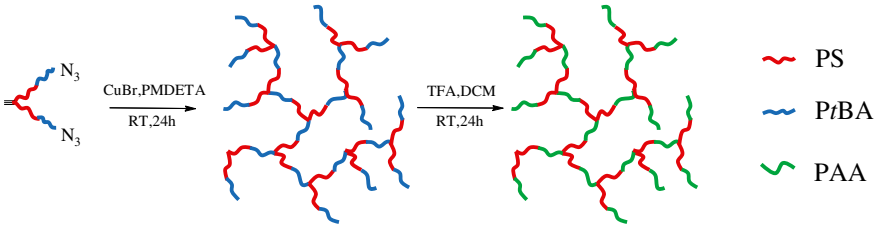

Fig. 4.11 Schematic of synthesis of larger hyperbranched amphiphilic copolymers with uniform subchains, hyper-(P*t*BA-PS-P*t*BA)$_n$ and hyper-(PAA-PS-PAA)$_n$

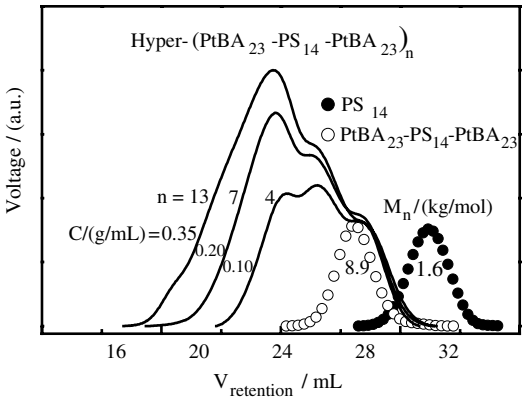

Fig. 4.12 Initial macromonomer concentration dependence of SEC curves of resultant hyperbranched block copolymers, hyper-(P*t*BA$_{23}$-PS$_{14}$-P*t*BA$_{23}$)$_n$, after 24 h polycondensation of triblock P*t*BA$_{23}$-PS$_{14}$-P*t*BA$_{23}$ in DMF at 35 °C

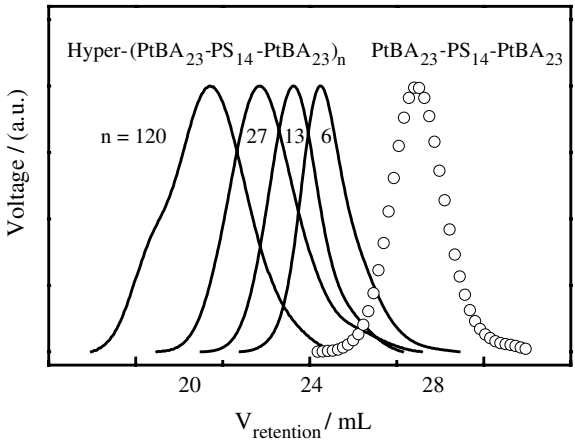

Fig. 4.13 SEC curves of four fractions of hyperbranched block copolymer hyper-(P*t*BA$_{23}$-PS$_{14}$-P*t*BA$_{23}$)$_n$ with different overall molar masses, which were obtained by precipitation fractionation

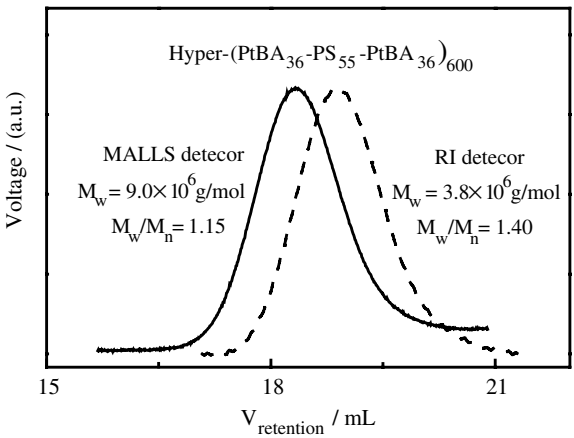

Fig. 4.14 SEC curves of hyper-(P*t*BA$_{36}$-PS$_{55}$-P*t*BA$_{36}$)$_{600}$ with two different detectors: RI (*dashed line*) and MALLS (*solid line*)

revealed that the ester bonds in the chain backbone undergo no cleavage during the TFA de-protection step, so that further characterization of the resultant copolymers after the de-protection is not necessary. These fractions of hyper-(PAA$_{23}$-PS$_{14}$-PAA$_{23}$)$_n$ were used to study the interchain association and rheological behaviors of amphiphilic hyperbranched block copolymers in water.

For the intrachain folding study, ultra-large hyperbranched copolymer hyper-(P*t*BA$_{36}$-PS$_{55}$-P*t*BA$_{36}$)$_{600}$ with a narrow molar mass distribution was prepared by a preparative SEC instead of the precipitation fractionation because we only need a very small amount of sample (10^2 μg), and Fig. 4.14 shows its SEC curve. As shown, the SEC measurement shows a narrow distribution with a M_w/M_n of ~1.15. Note that M_w from the RI detector is about three times smaller than that from the MALLS detector. This is because the scattered light intensity is proportional to the square of the mass of a scattering object. In addition, the branching effect will also result in a strong deviation of the real molar mass (MALLS detector) from the apparent one (RI detector). The detailed discussion about the solution properties of these amphiphilic hyperbranched copolymer chains will be given in the next chapter.

4.3 Preparation of Hyperbranched Graft Copolymers

To study the solution property of novel amphiphilic hyperbranched graft copolymer chains, we further prepared amphiphilic hyperbranched poly(acrylic acid) grafted with short polystyrene copolymer (HB-PAA-*g*-PS) with a large hydrophilic hyperbranched PAA core and short hydrophobic PS grafted chains. The copolymer chains with different branching degrees of PAA core were carefully prepared and well confirmed by SEC, ^{1}H NMR, and FT-IR. As well, the

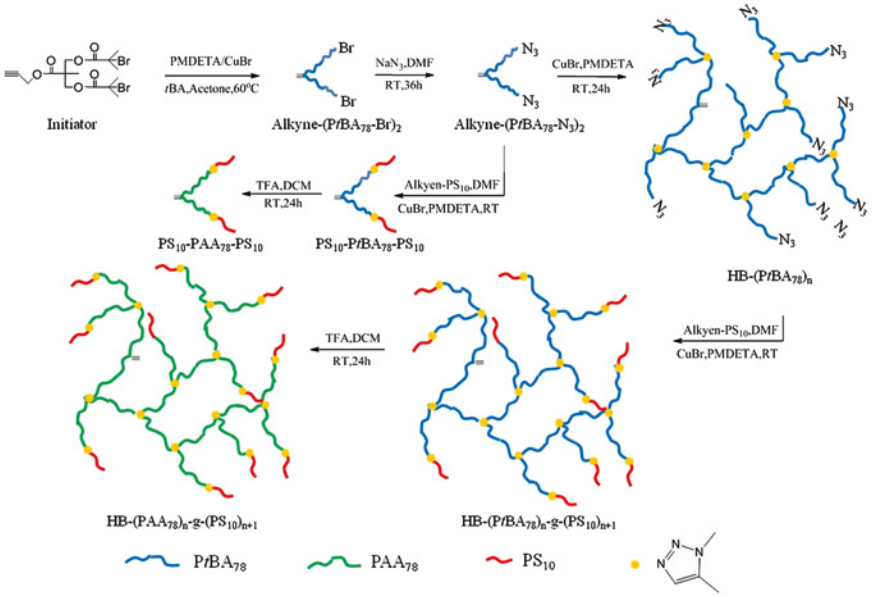

Fig. 4.15 Schematic of synthesis of amphiphilic hyperbranched poly(acrylic acid) grafted with short polystyrene copolymer chains (HB-PAA-*g*-PS) and their linear triblock PS-PAA-PS analogues

association, emulsifying and solubilization behavior of HB-PAA-*g*-PS chains in aqueous solution were investigated comparatively with their triblock PS-PAA-PS analogues by LLS, TEM, UV-vis.

Figure 4.15 schematically shows how linear triblock PS-P*t*BA-PS, hyperbranched graft copolymer HB-P*t*BA-*g*-PS, and its hydrolyzed target product are prepared. In our study, hyperbranched P*t*BA core was purposely prepared via our previously developed seesaw-type macromonomer strategy, i.e., azide-P*t*BA-alkyne-P*t*BA-azide macromonomer with one alkyne group in the center and one azide group at each chain end, which can ensure a uniform subchain length between two neighboring branching points. In this way, each resultant HB-$(PtBA_{78})_n$ core with no more than one alkyne group and many unreacted azide groups on the periphery can be treated as an ideal hyperbranched structure to study the structure-property correlation. Moreover, the remaining azide groups could be used to further couple with short linear alkyne-PS chains to result in HB-P*t*BA-*g*-PS copolymers. The characterization results of molecular parameters of prepared (co)polymers are summarized in Table 4.2.

First, well-defined Seesaw-type macromonomer alkyne-$(PtBA_{39}\text{-}N_3)_2$ was prepared via ATRP and azidation reaction. SEC curve (Fig. 4.16) demonstrates the prepared macromonomer alkyne-$(PtBA_{39}\text{-}N_3)_2$ is narrowly distributed with a polydispersity index (M_w/M_n) of ~1.09. The absolute *DP* value was calculated to be ~78 according to the ^{1}H NMR spectrum (Fig. 4.17).

Table 4.2 SEC characterization result of (co)polymer chains

Sample	M_n/(g/mol)[a]	M_w/(g/mol)[a]	M_w/M_n[a]
Alkyne-PS_{10}	9.00×10^2	1.10×10^3	1.22
Alkyne-(P*t*BA_{39}-N_3)$_2$	9.30×10^3	1.00×10^4	1.08
PS_{10}-P*t*BA_{78}-PS_{10}	1.20×10^4	1.38×10^4	1.15
HB-(P*t*BA_{78})$_{10}$	2.82×10^4	7.63×10^4	2.70
HB-(P*t*BA_{78})$_{47}$	2.98×10^4	1.98×10^5	6.64
HB-(P*t*BA_{78})$_{10}$-*g*-(PS_{10})$_{11}$	3.13×10^4	9.99×10^4	3.19
HB-(P*t*BA_{78})$_{47}$-*g*-(PS_{10})$_{48}$	4.57×10^4	3.11×10^5	6.88

[a] M_n, M_w and M_w/M_n were obtained from SEC measurements by using narrowly distributed polystyrenes as standards

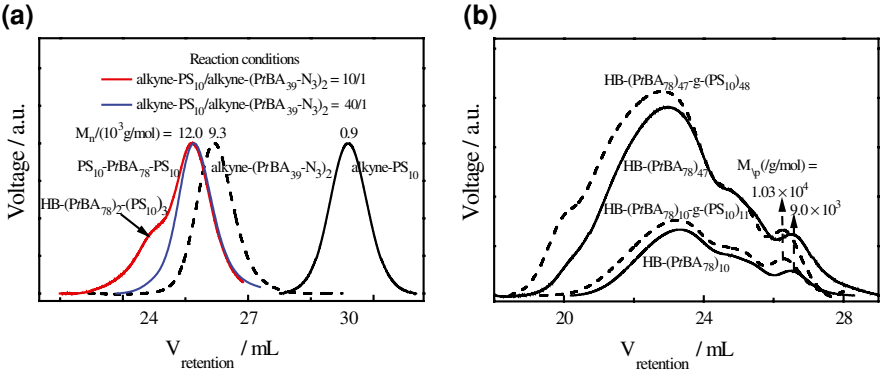

Fig. 4.16 SEC curves of **a** alkyne-PS_{10}, alkyne-(P*t*BA_{39}-N_3)$_2$ and triblock PS_{10}-P*t*BA_{78}-PS_{10} prepared at different alkyne-PS_{10}/alkyne-(P*t*BA_{39}-N_3)$_2$ molar ratios, and **b** HB-(P*t*BA_{78})$_n$ and HB-(P*t*BA_{78})$_n$-*g*-(PS_{10})$_{n+1}$ chains with different *n* values

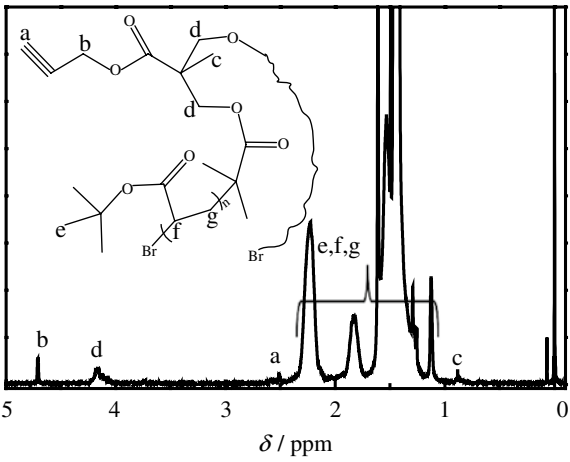

Fig. 4.17 ^{1}H NMR spectrum of alkyne-(P*t*BA_{39}-Br)$_2$ in $CDCl_3$

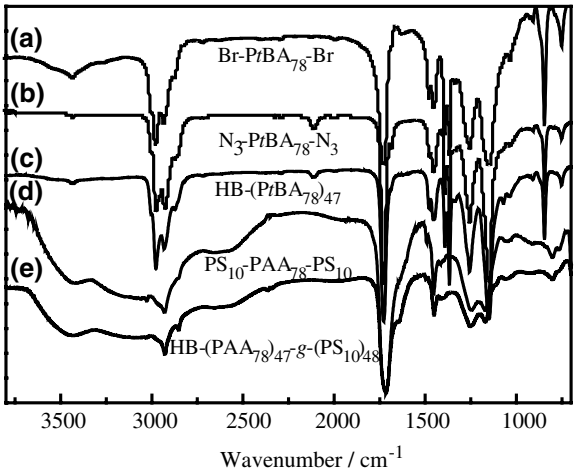

Fig. 4.18 IR spectra of (*a*) alkyne-(P*t*BA$_{39}$-Br)$_2$; (*b*) alkyne-(P*t*BA$_{39}$-N$_3$)$_2$; (*c*) HB-(P*t*BA$_{78}$)$_{47}$; (*d*) PS$_{10}$-PAA$_{78}$-PS$_{10}$; and (*e*) HB-(PAA$_{78}$)$_{47}$-*g*-(PS$_{10}$)$_{48}$

Moreover, the efficient substitution reaction of bromine into azide group in DMF was confirmed by IR spectra in Fig. 4.18, where a strong N=N=N anti-symmetric stretching absorbance near ~2,100 cm^{-1} emerges after azidation reaction (Fig. 4.18b). Further interchain "click" coupling of alkyne-(P*t*BA$_{39}$-N$_3$)$_2$ chains in a concentrated solution resulted in hyperbranched HB-(P*t*BA$_{78}$)$_n$ with different molar masses. As defined in the previous sections [3, 5], n represents the polycondensation degree, i.e., how many initial macromonomer chains were, on weight-average, coupled together ($n = M_{\text{w,hyperbranched chain}}/M_{\text{w,macromonomer chain}}$). We intentionally prepared a hyperbranched core with different sizes by controlling the initial macromonomer concentration. As shown in Fig. 4.16b, HB-(P*t*BA$_{78}$)$_{10}$ with M_w/M_n of ~2.70 and HB-(P*t*BA$_{78}$)$_{47}$ with M_w/M_n of ~6.88 were prepared at a polymer concentration of 0.1 and 0.4 g/L, respectively, where the absolute weight-average molar masses were determined by LLS (Fig. 4.19). Similar to our observation of hyperbranched homopolymers and block copolymers, the strength of N=N=N anti-symmetric stretch of hyperbranched graft copolymers almost decreases to 50 % of its initial value (Fig. 4.18c), indicating ~50 % of initial azide groups remain after "click" reaction, and also we observed ~10 % of initial macromonomer chains remained after the "click" reaction.

On the other hand, short linear alkyne-PS$_{10}$ polymer chains were separately synthesized through ATRP of St with PBIB as initiator (Fig. 4.20a). Figure 4.20b shows the corresponding ^{1}H NMR spectrum, where the proton signal located at 4.40–4.52 ppm (a) belongs to the methine of initiator, and signals located at 6.30–7.50 ppm (d) belong to the benzene rings on monomers. The absolute *DP* was calculated to be ~10 from the integral height of

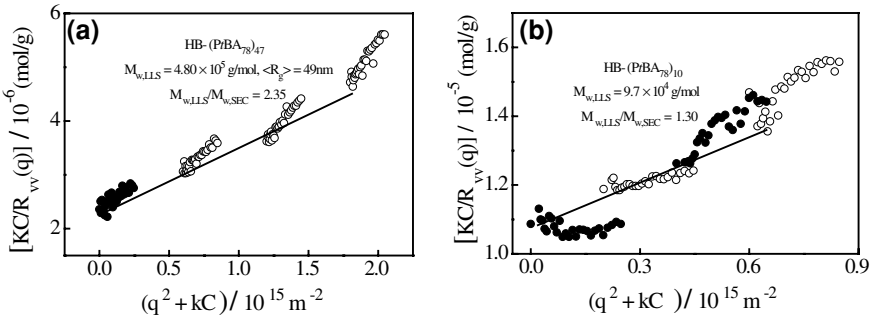

Fig. 4.19 Zimm plots of HB-(P*t*BA$_{78}$)$_{47}$ and HB-(P*t*BA$_{78}$)$_{10}$ chains in THF

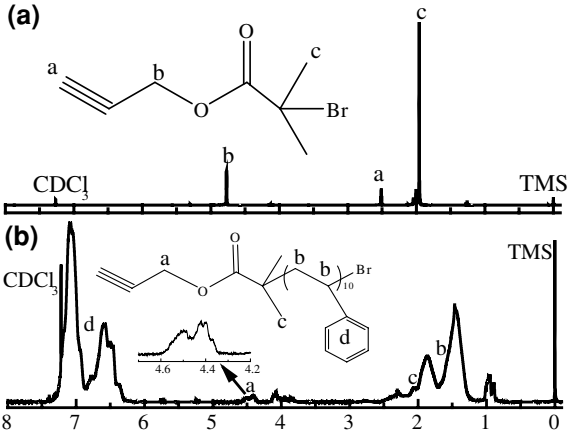

Fig. 4.20 ^{1}H NMR spectra of **a** alkyne-functional initiator (PBIB), and **b** alkyne-PS$_{10}$ in $CDCl_3$

peak (a) and (d). Moreover, SEC curve of alkyne-PS$_{10}$ suggests a narrow distribution (M_w/M_n ~ 1.21).

Further grafting alkyne-PS chains onto the peripheral azide groups of HB-(P*t*BA)$_n$ results in graft copolymer with a large hyperbranched P*t*BA core and very short grafted PS chains. To ensure ~100 % grafting efficiency, 3-fold excess of alkyne-PS was used in the "click" process. The success of grafting reaction is reflected first in the absolute disappearance of N=N=N stretch in FT-IR spectra (Fig. 4.18e); and second in the evolution of SEC curves before and after "click" grafting reaction (Fig. 4.16b), namely, the SEC curve of HB-(P*t*BA)$_n$-*g*-(PS)$_{n+1}$ shifts to a lower retention volume compared to the initial HB-(P*t*BA)$_n$ chains, indicating an increase of apparent molar mass. It is worth noting that, for an individual HB-(P*t*BA)$_n$ chain, the number of remaining azide groups is just equal to (n + 1),

which could finally determine the number of grafted PS chains. It is also interesting to notice that the retention peak of macromonomer shifts from 9.0×10^3 to 1.03×10^4 g/mol, indicating each remaining macromonomer still has one unreacted azide group to further couple with an alkyne-PS chain; in other word, the macromonomer originated from a mixture of broad distributed HB-(P*t*BA)$_n$ chains actually owns a tadpole topology with its tail attached one remaining azide group, confirming our previous observation of intrachain cyclization of polystyrene macromonomer from another perspective.

Then we directly carried out "click" reaction between 40-fold excess of alkyne-PS and alkyne-(P*t*BA-N_3)$_2$ to result in PS-P*t*BA-PS triblock; while 5-fold excess is not enough to suppress the self-polycondensation of alkyne-(P*t*BA-N_3)$_2$ chains (Fig. 4.16a). However, one problem to deal with is how to remove the excess of alkyne-PS chains from the mixtures of reaction products. Further TFA de-protection of tertiary butyl group into carboxyl group leads to the corresponding HB-(PAA)$_n$-*g*-(PS)$_{n+1}$ and PS-PAA-PS, which would facilitate the removal of excess alkyne-PS chains. In the precipitation-purification step, we repeated dissolution-precipitation cycle three times to remove excess alkyne-PS, where cyclohexane was used as precipitant, which is a good solvent for short PS, but a very poor solvent for HB-(PAA)$_n$-*g*-(PS)$_{n+1}$ and PS-PAA-PS copolymers. Finally, purified white-powder of amphiphilic copolymer HB-(PAA)$_{10}$-*g*-(PS)$_{11}$ ($M_w = 6.30 \times 10^4$ g/mol), HB-(PAA)$_{47}$-*g*-(PS)$_{48}$ ($M_w = 2.60 \times 10^5$ g/mol) and their linear triblock analogues PS-PAA-PS ($M_w = 7.50 \times 10^3$ g/mol) were obtained.

4.4 Preparation of Hyperbranched Hetero-subchain Copolymers

The interchain "clicking" of N_3-PS-≡-PCL-N_3 in DMF at 60 °C led to large hyperbranched hetero-subchain copolymer chains HB-(PS-*b*-PCL)$_n$ (Fig. 4.21). Figures 4.22, 4.23 and 4.24 show the characterization results. Note that the difference in the elution curves of HB-(PS-*b*-PCL)$_n$ measured by RI and MALLS detectors, as shown in Fig. 4.22, is due to the fact that the signal from RI detector is proportional to the weight concentration of polymer, while that from MALLS detector is proportional to the weight concentration of polymer multiplied by the weight average molar mass of polymer.

Figure 4.23a, b show that the interchain "clicking" is promoted in a more concentrated precursor solution, similar to our previous observation of hyperbranched homopolymers and block copolymers. However, there is no obvious difference of $(DP)_w$ between HB-(PS_{39}-*b*-PCL_{28})$_n$ and HB-(PS_{18}-*b*-PCL_{28})$_n$ chains for a given initial precursor concentration, indicating the PS block length does not affect the reactivity of the azide end group on the PS subchain. Both M_w/M_n and $(DP)_{w,MALLS}/(DP)_{w,RI}$ of such formed HB-(PS_{39}-*b*-PCL_{28})$_n$ chains increase significantly with the initial precursor concentration (Fig. 4.24),

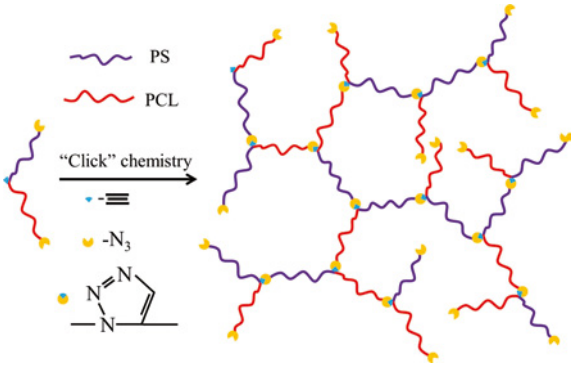

Fig. 4.21 Schematic of synthesis of hyperbranched hetero-subchain copolymer HB-(PS-*b*-PCL)$_n$

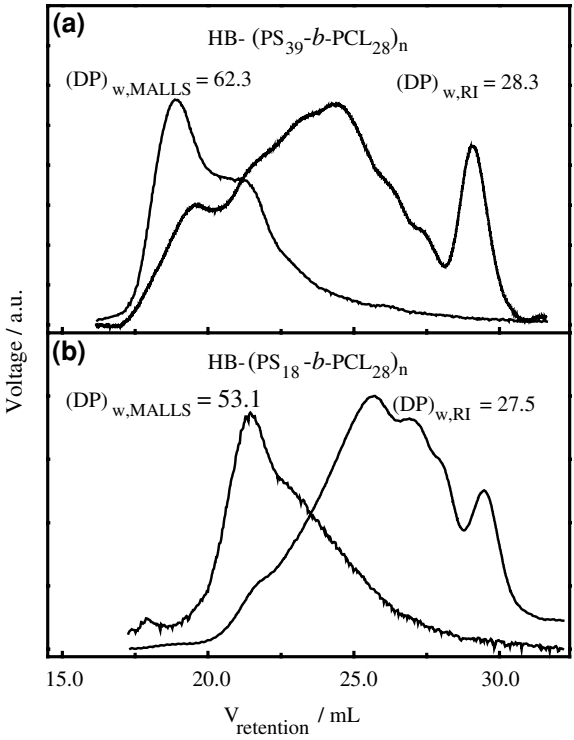

Fig. 4.22 GPC curves of HB-(PS-*b*-PCL)$_n$ with different PS subchain lengths, where $(DP)_{w,MALLS}$ and $(DP)_{w,RI}$ collected from MALLS and RI detector in one measurement

similar to the previous results for hyperbranched polystyrene homopolymers. The successful "click" coupling of precursors N_3-PS-≡-PCL-N_3 is also shown in a sharp decrease of the N=N=N asymmetric stretching vibration signal near ~2,100 cm^{-1}, as shown in Fig. 3.13c.

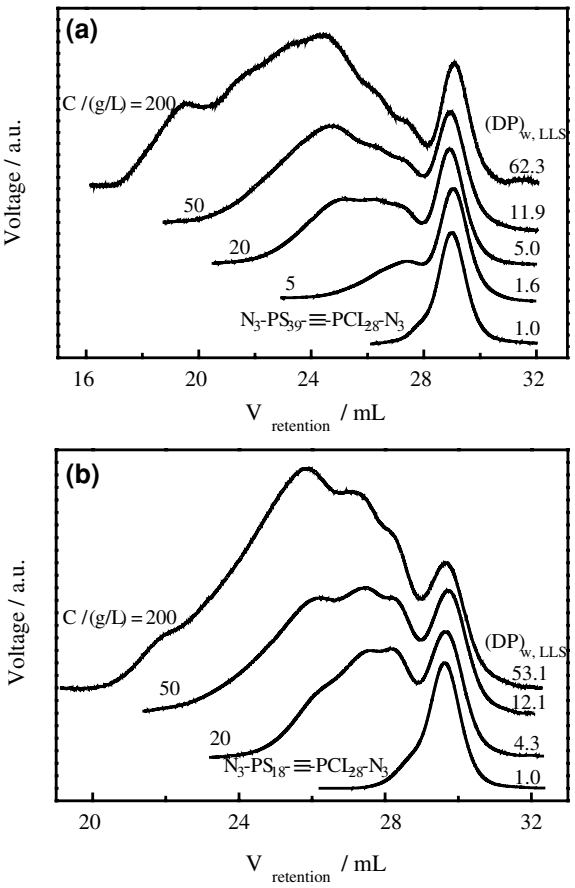

Fig. 4.23 Initial precursor concentration (*C*) dependent GPC-RI curves of **a** HB-$(PS_{39}$-*b*-$PCL_{28})_n$ and **b** HB-$(PS_{18}$-*b*-$PCL_{28})_n$ after 24-h reaction

4.5 Preparation of Degradable Hyperbranched Polystyrene Homopolymers with Cleavable Disulfide Linkages

Using Seesaw-type macromonomer ≡-S-S-$(PS\text{-}N_3)_2$ with one clevable disulfide linkage at the chain center, we successfully prepared degradable hyperbranched polystyrene chains with uniform subchains and controlled locations of cleavable disulfide linkages (Fig. 4.25).

Figure 4.26 shows that the two elution curves respectively from the RI and MALLS detectors are very different, which has been explained before. Figure 4.26b shows the reaction time dependent SEC curves of HB-$(S\text{-}S\text{-}PS)_n$ during the self-polycondensation. As the reaction proceeds, the macromonomer peak becomes smaller while the hyperbranched polymer peaks emerged after a few hours. Gradually, DP_w increases to ~28 and its polydispersity index (M_w/M_n) changes from 1.14 to 4.90 (Fig. 4.27) when most of the

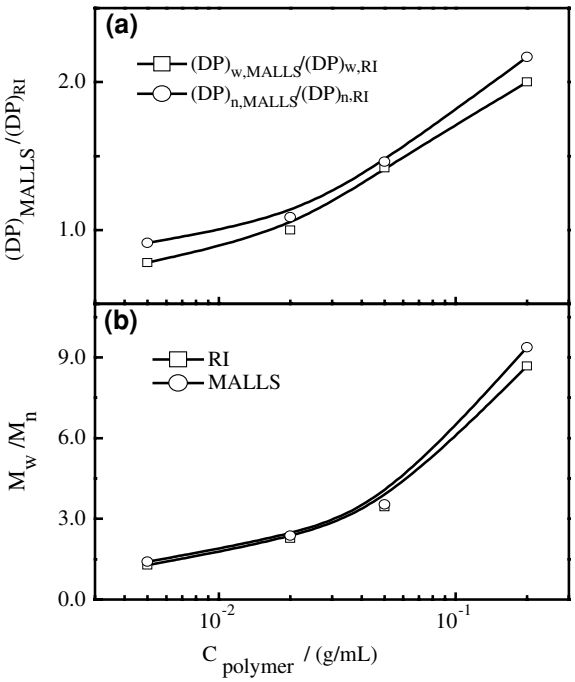

Fig. 4.24 Polymer concentration ($C_{polymer}$) dependence of $(DP)_{MALLS}/(DP)_{RI}$ and polydispersity index (M_w/M_n) for HB-$(PS_{39}$-*b*-$PCL_{28})_n$ from RI and MALLS detectors

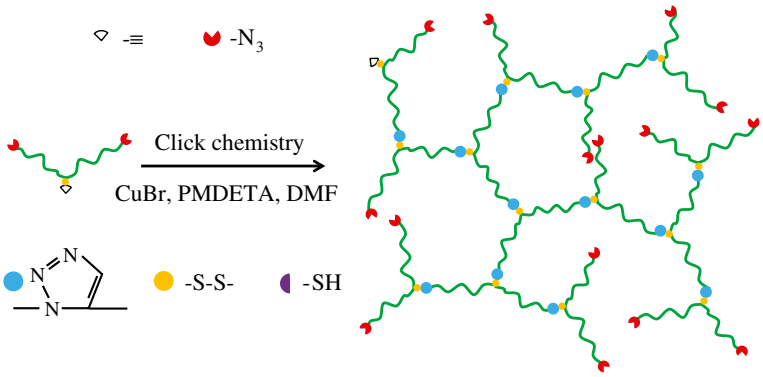

Fig. 4.25 Schematic illustration of the synthesis of disulfide-functional hyperbranched polystyrene chains HB-(S-S-PS)$_n$

initial macromonomers are coupled together. The self-polycondensation nearly ceases after ~14 h, similar to what we observed for hyperbranched polystyrene homopolymers.

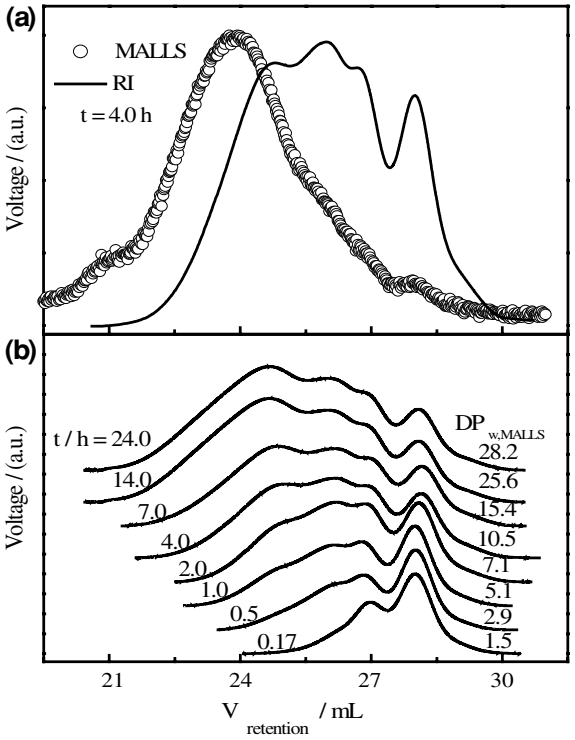

Fig. 4.26 **a** Comparison of two typical SEC curves of HB-(S-S-PS)$_n$ monitored by two different detectors: RI (*solid line*) and MALLS (*circle symbol*), and **b** reaction time (t) dependent SEC-RI curves of HB-(S-S-PS)$_n$, where $T = 35$ °C and $C_{\text{polymer}} = 0.30$ g/mL

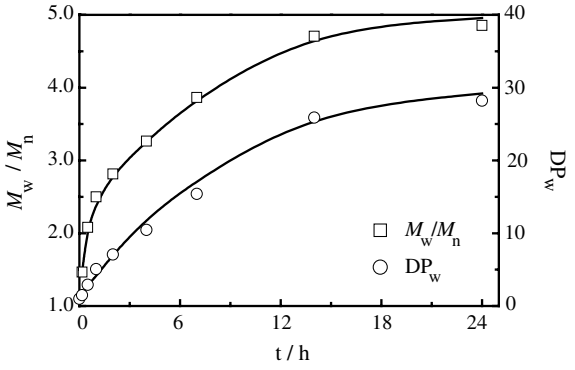

Fig. 4.27 Reaction time (t) dependence of polydispersity index (M_w/M_n) and average degree of polycondensation (DP_w) of HB-(S-S-PS)$_n$, where $T = 35$ °C and $C_{\text{polymer}} = 0.30$ g/mL

It is worth noting that each branching point of HB-(S-S-PS)$_n$ contains just one disulfide bond that is cleavable when a reducing agent is added. The cleavage of each disulfide bond results in two smaller fragmented hyperbranched chains with a thiol end group. Using a combination of static and dynamic LLS, we could further study such a degradation kinetics of a fractionated HB-(S-S-PS)$_n$ with a DP_w of 35 and a M_w/M_n of 1.40, which will be discussed in the next chapter.

References

1. Li L, Lu Y, An L, Wu C (2013) J Chem Phys 138:114908
2. He C, He W-D, Li L-W, Jiang W-X, Tao J, Yang J, Chen L, Ge X-S, Chen S-Q (2012) J Polym Sci Pol Chem 50:3214
3. Li L, He C, He W, Wu C (2011) Macromolecules 44:8195
4. He C, Li L-W, He W-D, Jiang W-X, Wu C (2011) Macromolecules 44:6233
5. Li L, Zhou J, Wu C (2012) Macromolecules 45:9391
6. Li L, Wang X, He C, He W (2014) J Polym Sci Pol Chem 52:128
7. Golas PL, Matyjaszewski K (2007) QSAR Comb Sci 26:1116
8. Kolb HC, Finn MG, Sharpless KB (2004) Angew Chem Int Edit 2001:40
9. Bock VD, Hiemstra H, van Maarseveen JH (2006) Eur J Org Chem 51
10. Hutchings LR, Dodds JM, Roberts-Bleming SJ (2006) Macromol Symp 240:56
11. Hutchings LR (2008) Soft Matter 4:2150
12. Clarke N, Luca ED, Dodds JM, Kimani SM, Hutchings LR (2008) Eur Polym J 44:665
13. Hutchings LR, Dodds JM, Roberts-Bleming SJ (2005) Macromolecules 38:5970
14. Chen F, Liu G, Zhang G (2012) J Polym Sci Pol Chem 50:831
15. Greene AC, Zhu J, Pochan DJ, Jia X, Kiick KL (1942) Macromolecules 2011:44

Chapter 5
Solution Properties of "Perfect" Hyperbranched Homopolymers and Copolymers

In the previous two chapters, we discussed the design strategy synthetic detail of various Seesaw-type macromonomers and "perfect" hyperbranched (co)polymers. In this chapter, we will focus on the solution properties of these novel hyperbranched (co)polymers in dilute and semidilute solutions.

5.1 Fractal Property of "Perfect" Hyperbranched Chains: Scaling Laws of Sizes and Intrinsic Viscosities

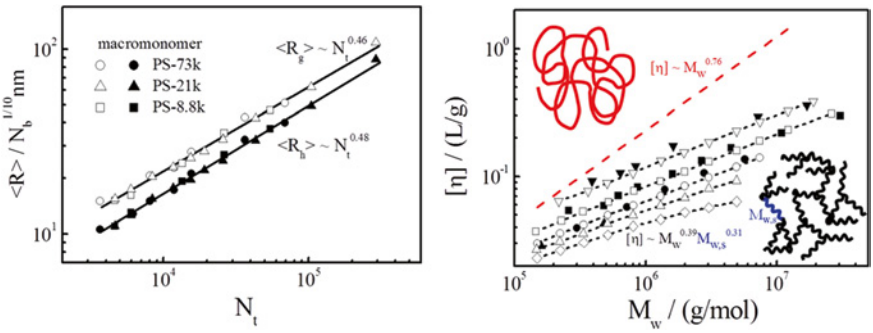

5.1.1 Theoretical Background

Whenever addressing the structure-property relationships of a polymer, its rheological behavior must be one of the first considerations, more specifically, its intrinsic viscosity $[\eta]$, also called the Staudinger index, because it is often used in industry as a

L. Li, *Studies on "Perfect" Hyperbranched Chains Free in Solution and Confined in a Cylindrical Pore*, Springer Theses, DOI: 10.1007/978-3-319-06097-2_5,

quality and process control and in research as a structural characterizing parameter. It has been known that [1, 2]

$$[\eta] = \Phi\left(\frac{R_g^3}{M}\right) \tag{5.1}$$

where Φ is the Flory hydrodynamic constant, R_g is the root-mean square radius of gyration, and M is the molar mass of polymer. $[\eta]$ is inversely proportional to the chain density in a given solvent. Φ is roughly related to the chain draining in solution, namely, a higher degree of draining leads to a smaller Φ. Therefore, a linear chain should have a smaller Φ than its hyperbranched counterpart. However, it remains a challenge to properly and quantitatively describe the draining nature of a hyperbranched chain in good solvents. Generally, we know that R_g is scaled to M so that Eq. 5.1 is written as in the Mark-Houwink-Sakurada (MHS) equation [1, 2]

$$[\eta] = KM^{\alpha} \tag{5.2}$$

where K and α are two constants for a given type of polymer solution. Their values depend on the solvent quality and chain topology. Specifically, for linear chains, $\alpha = 0.7$–1.0 in good solvents; and $\alpha = 0.5$ under the theta condition [3–5].

However, Eqs. 5.1 and 5.2 completely fail to predict how $[\eta]$ depends on M for dendrimers [6], because of an improper assumption that the hydrodynamic radius (R_h) is proportional to the radius of gyration (R_g), which means dendrimers are not fractal objects. Experimental study demonstrates there exists a maximum in the plot of $[\eta]$ versus M, i.e., $[\eta]$ first increases with the number of generation (G) and then decreases after G reaches a certain value [7]. Such an anomalous behavior has not been described by the Fox-Flory formula [8] and the existing Zimm or Rouse arguments for a long time. Recently, An et al. [9] developed a two-zone model for dendrimers after considering the radial segmental density profile and quantitatively explained those existing experimental results. Further, by combining Debye's theory for free draining polymer chain with Einstein's theory for hard spheres, they presented a general theory for the intrinsic viscosity of polymers with any morphology on the basis of a partially permeable sphere model [10]. Such predictions agree well with the experimental results in literature, ranging from linear to star and to dendritic chains.

As mentioned in Chap. 1, randomly hyperbranched chains are even more complicated than dendrimers. It has not been completely clear whether they are fractal objects [11, 12]; and whether those previously reported M-dependent intrinsic viscosities from an on-line combination of the size exclusion chromatograph (SEC) with viscosity and multi-angle laser light scattering (MALLS) detectors actually captured its structure-property relationship [11, 13]. In the next section, we'll discuss our experimental results in detail.

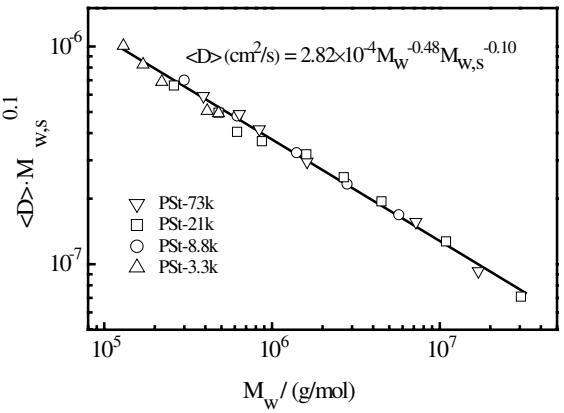

Fig. 5.1 Weight average molar mass (M_w) dependence of average translational diffusion coefficient ($\langle D \rangle$) of hyperbranched polystyrenes with different subchain lengths in toluene at T = 25 °C, where $\langle D \rangle$ has a unit of "cm^2/s" and both $M_{w,s}$ and M_w are expressed as "g/mol"

5.1.2 Experimental Result

In order to clarify the fractal nature of hyperbranched polymers, we first fractionated the polydisperse "perfect" hyperbranched polystyrene homopolymers into a series of narrowly distributed samples, and determine their molar mass-dependent molecular parameters by a combination of LLS and viscosity measurements.

First, we measured their molar masses dependent average diffusion coefficients ($\langle D \rangle$) by combining static and dynamic laser light scattering. Figure 5.1 shows that after normalized by the weight average molar mass ($M_{w,s}$) of the subchain, the double logarithmical plots of $\langle D \rangle$ versus the weight average molar mass of the entire hyperbranched chains (M_w) for different hyperbranched chains unquestionably collapse into a single line, which clearly indicates that $\langle D \rangle$ is scaled to both M_w and $M_{w,s}$. Moreover, a much smaller absolute value of the exponent of $M_{w,s}$ (0.1) indicate the diffusion behavior of hyperbranched chains is mainly dominated by the overall molar mass (M_w) but not the subchain length ($M_{w,s}$). To our knowledge, such a scaling has not been well established before even though many people have tried in the past.

Further, Fig. 5.2 shows the average size ($\langle R \rangle$) of the hyperbranched polystyrene chains is scaled to the overall degree of polymerization (N_t), where $N_t = M_w/M_o$ with M_o is the molar mass of styrene; the average hydrodynamic radius ($\langle R_h \rangle$) is calculated from $\langle D \rangle$ by using the Stokes–Einstein equation; the average radius of gyration ($\langle R_g \rangle$) is measured using static LLS; and $\langle R \rangle$ is normalized by the polymerization degree of the subchain on the basis of the theoretical prediction [14, 15]; namely, $\langle R_g \rangle$ of hyperbranched polymer chains in good solvents is scaled to the polymerization degrees of the overall hyperbranched chain (N_t) and the subchain (N_b) as $\langle R \rangle \sim N_t^{\alpha} N_b^{\beta}$ with $\alpha = 1/2$ and $\beta = 1/10$, which has not been proved experimentally. Indeed, the average size of the hyperbranched polystyrenes with different subchain lengths is scaled to the overall polymerization degree but the scaling exponent (α), respectively, for $\langle R_g \rangle$ and $\langle R_h \rangle$, is 0.46 ± 0.01 and 0.48 ± 0.01,

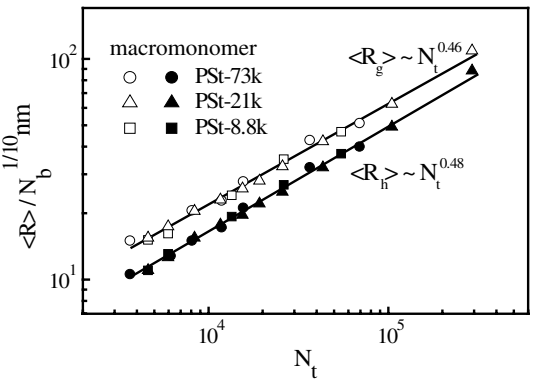

Fig. 5.2 Overall degrees of polymerization (N_t) dependence of normalized average radius of gyration $\langle R_g \rangle$ and average hydrodynamic radius $\langle R_h \rangle$ of hyperbranched polystyrene chains with different uniform subchain lengths in toluene at $T = 25$ °C

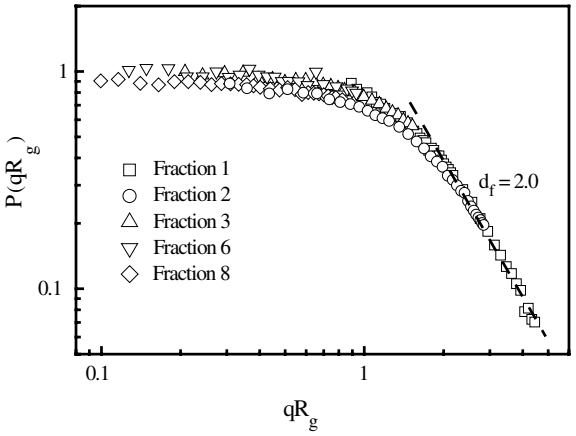

Fig. 5.3 qR_g-dependence of scattering factor $P(qR_g)$ of different fractions of hyperbranched polystyrenes synthesized using PS-18.7K

smaller than the predicted 1/2. On the other hand, we also attained the scaling exponent β by fixing the overall molar mass of the hyperbranched polystyrenes and plotting $\langle R \rangle$ versus N_b (not shown). We found that β is 0.11 ± 0.01 for $\langle R_g \rangle$ and 0.09 ± 0.01 for $\langle R_h \rangle$, supporting the normalization used. Again, to our knowledge, such scaling laws have not been seriously established before even though much effort has been spent before.

On the other hand, we can extract the fractal dimension (d_f) of hyperbranched chains by plotting the scattering factor $P(qR_g)$ versus qR_g [16–19], as shown in Fig. 5.3. Note that both $P(qR_g)$ and qR_g are dimensionless so that such a plot should be universal for a given type of chain topology. Indeed, the scattering factors of different fractions collapse into a master curve in the range of qR_g studied, indicating that all the fractions are self-similar to each other and follow the same scaling law at $q\langle R_g \rangle > 1.5$. The negative slope represents the ensemble fractal dimension (d_f) of ~2.0 that is close to the theoretical prediction for the reaction-limited cluster-cluster aggregation [18, 20], consistent with our extracted exponents from Fig. 5.2.

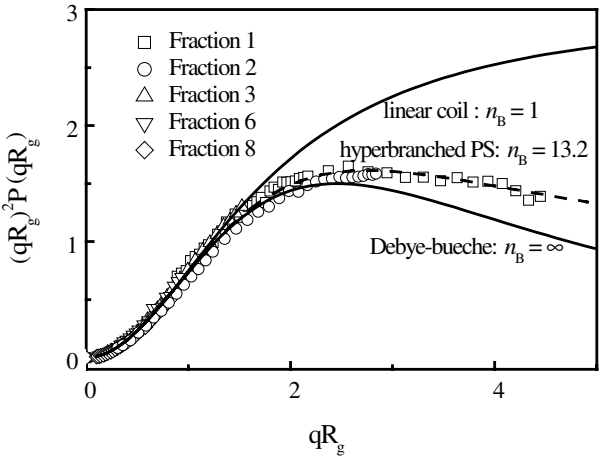

Fig. 5.4 Kratky plots for different hyperbranched polystyrenes synthesized using PS-18.7K, where *two solid lines* represent fitting curves for linear coiled chains and Debye-bueche hard spheres, respectively

The effect of branching is even better displayed in the Kratky plot; namely $(qR_g)^2P(qR_g)$ versus qR_g, as shown in Fig. 5.4. Theoretically, Burchard [18] deduced the scattering factor for AB_2-type hyperbranched chains as

$$p(qR_g) = \frac{1 + \frac{(qR_g)^2}{3n_B}}{[1 + (\frac{1+n_B}{6n_B})(qR_g)^2]^2} \tag{5.3}$$

where n_B is the number of branching points per hyperbranched chain and expressed as

$$n_B = \frac{(\phi + \varphi) - (\phi^2 + \varphi^2)}{(\phi^2 + \varphi^2)[1 - (\phi + \varphi)]} \tag{5.4}$$

where ϕ in our case is the probability of group A in one macromonomer (B~~~~A~~~~B) reacted with the first group B in another macromonomer; and φ is the probability of group A reacted with the second group B. Experimentally, we found that $n_B \simeq 13.2$, as shown in Fig. 5.4, where we also plot two limiting cases: $n_B = \infty$ (hard sphere) and 1 (linear chains). It is clear that our hyperbranched chains are less draining and close to a hard sphere.

In principle, $\phi = 0.5$ because the two unreacted A groups on a macromonomer should have an equal probability to react the A group on another macromonomer. Using our fitting result of value of $n_B = 13.2$, we could numerically calculate $\varphi = 0.42$ on the basis of Eq. 5.4, smaller than 0.5, as expected, because the steric effect makes the second B group less reactive. It is worth-noting that in our simple discussion, the effect of excluded volume is neglected [16]. Up to now, all the

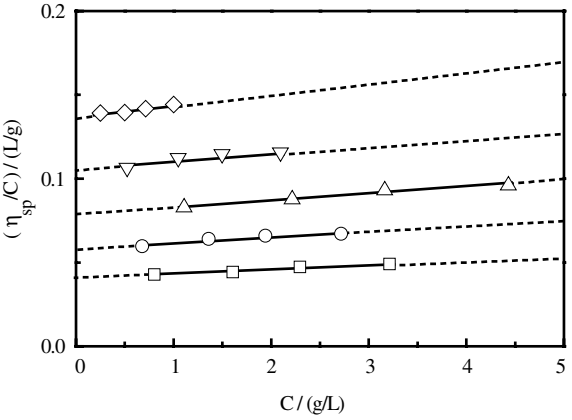

Fig. 5.5 Typical plots of polymer concentration dependence of reduced specific viscosity (η_{sp}/C) of hyperbranched polystyrenes (PSt-8.8k) made of one macromonomer in toluene at $T = 25$ °C

obtained scaling plots indicate that the hyperbranched chains with long subchains are self-similar, which leads us to believe that hyperbranched polymers should also obey the MHS equation.

To verify it, we further measured their concentration dependence of viscosity in toluene at $T = 25.0 \pm 0.1$ °C by a conventional flow viscometer. It should be emphasized that the used most concentrated solution was still dilute enough, a region far away from the semi-dilute region, i.e., $C \ll C^*$ (the overlap concentration), to keep the relative viscosity below 1.30. Figure 5.5 shows typical plots of the concentration dependence of specific viscosity η_{sp}/C of hyperbranched polystyrenes made of one macromonomer, where η_{sp} is defined as $\eta_r - 1$. The intercept and slope of each fitting line respectively lead to the intrinsic viscosities ($[\eta]$) and the Huggins constant (k_h) of a given hyperbranched polystyrene on the basis of $\eta_{sp}/C = [\eta] + k_h[\eta]^2 C$. Note that for some samples we did not have a sufficient quality to make a large number of solutions so that their k_h values were estimated with some uncertainty, which scarcely affects those measured intrinsic viscosity ($[\eta]$) because polymer solutions used were sufficiently dilute.

Theoretically, we calculated the intrinsic viscosity of these hyperbranched polystyrene chains using the theory for the intrinsic viscosity of polymers proposed by us recently based on the partially permeable sphere model [21, 22]. By combining Einstein's theory for hard spheres with Debye's theory for free draining polymer chains, our theory, by introducing two phenomenological functions, a drainage function and a drag function, both of which can be determined from the density profile, provides a simple and convenient method that circumvents the explicit treatment of the complex, multi-body hydrodynamic interactions in these systems while capturing their key effects. The parameter choice was detailed before.

Figure 5.6a shows our experimental and theoretical results of how $[\eta]$ depends on both M_w and $M_{w,s}$ for hyperbranched polystyrene chains with different subchain lengths, indicating that hyperbranched chains obey the MHS equation just like their linear counterpart, i.e., they are fractal objects. Apparently, the data points spread over a wide range but with a similar slope of 0.39. Also note that a slight deviation from the scaling occurs when $M_{w,s}$ is less than ~10^3 g/mol, presumably due to the emergence of a strong effect of the excluded volume.

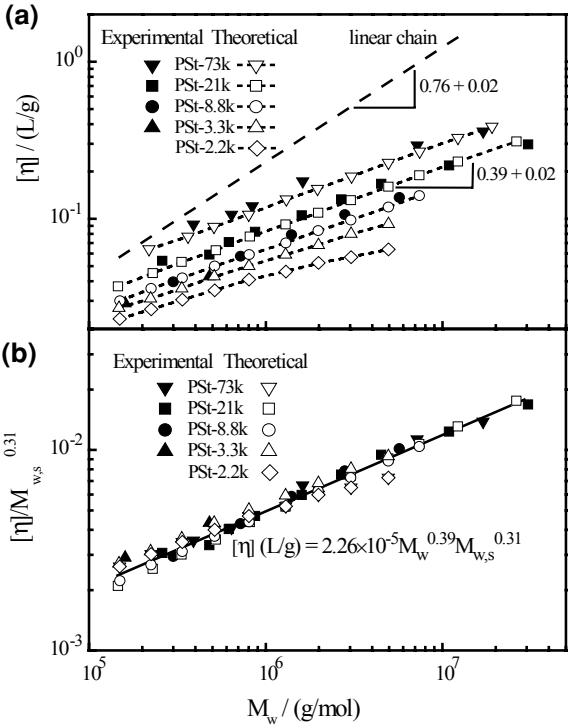

Fig. 5.6 Weight-average molar mass (M_w) dependence of intrinsic viscosity ($[\eta]$) of hyperbranched polystyrenes with different subchain lengths in toluene at $T = 25$ °C, where *dashed line* for linear chains is from literature [5]. Theoretical results were calculated using our partially permeable sphere model with a density profile accurately calculated from Monte Carlo simulation [21, 22]

Furthermore, Fig. 5.6b clearly reveals that these scattered data in Fig. 5.6a collapse into a single master line when $[\eta]$ is normalized by is corresponding subchain length; namely, $[\eta]$ is scaled to both M_w and $M_{w,s}$ as

$$[\eta] = K_\eta M_w{}^{\nu} M_{w,s}{}^{\mu} \tag{5.5}$$

where $\nu = 0.39 \pm 0.01$ and $\mu = 0.31 \pm 0.01$; and $K_\eta = 2.26 \times 10^{-5}$ L/g. Up to now, we have experimentally and theoretically revealed that both Eqs. 5.1 and 5.2 are also valid for hyperbranched chains with long and uniform subchains in a good solvent, clearly indicating that these hyperbranched chains are fractal objects; in contrast a slight deviation from the scalings occurs for hyperbranched chains with a much shorter subchain length, because of the excluded volume effect. It should be emphasized that the fractal behavior of hyperbranched chains have been previously well theoretically discussed via the branching theory [23, 24] and further experimentally verified by the scattering experiments finished by Burchard' group [16, 19, 25]; however, the subchain lengths in previous studies were extremely short and unchangeable; therefore, their adopted AB_2 monomer is actually different with what we mentioned. It is also interesting to note that the two scaling exponents between $[\eta]$ and both M_w and $M_{w,s}$ are not far away from each other. The literature values of the measured scaling exponent between $[\eta]$ and M_w is very widely spread over a range 0.3–0.5 for hyperbranched polymers prepared by conventional methods with a broad distribution of subchain length. With no exception, all of previous experiments used the online SEC-viscosity-MALLS to measure both $[\eta]$

and M_w [12, 13, 26]. Unfortunately, it had been repeatedly overlooked that SEC separates polymer chains by their hydrodynamic volumes, not by their molar masses. Namely, for non-linear polymer chains, each retentive fraction in principle contains polymer chains with a similar hydrodynamic volume but not necessarily with a similar molar mass. Theoretically, Eqs. 5.1 and 5.2 require that each fraction contains polymer chains with a similar molar mass, not a similar size. Presumably, it is due to difficulties and limitations in both the sample preparation and experimental methods so that less attention has been paid to this very important point so far.

In contrast, all the hyperbranched polystyrenes used in the current study were fractionated by precipitation, i.e., according to the interaction parameter χM, where M is the overall molar mass of the chain and χ is the Flory-Huggins parameter, a constant, independent on M for a polymer in a given solvent. Therefore, hyperbranched chains in each fraction used here have a similar molar mass. In comparison with our results, some of previous computer simulations [27, 28] suggested that the molar mass dependence of intrinsic viscosity of irregular hyperbranched chains deviates from Eq. 5.2 because the segment density distribution is different from those predicted by de Gennes and Hervet. We will come back to this point later.

Previously, we have already used static LLS to reveal that for hyperbranched polystyrene chains with long and uniform subchains, $R_g \sim R_h \sim {M_w}^{\gamma} {M_{w,s}}^{\varphi}$ with $\gamma = 0.47 \pm 0.01$ and $\varphi = 0.10 \pm 0.01$. Therefore, we have

$$[\eta] \sim {M_w}^{3\gamma-1} {M_{w,s}}^{3\varphi} \tag{5.6}$$

A combination of Eqs. 5.1 and 5.6 leads to $\nu = 3\gamma - 1$ and $\mu = 3\varphi$. Inputting our experimentally determined values of γ and φ, we have $\nu = 0.41 \pm 0.01$ and $\mu = 0.30 \pm 0.01$, fairly close to those directly measured values (0.39 ± 0.01 and 0.31 ± 0.01) from the viscosity measurements, which cross-examines and validates our previous LLS data and current viscosity results. It is worth-noting that in comparison with LLS, viscosity is more sensitive and much easier to be measured in characterizing the effect of chain topology and conformation, such as the branching degree, because LLS measures the hydrodynamic size, while viscosity detects the hydrodynamic volume that is a cubic of the chain size.

When treating each hyperbranched chain as a suspending hard sphere and taking $\Phi = 2.5$ [1], we can rewrite Eq. 5.1 as

$$[\eta] = \frac{10\pi}{3} N_A \left(\frac{{R_\eta}^3}{M_w} \right) \text{ or } R_\eta = \left(\frac{3[\eta] M_w}{10\pi N_A} \right)^{1/3} \tag{5.7}$$

where R_η and N_A are the average viscometric radius and the Avogadro's number, respectively. Therefore, we can convert each measured intrinsic viscosity $[\eta]$ into a viscometric radius R_η so that we can directly compare two average hydrodynamics-related radii ($\langle R_h \rangle$ and $\langle R_\eta \rangle$), as shown in Fig. 5.7. It reveals that $\langle R_\eta \rangle$ is fairly close to $\langle R_h \rangle$ and their ratio ($\langle R_\eta \rangle / \langle R_h \rangle$) is 0.95 ± 0.05, smaller than ~1.2 for linear chains in good solvents [3, 29]. Such a difference illustrates different structures and solution behaviors of linear and branched chains in good solvents, presumably reflecting that a linear chain is more draining, i.e., its hydrodynamic radius is smaller, than its branch counterpart for a given intrinsic viscosity.

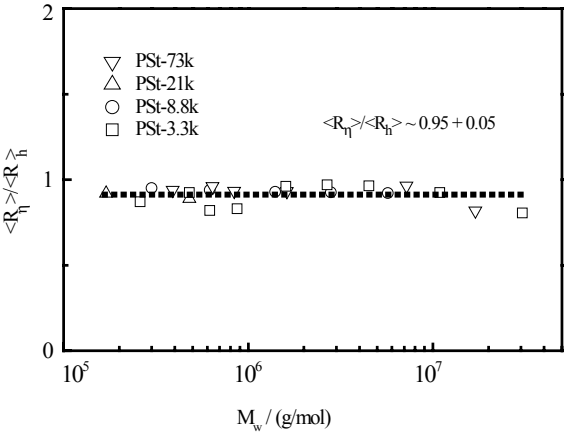

Fig. 5.7 Weight-average molar mass (M_w) dependence of ratio of two hydrodynamics-related radii (average viscometric radius, $\langle R_\eta \rangle$, and average hydrodynamic radius, $\langle R_h \rangle$) of hyperbranched polystyrenes with different subchain lengths in toluene at $T = 25$ °C

5.2 Deformation Property of "Perfect" Hyperbranched Chains: How Do They Pass through a Cylindrical Pore?

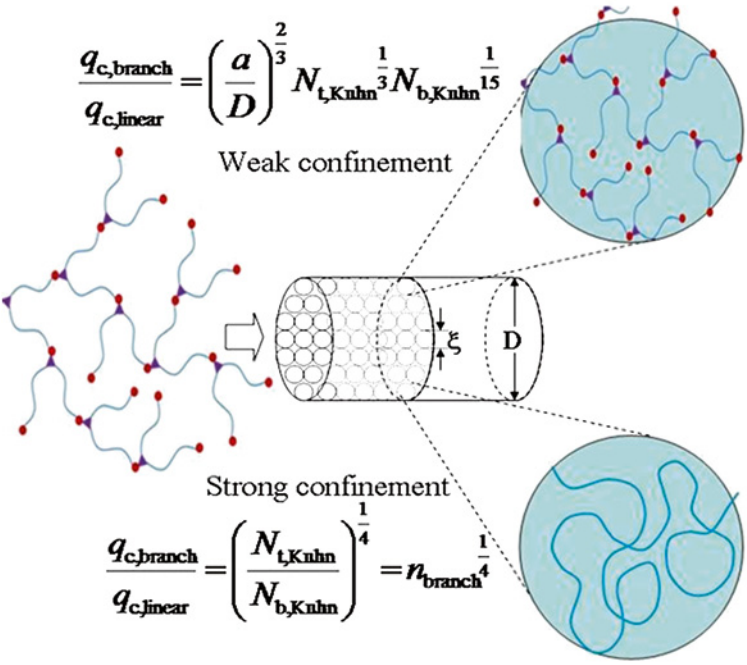

The translocation of flexible polymer chains in solution through a porous media (ultrafiltration) dominates many processes, such as size exclusion chromatography (SEC) [30], ultrafiltration [31] and gene delivery [32], to name but a few.

Generally speaking, whether a polymer chain can pass through a pore smaller than its size under an elongational flow should depend on the flow rate and its deformability (deformable property). The deformability is mainly determined by its chemical and topological structures. Limited by polymer synthesis methodologies, the preparation of "perfect" hyperbranched chains are rather difficult, if not impossible, which has hindered experimental confirmation of some predicted behaviors of hyperbranched polymer chains passing through a small pore. Therefore, establishing the correlation between molecular parameters of hyperbranched chains and their translocation behavior and deformation property still remains an important challenge in modern polymer research. In this section, we'll discuss how a hyperbranched chain pass through a nanopore under an elongational flow field theoretically and experimentally.

5.2.1 *Unified Theoretical Description of Polymer Chains with Different Topologies Passing Through a Nanopore*

Statistical physics tells us that the possibility of a polymer chain passing through a cylindrical pore with a diameter of D much smaller than its size is extremely low because there is a confinement penalty. To overcome the confining energy barrier, one has to "pull" the chain with a kind of interaction, such as the hydrodynamic or electric (if it is charged) force. It was shown by de Gennes [33], Pincus [34], Casassa [35], and Freed [36, 37], that the minimum force (the critical flow rate, q_c, when the Poiseuille flow is used) depends on the chain's topology and deformability as well as the pore size, but unexpectedly not on the chain size in some cases, including linear and star chains. In particular, de Gennes [33] and Pincus [34] showed that for a linear chain, $q_{c,linear} \sim k_B T/\eta$, independent on sizes of both the chain and pore, where k_B, T and η are the Boltzmann constant, absolute temperature and solution viscosity, respectively. However, our previous experimental results revealed that for a linear chain, $q_{c,linear}$ decreases as D increases because the chain segment inside each "blob" should not be treated as a hard sphere with a dimension of D but with an effective length (l_e) along the flow direction [31, 38], i.e.,

$$q_{c,linear} = \frac{k_B T}{3\pi\eta}\frac{D}{l_e} \tag{5.8}$$

Note that here individual "blobs" with a size of ξ is defined as portions of the confined chain whose center of gravity undergoes the Brownian motion under the agitation of the thermal energy. Such a dependence (Eq. 5.8) was supported by the recent first principle calculation [36, 37].

Physically, each polymer chain confined inside a small cylindrical pore can be viewed as a number of packed blobs. Instead of considering free energy of the entire confined chain as previously done by others, we only consider the confinement and hydrodynamic forces on individual blobs ($f_c = k_B T/\xi$ and $f_h = 3\pi\eta l_e u$, where $u = q/D^2$, the flow velocity), i.e., from $f_c = f_h$, and drive the critical flow

rate (q_c). Using such an approach, we have established a unified description of normalized q_c without any priori consideration of the chain topology as follows.

$$\frac{q_c}{q_{c,linear}} = \left(\frac{D}{\xi}\right)^2 \tag{5.9}$$

It shows that the only thing left here is to find ξ for each topology. Obviously, for a confined linear chain, $\xi_{linear} = D$. For a confined star chain with f arms, we have to consider whether the number of forwarded and stretched arms (f_{in}) that are inserted into the pore is larger or smaller than that of backwarded and coiled arms (f_{out}) outside, where $f = f_{in} + f_{out}$. When $f_{in} \geq f_{out}$, we only need to consider those forwarded f_{in} arms that occupied the pore. Each stretched arm acts as a tube with a diameter of ξ_{star}; namely, $D^2 = {\xi_{star}}^2 f_{in}$ so that $q_c/q_{c,linear} = f_{in}$. Similarly, when $f_{in} \leq f_{out}$, we have to consider those backwarded f_{out} arms outside. In this case, the forwarded and stretched arms must be further stretched (i.e., with a higher flow rate) to generate a sufficient force to pull those outside arms into the pore. When they come into the pore, $D^2 = {\xi_{star}}^2 f_{out}$ so that $q_c/q_{c,linear} = f_{out}$. These two different cases can be summarized into one equation as

$$\frac{q_{c,star}}{q_{c,linear}} = \frac{f + |f - 2f_{in}|}{2} \tag{5.10}$$

Recent experimental results confirmed that for a given arm length (L_A), q_{star} increases with f but is nearly independent on L_A [39], contradictory to the de Gennes' prediction [33], in which the full extension of each pulled-in arm was assumed. Our derivation and experimental results reveal that such an assumption is not necessary and incorrect. It should be noted that we previously made one unfortunate mistake in *Polym Chem* **2011**, *2*, 1071 [39]; namely, the denominator in Eqs. 5b and 6b in that manuscript should be ${f_{out}}^2$ instead of ${f_{in}}^2$, which also affects Fig. 6 there.

Transportation of a hyperbranched chain made of subchains with a uniform length (l_b) through a small pore is much more complicated, depending on whether l_b is much larger or smaller than ξ_{branch}. In other words, when $l_b \gg \xi_{branch}$, each blob contains a linear chain segment that is easily deformable (strong confinement); while $l_b \ll \xi_{branch}$, each blob itself contains a number of subchains, i.e., a hyperbranched and less-deformable chain segment (weak confinement). Previously, using the Flory scaling, de Gennes [40, 41] deduced $q_{c,branch}$ for a hyperbranched chain in a good solvent and found that $q_{c,branch} \sim {N_{t,Kuhn}}^{\gamma} {N_{b,Kuhn}}^{\varphi}$, where $N_{t,Kuhn}$ and $N_{b,Kuhn}$ are numbers of Kuhn segments of the entire chain and the subchain; and $\gamma = 1/2$ and $2/3$; and $\varphi = -1/2$ and $2/15$, respectively, for strongly and weakly confined hyperbranched chains inside a cylindrical pore. Unfortunately, the prediction is partially incorrect because the barrier energy (E_b) of one layer (cross-section) of blobs was mistaken as $\sim k_B T$. Actually, $k_B T$ is the barrier energy for one blob. The barrier energy for one layer of blobs should be $k_B T$ multiplied by the number of blobs in one layer, i.e., $E_b = k_B T(D^2/{\xi_{branch}}^2)$. This explains why the correct exponent should be 2, as shown in Eq. 5.9, instead of 4.

As discussed above, each blob in the strong or weak confinement limits contains a linear or a hyperbranched chain segment with a maximum size of D. Assuming that each blob contains n Kuhn segments and each Kuhn segment has a size of a, the volume fractions of the Kuhn segments inside each blob and inside the volume occupied by the entire confined and stretched chain should be identical, i.e., $a^3n/\xi^3 = a^3N_{t,Kuhn}/(D^2L_o)$, for a uniform chain density, where L_o is the optimal length of the entire chain stretched along the flow direction, i.e.,

$$\xi = \left(\frac{nD^2L_o}{N_{t,Kuhn}}\right)^{\frac{1}{3}} \tag{5.11}$$

Let us first find L_o. After a chain is confined inside the pore and stretched to a length of L, its free energy (F) has an enthalpy term: $k_BT[N_{t,Kuhn}{}^2a^3/(D^2L)]$ and an entropy term: $k_BT(L/R_0)^2$, where R_0 is the unperturbed chain size. L_o can be found from $dF/dL = 0$, i.e.,

$$L_o \cong a\left(\frac{N_{t,Kuhn}R_0}{D}\right)^{\frac{2}{3}} \tag{5.12}$$

Note that $R_0 = aN_{t,Kuhn}{}^{1/4}N_{b,Kuhn}{}^{1/4}$ and $aN_{t,Kuhn}{}^{1/2}$ for branched and linear chains, respectively. Actually, a linear chain can also be viewed as a special branched chain with one "branching" point, i.e., $N_{t,Kuhn} = N_{b,Kuhn}$; namely, we can also using $R_0 = aN_{t,Kuhn}{}^{1/4}N_{b,Kuhn}{}^{1/4}$ for a linear chain. It is also known that for a hyperbranched or a linear chain in good solvents, its root mean square radius of gyration $\langle R_g^2\rangle^{1/2}$ is scaled to $N_{t,Kuhm}$ and $N_{b,Kuhm}$ as $aN_{t,Kuhn}{}^{\alpha}N_{\beta,Kuhm}{}^{\beta}$ with $\alpha = 1/2$ and 3/5, and $\beta = 1/10$ and 0, respectively [1, 15, 42]. Similarly, we can also generally express the blob size (ξ) in good solvents as $\xi = aN_{t,\,Kuhn}{}^{\alpha}N_{\beta,Kuhn}{}^{\beta}$. A combination of Eqs. 5.9, 5.11 and 5.12 as well as two scaling equations of R_0 and ξ results in

$$\frac{q_{c,branch}}{q_{c,linear}} = \left(\frac{a}{D}\right)^{\frac{2(3-5\alpha)}{3(3\alpha-1)}} N_{t,Kuhn}{}^{\gamma}N_{b,Kuhn}{}^{\varphi} \tag{5.13a}$$

where

$$\gamma = \frac{\alpha}{3(3\alpha-1)} \quad \text{and} \quad \varphi = \frac{6\beta-\alpha}{3(3\alpha-1)} \tag{5.13b}$$

It should be noted that Eq. 5.13 generally covers different solvent qualities and confinements. In the weak confinement limit ($n \gg N_{b,Kuhn}$), each blob contains a hyperbranched chain segment with $\alpha = 1/2$ and $\beta = 1/10$ in good solvents so that Eq. 5.13 becomes

$$\frac{q_{c,branch}}{q_{c,linear}} = \left(\frac{a}{D}\right)^{\frac{2}{3}} N_{t,Kuhn}{}^{\frac{1}{3}}N_{b,Kuhn}{}^{\frac{1}{15}} \quad \text{or} \quad \left(\frac{a}{D}\right)^{\frac{2}{3}} n_{branch}{}^{\frac{1}{3}}N_{b,Kuhn}{}^{\frac{6}{15}} \quad \text{(weak confinement)} \tag{5.14}$$

where n_{branch} is defined as $N_{t,Kuhn}/N_{b,Kuhn}$, the number of branching points of a hyperbranched chain. In the strong confinement limit ($n \ll N_{b,Kuhn}$), each blob contains a linear chain segment with $\alpha = 3/5$ and $\beta = 0$ in good solvents so that:

$$\frac{q_{c,branch}}{q_{c,linear}} = \left(\frac{N_{t,Kuhn}}{N_{b,Kuhn}}\right)^{\frac{1}{4}} = {n_{branch}}^{\frac{1}{4}} \quad \text{(strong confinement)} \tag{5.15}$$

As expected, for linear chains, $N_{t,Kuhn} = N_{b,Kuhn}$, i.e., $n_{branch} = 1$ so that $q_{c,branch} = q_{c,linear}$. Note that Eq. 5.15 is identical to what de Gennes described after we correct the mistake, i.e., changing the exponent from 4 to 2. However, our recent experimental results showed that the scaling components are different from those predicted in Eqs. 5.14 and 5.15. This is because when a hyperbranched chain is confined and squeezed inside a pore the scaling of its size and the number of Kuhn segments is not 1/2 but much smaller. This is not the point we like to discuss in the next experimental result section. The crossover between two different confinement limits occurs when the pore size reaches a critical value (D^*) at which sizes of the subchain and the pore become similar. Quantitatively, equalizing the right sides of Eqs. 5.14 and 5.15 leads to

$$D^* = a{N_{t,Kuhn}}^{\frac{1}{8}}{N_{b,Kuhn}}^{\frac{19}{40}} \tag{5.16}$$

In this section, by assuming that a polymer chain confined inside a small cylindrical pore is divided into a number of "blobs" whose center of gravity is undergoing the Brownian motions under the thermal agitation, we have shown that it is necessary and sufficient to consider only confinement and hydrodynamic forces on a single blob. A direct balance between them leads to the critical (minimum) flow rate (q_c) to pull a chain through the pore without any priori consideration of chain topology. Using such a simple approach, we have established a unified description of q_c, normalized by $q_{c,linear}$, as $q_c/q_{c,linear} = (D/\xi)^2$ for different chain topologies. The only thing left here is to deduce ξ for each given chain topology. Figure 5.8 schematically summarizes our results for polymer chains with different topologies.

5.2.2 *Experimental Result*

After theoretically illuminating how polymer chains with different topologies pass through a nanopore, we further made use of our fractionated two sets of narrowly distributed hyperbranched polystyrenes to experimentally study how they are pulled through a pore by using a previously established ultrafiltration method.

First, we measured the flow rate dependent relative retention $[(C_0 - C)/C_0]$ of hyperbranched polystyrene fractions by gradually increasing the flow rate. Figure 5.9 shows that $(C_0 - C)/C_0$ decreases as the flow rate increases but not as sharp as the first-order coil-to-stretch transition of linear chains observed before [38, 43]. Presumably, this is because even for a given overall molar

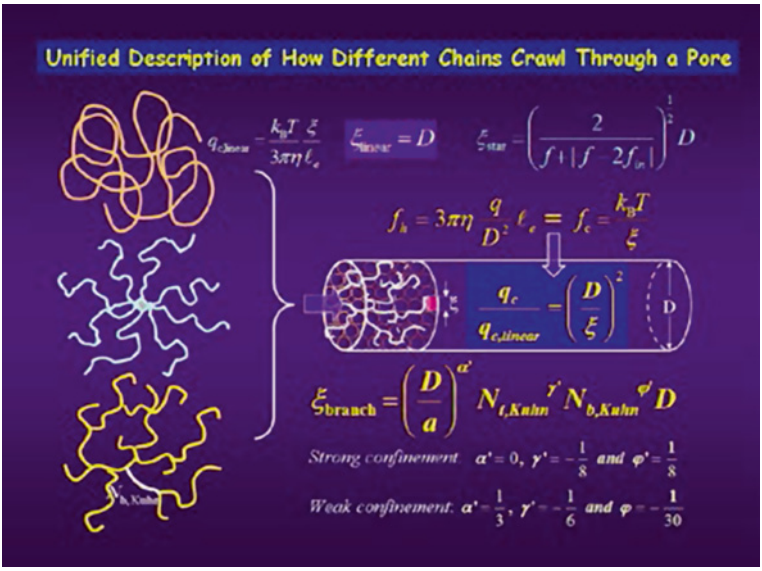

Fig. 5.8 Schematic of a polymer chain with different topologies confined inside a cylindrical pore and how blob size (ξ) varies with chain topology

mass, different arrangements of a given number of uniform subchains can lead to different hyperbranched chain structures. As expected, the flow rate required to pull the hyperbranched chains to pass through the pore increases with N_t for each given N_b.

Figure 5.10 shows that the critical flow rate ($q_{c,b,50\ \%}$) of the hyperbranched chains with a given subchain length is scaled to the polymerization degree of entire hyperbranched chain (N_t) as $q_{c,b,50\ \%} \sim N_t^{\gamma}$ with $\gamma = 1.0 \pm 0.1$. We also differentiated each curve in Fig. 5.9 and plotted $q_{c,b,peak}$, $q_{c,b,20\ \%}$ or $q_{c,b,80\ \%}$ against N_t. The scaling exponent (γ) remains 1.0 ± 0.1. For a given N_t, $q_{c,b,50\ \%}$ decreases as the subchain length increases because longer subchains deform easier inside the pore so that a low flow rate is required to pull each hyperbranched chain through. Further, we fixed N_t to find how $q_{c,b,50\ \%}$ is scaled to N_b. Our results showed that $\varphi = -0.4 \pm 0.1$ with a large uncertainty because there are only three data points within a limited range of N_b. Even considering our experimental uncertainties, our measured scalings are still deviated much from $q_{c,b} \sim N_t^{1/3} N_b^{1/15}$ and $q_{c,b} \sim N_t^{1/4} N_b^{-1/4}$, respectively, predicted for the weak and strong confinements [40], which forces us to reconsider whether something was missing or improper in the original assumption and theoretical treatments of how hyperbranched chains pass through a small cylindrical pore under an elongation flow. It is worth-noting that such theoretical predictions have never been experimentally tested or confirmed before.

As we know, each hyperbranched chain confined inside a small cylindrical pore can be viewed as a number of packed "blobs" and each blob has a size (correlation length) of ξ and contains n number of Kuhn segments, as schematically shown

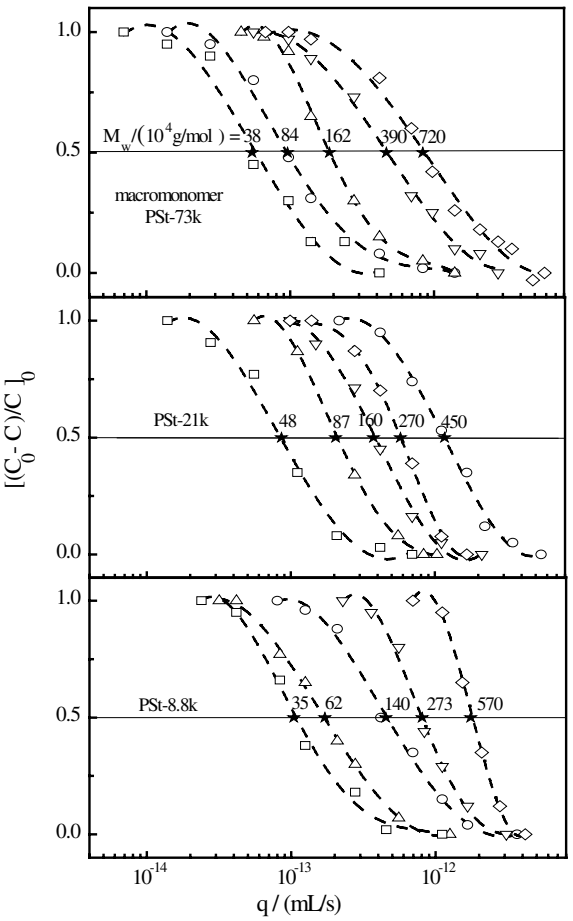

Fig. 5.9 Flow rate (q) dependence of relative retention $[(C_0 - C)/C_0]$ of hyperbranched polystyrene chains made of macromonomers in toluene at T = 25 °C, where symbol *asterisk* marks $q_{c,b,50\,\%}$

in Fig. 5.11. In the limit of the weak or strong confinements, each blob contains a hyperbranched or a linear chain segment, i.e., $\xi = aN_{t,Kuhm}{}^{1/2}N_{b,Kuhm}{}^{1/10}$ or $aN_{t,Kuhm}{}^{3/5}$ in good solvents, where a is the size of a Kuhn monomer; and $N_{t,Kuhm}$ and $N_{b,Kuhm}$ are numbers of the Kuhn segments of the entire hyperbranched chain and the subchain, respectively. Obviously, the maximum size of a blob is the pore diameter (D); namely, $\xi \leq D$. In the previous section, we showed that instead of considering the entire confined chain, one only needs to balance the confinement and hydrodynamic forces on each blob and found a unified description of q_c for chains with different topologies, i.e., $q_c/q_{c,linear} = (D/\xi)^2$ [44].

Here the only thing left is to find ξ for each chain topology. Obviously, for a confined linear chain, $\xi = D$; while for a confined star chain with a total of f arms and a number of forwarded arms inside the pore (f_{in}), we showed how $q_{c,star}$ depends on f and f_{in} in the previous section. As for hyperbranched chains, Eqs. 5.13–5.16 show that:

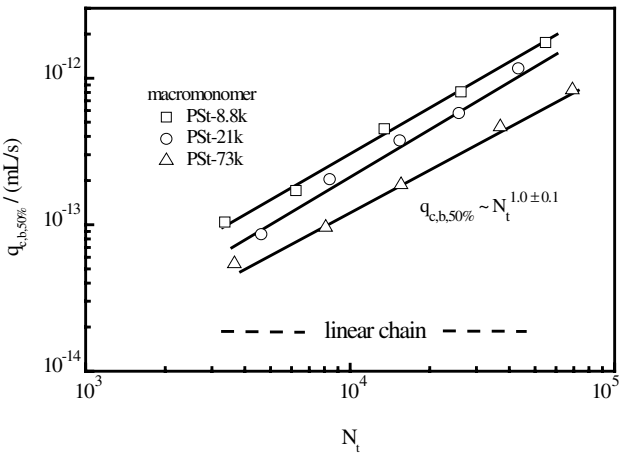

Fig. 5.10 Overall polymerization degree (N_t) dependence of critical flow rate ($q_{c,b,50\ \%}$) of hyperbranched chains made of different seesaw-type macromonomers (i.e., subchain lengths) in toluene at $T = 25$ °C

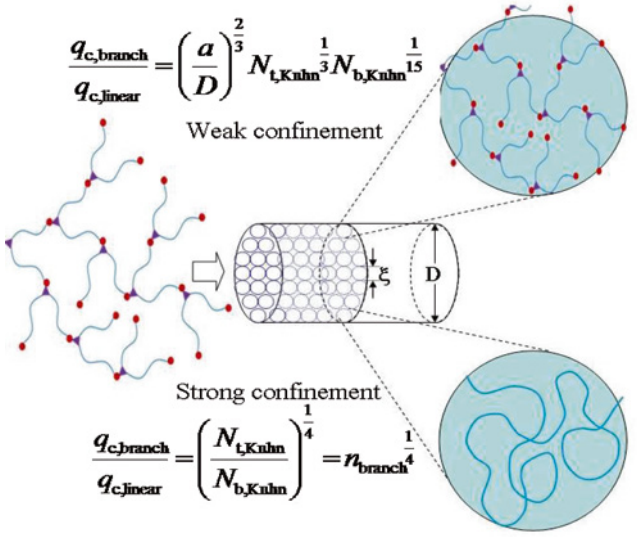

Fig. 5.11 Schematic of weak and strong confinements of a hyperbranched chain inside a small cylindrical pore with a diameter of D, where *each small circle* represents a blob with a size of ξ

$$\frac{q_{c,branch}}{q_{c,linear}} = \left(\frac{a}{D}\right)^{\frac{2(3-5\alpha)}{3(3\alpha-1)}} N_{t,Kuhn}{}^{\gamma} N_{b,Kuhn}{}^{\varphi} \text{ with } \gamma = \frac{\alpha}{3(3\alpha-1)} \text{ and } \varphi = \frac{6\beta-\alpha}{3(3\alpha-1)} \tag{5.13}$$

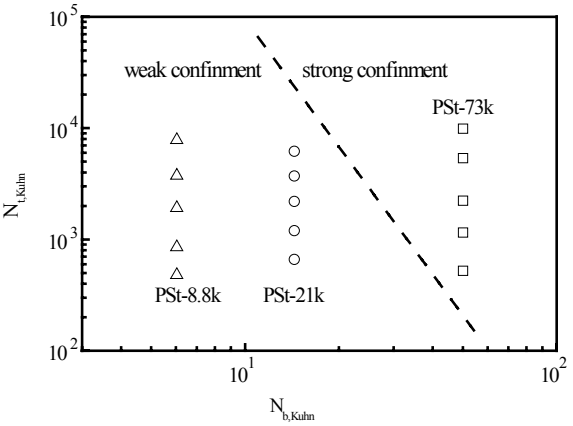

Fig. 5.12 Calculated "phase" diagram of strong and weak confinements of hyperbranched polystyrene chains in toluene at T = 25 °C, where *dash line* represents a boundary between two different confinements, where we used $D^* = 20$ nm, $a \simeq 1.8$ nm, and $N_{b,kuhn} \simeq 7N_b$

$$\frac{q_{c,branch}}{q_{c,linear}} = \left(\frac{a}{D}\right)^{\frac{2}{3}} N_{t,Kuhn}{}^{\frac{1}{3}} N_{b,Kuhn}{}^{\frac{1}{15}} = \left(\frac{a}{D}\right)^{\frac{2}{3}} n_{branch}{}^{\frac{1}{3}} N_{b,Kuhn}{}^{\frac{6}{15}} \quad \text{(weak confinement)} \tag{5.14}$$

$$\frac{q_{c,branch}}{q_{c,linear}} = \left(\frac{N_{t,Kuhn}}{N_{b,Kuhn}}\right)^{\frac{1}{4}} = n_{branch}{}^{\frac{1}{4}} \quad \text{(strong confinement)} \tag{5.15}$$

$$D^* = aN_{t,Kuhn}{}^{\frac{1}{8}} N_{b,Kuhn}{}^{\frac{19}{40}} \tag{5.16}$$

It shows that D^* weakly depends on the overall molar mass but more on the subchain length. For polystyrene in toluene, it is known that each Kuhn segment contains ~7 monomers and has a size of ~1.8 nm [1]. If ξ reaches D (its maximum value, 20 nm), each blob only contains ~55 and ~100 Kuhn segments in the strong and weak confinements, respectively. For the three hyperbranched polystyrenes used here, their subchains respectively contain ~5, ~15 and ~50 Kuhn segments. Therefore, even for the hyperbranched polystyrene made of the shortest subchain, each blob mostly contains ~20 subchains, i.e., ~10 branching points. In reality, ξ is much smaller than D so that each blob contains few branch points. In other words, the chain topology inside each blob is not ideally branched but star-like. As for the hyperbranched polystyrene sample made of the longest subchain, each subchain might contain few blobs.

Quantitatively, letting D^* to be the pore size (20 nm), we are able to estimate the boundary that divides the two confinements, as shown in Figs. 5.11 and 5.12. It is clear that for the hyperbranched polystyrene chains made of the two short macromonomers (PSt-8.8k and PSt-21k), the ultrafiltration occurs in the weak confinement region; while the hyperbranched polystyrenes made of the longest macromonomer (PSt-73k) is on the strong confinement side, but far away from the weak or strong confinement limit, because the pore and subchain have a similar size. In other words, most of our ultrafiltration experiments were done around

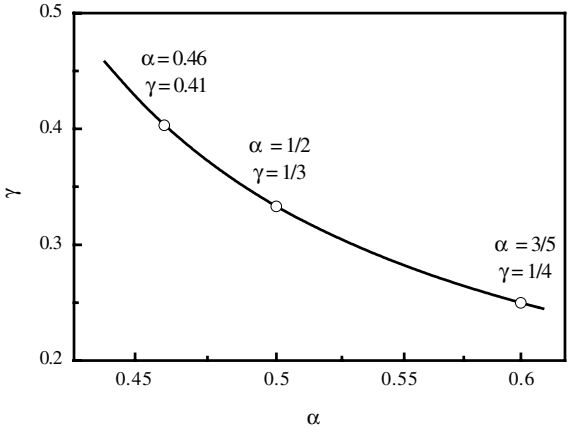

Fig. 5.13 Plot of two scaling exponents α versus γ based on Eq. 5.13

the weak and strong confinement boundary. Therefore, we are not able to use Eqs. 5.14 and 5.15 to treat our experimental data, which also partially explains why the scaling exponents are deviated from the predicted ones.

On the basis of Eq. 5.13, we know that γ increases from 1/4 to 1/3 when α decreases from 3/5 to 1/2, as show in Fig. 5.13. Putting $\alpha = 0.46 \pm 0.01$ into Eq. 5.13, we have $\gamma = 0.41$, still far away from 1.0 ± 0.1, as shown in Fig. 5.13, even after considering all the experimental uncertainties. Physically, for a given overall molar mass, a smaller α means a more compact and less deformable chain conformation so that a higher flow rate is required to drag the chain into the pore, resulting in a stronger molar-mass dependent critical flow rate. Therefore, the higher measured γ value actually means that the real α value should be smaller. Putting the measured γ value into Eq. 5.13, we are able to estimate that $\alpha \simeq 3/8$, which is reasonable because the chain segments inside each blob are squeezed together with a more uniform chain density so that α should be lower than that for the hyperbranched chain free in solutions. In the fully collapsed limit, $\alpha = 1/3$ for a subject with a uniform density. It is worth-noting that such a discrepancy might also be traced back to the assumption of the blob as a non-draining sphere.

On the other hand, φ depends on both α and β. As α decreases from 3/5 to 1/2 and β increases from 0 to 1/10, φ increases from $-1/4$ to 1/15. Equation 5.13 generally shows that a smaller α should lead to a larger φ. In the current study, the chain topology inside the blob changes from branching to star-like and then to linear as the subchain length increases. Therefore, it is not meaningful to extract φ from our current study. In reality, using shorter initial sub-chains in the polymerization results in smaller hyperbranched chains; while using much longer initial subchains leads to a low reactivity, which limit the reachable ranges of $N_{\mathrm{t,Kuhn}}$ and $N_{\mathrm{b,Kuhn}}$.

Figure 5.14 further shows how the pore size (D) affect $q_{\mathrm{c,branch}}$. The slope of $q_{\mathrm{c,branch}}$ versus D is slightly smaller than $-2/3$ predicted by Eqs. 5.14 and 5.15. Since there are only two points, we should not be too serious about the exact

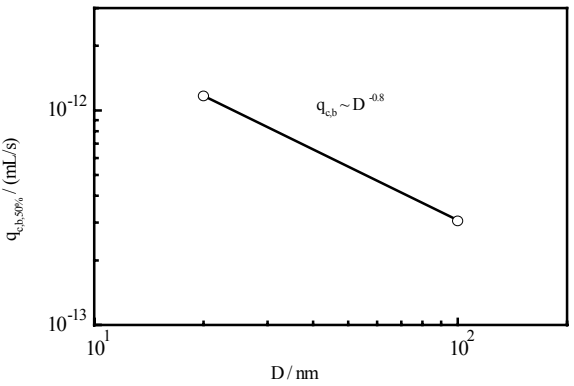

Fig. 5.14 Pore size (D) dependence of critical flow rate ($q_{c,branch,50\ \%}$) of fraction made of macromonomer PSt-21k with $N_t = 4.33 \times 10^4$

value of the slope. Besides the experimental uncertainties, such a deviation can be similarly explained as what we did for linear chains [31, 38, 43]. Namely, each blob contains a chain segment, not a hard sphere, so that it is draining. Therefore, the effective length of each blob (l_e) along the flow direction is longer than its size (ξ) and l_e is proportional to the molar mass of the chain segment inside the blob and scaled to ξ with a scaling exponent that depends on the topology of the chain segment inside the blob.

Up to now, we have discussed how the molar masses of the overall chain and the subchain affect the ultrafiltration of a hyperbranched chain through a small cylindrical pore. Note that our ultimate goal of conducting this kind of studies is to use what we found/understood to separate polymer chains by their structures, such as the subchain length and the overall molar mass, instead of those existing methods mainly by the hydrodynamic volume and solubility. Using the following example, we like to demonstrate how it works in a real application to effectively separate hyperbranched chains with a similar size but different subchain lengths.

To demonstrate it, we purposely chose two hyperbranched samples and their molecular parameters [the weight-average molar mass (M_w), polydispersity index (M_w/M_n), and average hydrodynamic radius ($\langle R_h \rangle$)], are summarized in Table 5.1, where a linear polystyrene sample was used as an internal reference to calibrate the concentrations of hyperbranched chains before and after the ultrafiltration.

Figure 5.15 shows that when the flow rate is 4.0×10^{-11} mL/s, much higher than $q_{c,HB\text{-}3.3k}$ and $q_{c,HB\text{-}73k}$, both of the two hyperbranched chains are able to pass through small pores because we know the ratio of the peak areas between the two hyperbranched and short linear reference chains. As the flow rate decreases to 4.0×10^{-12} mL/s, higher than $q_{c,HB\text{-}73k}$ (1.0×10^{-13} mL/s) but still much lower than $q_{c,HB\text{-}3.3k}$, we also observed two peaks, as shown in Fig. 5.15b, in which the area of the peak located at ~25 nm decreases by ~50 %. In comparison with the solution mixture before the ultrafiltration and data in Table 5.1, we know, in principle, that here smaller HB-3.3k chains with a short subchain length and a higher branching degree are retained by small cylindrical pores because it

Table 5.1 Molecular parameters of two hyperbranched and one short linear chains

Polymer	$M_{w,macromonomer}$/(kg/mol)	M_w/(kg/mol)	M_w/M_n	$\langle R_h \rangle$/nm
HB-3.3k	3.3	780	1.13	21
HB-73k	73	840	1.10	27
Linear PS as an internal reference		11	1.05	2.6

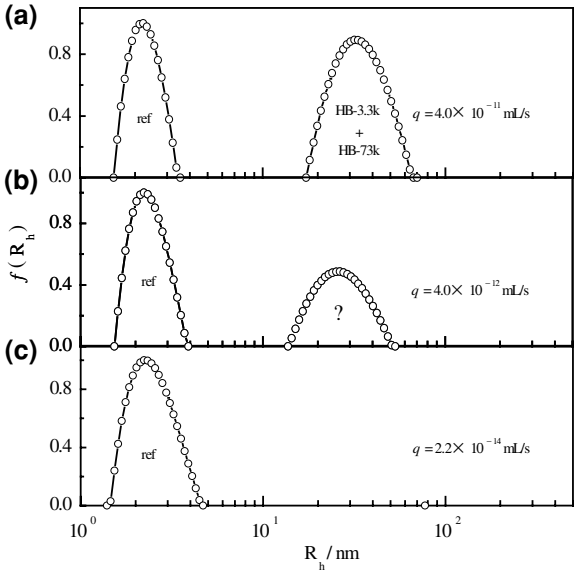

Fig. 5.15 Hydrodynamic radius distribution of a solution mixture of linear reference and two hyperbranched chains (HB-3.3k, and HB-73k) in toluene at T = 25 °C after they are extruded through small cylindrical pores (20 nm) under different flow rates, where $C_{ref} = 40$ mg/mL, $C_{HB\text{-}3.3k} = 0.6$ mg/mL and $C_{HB\text{-}73k} = 0.5$ mg/mL

is relatively difficult to deform a hyperbranched chain with a shorter subchain (a higher branching degree) when two hyperbranched chains have a similar overall molar mass. As expected, Fig. 5.15c shows that further decrease of the flow rate to 2.2×10^{-14} mL/s makes the peak on the right disappearing because both the hyperbranched chains are retained by small pores.

For an attentive reader, there still remains a question whether the peak on the right in Fig. 5.15 is truly related to smaller hyperbranched HB-3.3k, instead of larger HB-73k chains that pass though small cylindrical pores. To clarify this point, we mixed the linear reference chains with HB-3.3k and HB-73k, respectively, to prepare two solution mixtures. As shown in Fig. 5.16a, larger hyperbranched HB-73k chains pass through when the flow rate reaches to 4.0×10^{-12} mL/s, while smaller hyperbranched HB-3.3k chains are still retained, i.e., its related peak is missing in Fig. 5.16b in comparison with Fig. 5.16c. It requires a flow rate 10 times higher to push smaller hyperbranched HB-3.3k chains to pass through small cylindrical pores (Fig. 5.16c), clearly answering the question. It experimentally demonstrates that one can use small pores to separate hyperbranched chains by their structures instead of their sizes.

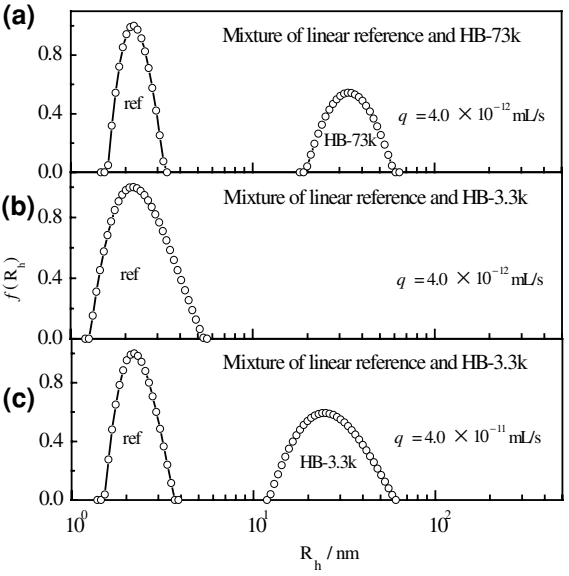

Fig. 5.16 Hydrodynamic radius distributions of mixtures of linear reference respectively with hyperbranched HB-3.3k and HB-73k chains in toluene at T = 25 °C after they are extruded through small cylindrical pores (20 nm) under different flow rates, where $C_{ref} = 40$ mg/mL, $C_{HB\text{-}73k} = 0.6$ mg/mL, and $C_{HB\text{-}3.3k} = 0.8$ mg/mL

5.3 Solution Properties of Amphiphilic Hyperbranched Copolymer Chains in Dilute and Semidilute Solutions

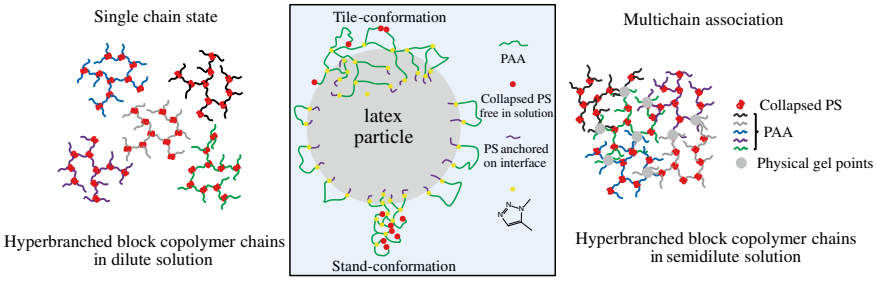

5.3.1 Solution Properties of Hyperbranched Block Copolymer Hyper-(PtBA-PS-PtBA)$_n$ and Hyper-(PAA-PS-PAA)$_n$

Previously, we successfully prepared narrowly distributed amphiphilic hyperbranched block copolymer hyper-(P*t*BA$_{36}$-PS$_{55}$-P*t*BA$_{36}$)$_{600}$. In this section, we'll see how these ultralarge hyper-(P*t*BA$_{36}$-PS$_{55}$-P*t*BA$_{36}$)$_{600}$ chains fold and associate

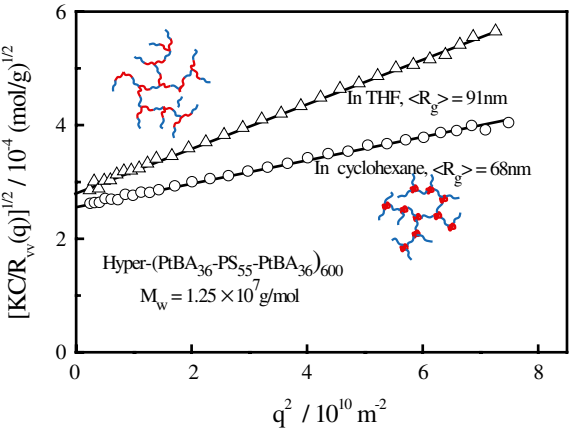

Fig. 5.17 Angular dependence of $[KC/R_{vv}(q)]^{1/2}$ (the Berry plot) of hyper-(P*t*BA$_{36}$-PS$_{55}$-P*t*BA$_{36}$)$_{600}$ in THF, good for both P*t*BA and PS blocks; and in cyclohexane, only selectively good from P*t*BA block

in a good solvent (THF) and a selective poor solvent (cyclohexane) of the PS block by LLS measurements. For comparison, we also studied a hyperbranched PS homopolymer, hyper-(PS$_{700}$)$_{120}$. Figure 5.17 shows that the Berry plot is better than the Zimm plot in extracting M_w and $\langle R_g \rangle$ of the hyper-(P*t*BA$_{36}$-PS$_{55}$-P*t*BA$_{36}$)$_{600}$ chains in THF and cyclohexane, where the concentration correction was ignored because the solution was so dilute ($C \sim 10^{-5}$ g/mL). The decrease of $\langle R_g \rangle$ clearly shows the contraction of hyper-(P*t*BA$_{36}$-PS$_{55}$-P*t*BA$_{36}$)$_{600}$ chains in cyclohexane. On the other hand, the extrapolation to the zero scattering angle ($q \to 0$) leads to a similar intercept, indicating that no interchain association occurs in cyclohexane. The smaller size in cyclohexane reflects that for polystyrene the solvent quality of THF is much better than cyclohexane at 25 °C.

Figure 5.18 shows that $\langle R_h \rangle$ decreases from 76.0 to 57.5 nm, presumably directly revealing the intrachain contraction of individual PS blocks in cyclohexane as the solution is cooled down. Both $\langle R_g \rangle$ and $\langle R_h \rangle$ of the hyperbranched chains in cyclohexane are smaller than that in THF because of the shrinking of the PS blocks in cyclohexane. It is interesting to note that the ratios of $\langle R_g \rangle / \langle R_h \rangle$ in two solvents nearly remain a constant value of ~1.2, a typical value for hyperbranched chains, revealing that hyperbranched chains have a very similar chain conformation in these two solvents even the PS blocks slightly shrink in cyclohexane.

Figure 5.19 shows that lowering the solution temperature from 60 to 10 °C has nearly no effect on M_w of hyperbranched copolymer chains but leads to a very sharp increase of M_w of hyperbranched homopolymer chains at ~28 °C, signaling the interchain association, which is expected because unlike the copolymer chains there is no soluble P*t*BA blocks to stabilize those collapsed PS subchains and prevent them to phase out of the solution. Such intrachain contraction and interchain association are also directly reflected in the decrease of both $\langle R_g \rangle$ and $\langle R_h \rangle$. It is also understandable that the hyperbranched homopolymer chains shrink much

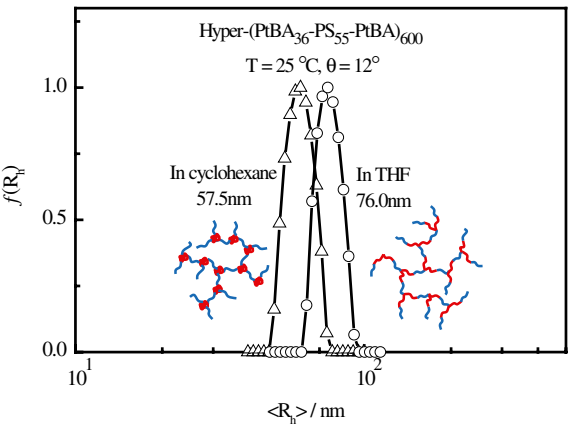

Fig. 5.18 Hydrodynamic radius distributions of hyperbranched hyper-($PtBA_{36}$-PS_{55}-$PtBA_{36}$)$_{600}$ in THF, good for both P*t*BA and PS blocks, and in cyclohexane, only selectively good from P*t*BA block

more that their copolymer counterparts. It should be stated that the time-average scattering intensity of the copolymer solution after the extrapolation to the zero scattering angle remains a constant in the temperature range 10–60 °C, also indicating that no interchain association occurred at ~10 °C, at which cyclohexane is a very poor solvent for PS.

Figure 5.19c shows that for the hyperbranched homopolymer chains, $\langle R_g \rangle / \langle R_h \rangle$ decreases as the temperature decreases before the chains start to associate because $\langle R_g \rangle$ decreases faster than $\langle R_h \rangle$. Note that $\langle R_g \rangle$ describes how mass is distributed in space, while $\langle R_h \rangle$ contains the hydrodynamic draining. Such a size decrease as the chain shrinks was also observed for linear homopolymer chains before because of a less change in $\langle R_h \rangle$ [45, 46], especially in the low temperature region. However, an opposite trend was observed for the hyperbranched copolymer chains, presumably because the shrinking of each PS block makes the subchain less flexible, which has an opposite effect on $\langle R_g \rangle$.

It should be noted that the formation of a single-flower conformation here is unlikely because each collapsed PS block is hindered by three soluble P*t*BA blocks that are linked to other triblock subchains. The occurrence of intrachain contraction with no interchain association in a very dilute solution is mainly attributed to the existence of those soluble P*t*BA blocks on its periphery.

Furthermore, we used LLS to study interchain association of hyperbranched block copolymer hyper-(PAA_{23}-PS_{14}-PAA_{23})$_n$ chains in aqueous solutions. We first determined their differential refractive index increments (d*n*/d*C*) of hyper-(PAA_{23}-PS_{14}-PAA_{23})$_n$ in 0.1 M and 1.0 M NaCl aqueous solution, which are 0.17 and 0.19 mL/g, respectively. The addition of NaCl is to suppress the polyelectrolytes effect. It should be stated that for all the solutions, pH ~ 9.0. This is because the AA group used was in the sodium salt form (–COONa) and most of the –COONa groups (~95 %) are ionized into $–COO^-$ and Na^+ in water according to literature [47, 48].

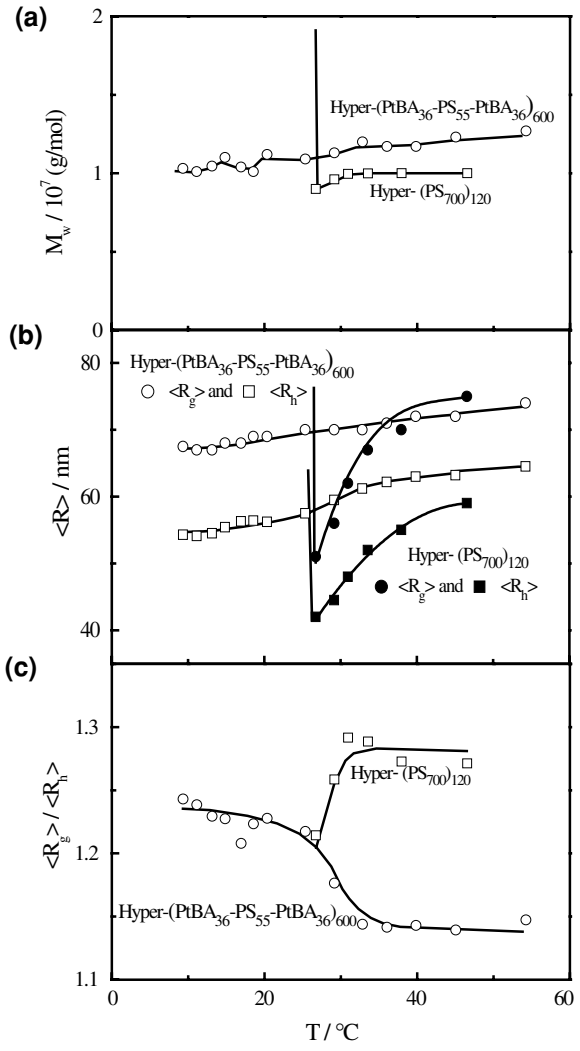

Fig. 5.19 Temperature dependence of **a** weight average molar mass (M_w), **b** average radius of gyration ($\langle R_g \rangle$) and average hydrodynamic radius ($\langle R_h \rangle$), and **c** $\langle R_g \rangle / \langle R_h \rangle$ of hyper-(P*t*BA$_{36}$-PS$_{55}$-P*t*BA$_{36}$)$_{600}$ copolymer and hyper-(PS$_{700}$)$_{120}$ homopolymer in cyclohexane, a solvent selectively poor for PS blocks at temperatures lower than ~34.5 °C

Figure 5.20 shows that larger hyperbranched block copolymer chains have a less tendency to undergo interchain association and the average aggregation number (N_{agg}) is related to the weight average degree of polycondensation ($(DP)_w$) as $N_{agg} \sim (DP)_w^{-0.7}$. Presumably, in a large hyper-(PAA$_{23}$-PS$_{14}$-PAA$_{23}$)$_n$ chain, most of its hydrophobic PS blocks are inevitably wrapped, protected and stabilized by those hydrophilic PAA blocks at its periphery so that the interchain association is hindered, resulting in a smaller N_{agg}.

Figure 5.21 reveals that adding salt promotes the interchain association of hyperbranched chains in spite of their different initial sizes, but for a given salt

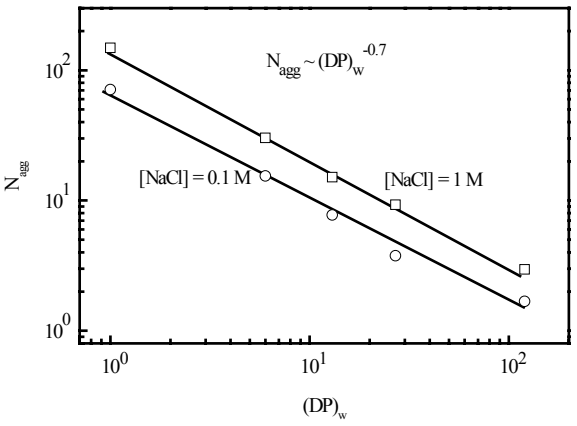

Fig. 5.20 Degree of polycondensation $(DP)_w$ dependence of average aggregation number (N_{agg}) of hyper-$(PAA_{23}\text{-}PS_{14}\text{-}PAA_{23})_n$ chains in different aqueous solutions, where $C_{copolymer} = 1.0$ g/L

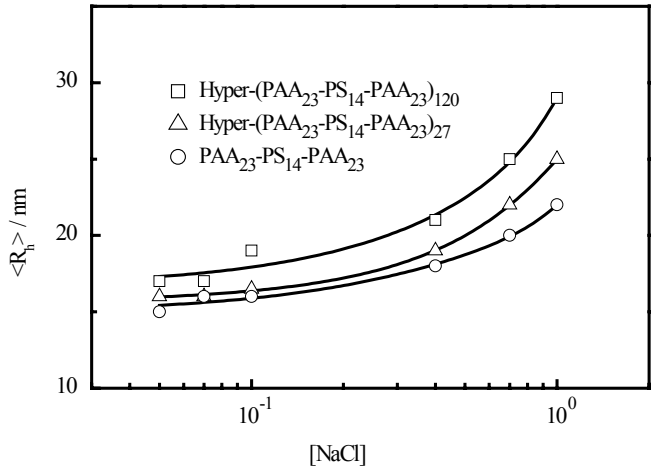

Fig. 5.21 Salt concentration dependence of average hydrodynamic radius ($\langle R_h \rangle$) of hyper-$(PAA_{23}\text{-}PS_{14}\text{-}PAA_{23})_n$ and their corresponding linear triblock precursor $PAA_{23}\text{-}PS_{14}\text{-}PAA_{23}$

concentration, the increment of the average hydrodynamic size of the resultant aggregates increases with its initial size, i.e. $(DP)_w$, which is expected. It should be noted that the addition of salt into the solution makes the PAA block contract and reduces its stabilization role. The intrachain contraction and interchain association have opposite effects on $\langle R_h \rangle$. The results in Fig. 5.21 indicate that the interchain association overrides the intrachain contraction of the PAA blocks.

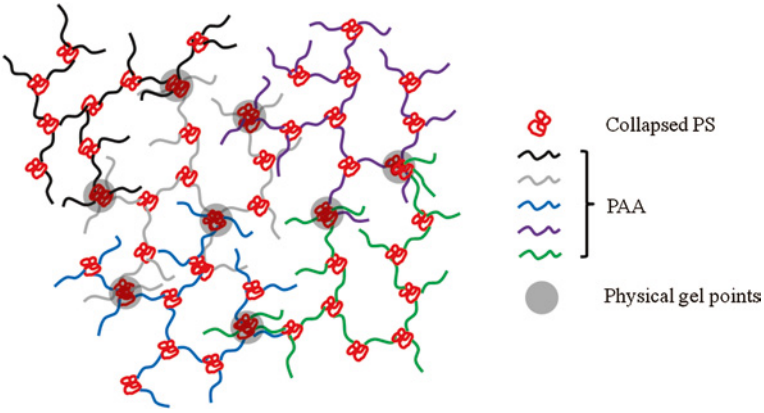

Fig. 5.22 Schematic of how hyper-$(PAA_{23}\text{-}PS_{14}\text{-}PAA_{23})_n$ chains undergo interchain association to form a gel-like network, where PAA blocks from different chains are represented by *different colors*

It is worth-noting that in the high salt range 0.1–1.0 M, linear triblock precursor can only form more compacted micelle-like aggregates via the hydrophobic association of those collapsed PS blocks. In contrast, the interchain association of those collapsed PS blocks among different hyperbranched chains is more difficult because most of them are entrapped inside and surrounded by soluble hydrophilic PAA blocks. Therefore, the interchain association of hyperbranched chains only occurs via those collapsed PS blocks near their periphery, resulting in a loosely connected microgel-like structure with a larger $\langle R_h \rangle$, as shown in Fig. 5.21. As expected, if the hyperbranched copolymer concentration is higher than the overlapping concentration (C^*), i.e., in the semi-dilute regime, the interchain association of those collapsed PS blocks will act as physical cross-linking points to form a gel-like structure (Fig. 5.22) that can be better examined by rheological measurements.

Figure 5.23a shows that the storage modulus (G') of hyper-$(PAA_{23}\text{-}PS_{14}\text{-}PAA_{23})_6$ chains in aqueous solution gradually increases with its concentration (C) and finally exceeds its loss modulus (G'') at $C \sim 50$ g/L, revealing a gel-like behavior. Further increase of C to 60 g/L led to a free-standing gel. Figure 5.23b shows a strain-hardening feature, typical for solutions containing associative polymers; namely, G' increases with strain after an initial flat regime but before the shear thinning occurs at higher strains. As expected, no gel-like behavior was observed for triblock PAA-PS-PAA precursor even when C reached 200 g/L.

Figure 5.24 shows that for a given copolymer concentration, both G' and G'' increase with $(DP)_w$. Theoretically, for a space (V) containing N uniform hard spheres with a radius of R without any specific interaction, their volume fraction (ϕ_{sphere}) can be expressed as $\phi_{sphere} = (4\pi R^3/3)N/V = C/C^*$. Assuming each

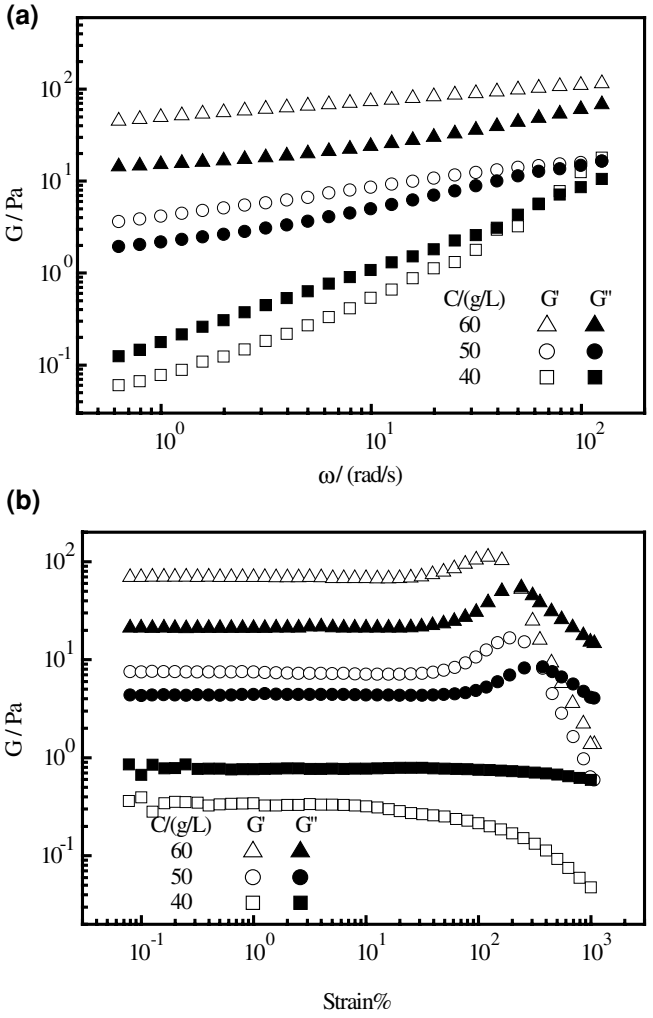

Fig. 5.23 **a** Oscillatory frequency and **b** strain dependence of hyper-$(PAA_{23}\text{-}PS_{14}\text{-}PAA_{23})_6$ aqueous solutions with different copolymer concentrations

hyperbranched chain as a sphere and using the scaling law $R_g \sim M_w^{1/2}$ for ideal hyperbranched chains, we have

$$C^* = \frac{M_W}{\left(4\pi R_g^3/3\right)N_A} \sim M_W^{-1/2} \tag{5.17}$$

Therefore, for a given weight/volume concentration (C), larger hyper-$(PAA_{23}\text{-}PS_{14}\text{-}PAA_{23})_n$ chains have a higher volume fraction, leading to a higher modulus.

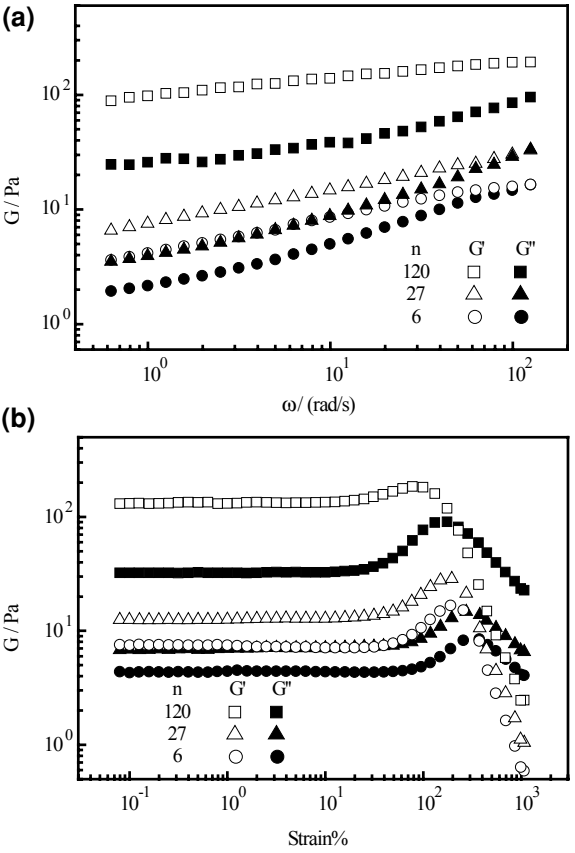

Fig. 5.24 **a** Oscillatory frequency and **b** strain dependence of hyper-(PAA_{23}-PS_{14}-PAA_{23})$_n$ aqueous solutions with different degrees of polycondensation $(DP)_w$, where $C = 50$ g/L

However, a quantitative description between the volume fraction and the modulus is rather difficult because of several reasons: (1) we need the pre-factor in the scaling law $R_g \sim M_w^{1/2}$; (2) each hyperbranched chain is not a hard sphere; and (3) the modulus of our gel-like system is related to both the interchain hydrophobic interaction among those collapsed PS blocks and the interchain entanglements among the swollen PAA blocks on periphery.

5.3.2 Solution Properties of Hyperbranched Graft Copolymer HB-(PAA_{78})$_n$-g-(PS_{10})$_{n+1}$

Using LLS technique, we also studied the solution properties of amphiphilic hyperbranched graft copolymer HB-(PAA_{78})$_n$-*g*-(PS_{10})$_{n+1}$. It is worth noting that triblock PS-PAA-PS is actually a special case of HB-(PAA)$_n$-*g*-(PS)$_{n+1}$, i.e., all of

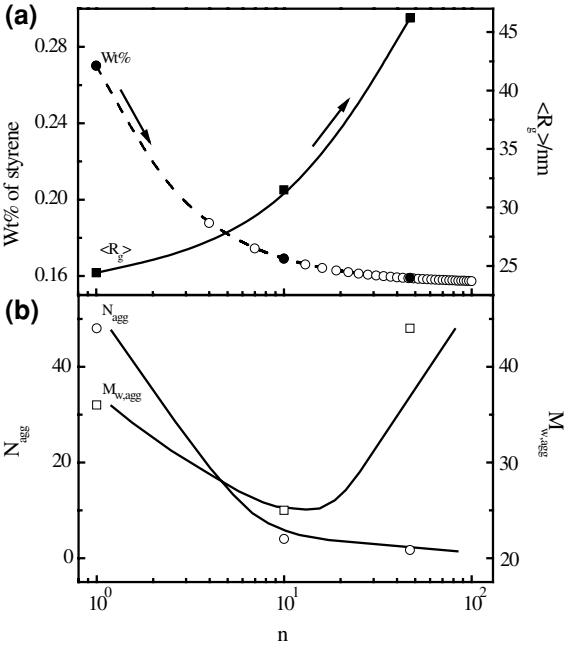

Fig. 5.25 Polycondensation degree (n) dependence of **a** styrene weight fraction (wt%) and average radius of gyration ($\langle R_g \rangle$) and **b** aggregation number (N_{agg}) and weight-average molar mass ($M_{w,agg}$) of HB-(PAA)$_n$-*g*-(PS)$_{n+1}$ chains in a 40 mM Na_2CO_3 aqueous solution, where the polymer concentration is 2.0 g/L

PS-PAA-PS, HB-(PAA)$_{10}$-*g*-(PS)$_{11}$ and HB-(PAA)$_{47}$-*g*-(PS)$_{48}$ are among a family of HB-(PAA)$_n$-*g*-(PS)$_{n+1}$, where $n = 1$, 10 and 47, respectively.

Figure 5.25 shows how the theoretical styrene weight fraction (wt%) depends on n. As shown, wt% decreases from 0.27 to 0.16 as n increases from 1 to 47; in other words, triblock PS-PAA-PS has the highest styrene weight fraction, which is reasonable because for an individual PS-P*t*BA-PS chain, each P*t*BA chain can couple with 2 PS chains; while for an individual HB-(PAA)$_n$-*g*-(PS)$_{n+1}$ chain, each P*t*BA chain, on average, can at most couple with only 1 PS chain in the limit of $n \to \infty$. In the following study of interchain association of HB-(PAA)$_n$-*g*-(PS)$_{n+1}$ chains in dilute aqueous solution, the addition of Na_2CO_3 can suppress the polyelectrolytes effect and adjust the solution pH to be constant. It should be stated that for all the solutions the AA group is assumed to be in the sodium salt form (–COONa), and most of the –COONa groups (~95 %) are ionized into $–COO^-$ and Na^+ in water (pH = 9.0–10) according to literatures [47, 48]. As shown in Fig. 5.25a, the average radii of gyration ($\langle R_g \rangle$) of the aggregates made of HB-(PAA)$_n$-*g*-(PS)$_{n+1}$ chains increase from 24.2 to 46.3 nm as n increases; but it is still difficult to answer whether this increment is attributed to a stronger aggregation ability of HB-(PAA)$_{47}$-*g*-(PS)$_{47}$ chains or much larger size of an individual HB-(PAA)$_{47}$-*g*-(PS)$_{48}$ chain, compared with triblock PS-PAA-PS chain. Figure 5.25b shows the calculated aggregation number ($N_{agg} = M_{w,agg}/M_{w,unimer}$) monotonically decreases from ~48 to ~2, strongly indicating larger HB-(PAA)$_n$-*g*-(PS)$_{n+1}$ copolymer chains have a less tendency

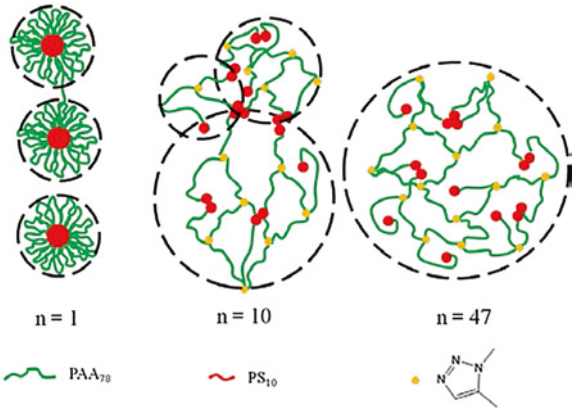

Fig. 5.26 Schematic of interchain association of HB-$(PAA)_n$-*g*-$(PS)_{n+1}$ chains in dilute solution

to undergo interchain association. Presumably, for a large HB-$(PAA)_n$-*g*-$(PS)_{n+1}$ chain in dilute solution, most of its peripheral hydrophobic PS chains collapse, and are easily protected and stabilized by those internal hydrophilic PAA segments, so that the interchain association is hindered due to the steric effect, resulting in a smaller N_{agg} for HB-$(PAA)_n$-*g*-$(PS)_{n+1}$ with a larger n (Fig. 5.25). Therefore, it is actually not strange that the weight-average molar mass ($M_{w,agg}$) of aggregates has a minimal value at $n = 10$ because both of $M_{w,unimer}$ and N_{agg} could affect the final $M_{w,agg}$.

As mentioned before, the hydrophobic PS chain number per amphiphilic chain is limited to 2 for PS-PAA-PS, but $(n + 1)$ for HB-$(PAA)_n$-*g*-$(PS)_{n+1}$. Moreover, the aggregated structure made of HB-$(PAA)_{47}$-*g*-$(PS)_{48}$ chains is assumed to be much more loose than that made of triblock PS-PAA-PS chains. More specifically, the apparent segment density (ρ_{agg}) can be expressed as:

$$\rho_{agg} = 3M_{w,agg} / \left(4\pi N_A \langle R_{g,agg} \rangle^3\right) \tag{5.18}$$

where N_A represents Avogadro constant 6.02×10^{23} mol^{-1}. For aggregates made of PS-PAA-PS, HB-$(PAA)_{10}$-*g*-$(PS)_{11}$ and HB-$(PAA)_{47}$-*g*-$(PS)_{48}$ chains, the calculated ρ_{agg} is 9.4, 4.2 and 2.8 g/L, respectively, implying the decrease of overlap concentration (C) of assembled aggregates with a larger n. Therefore, one can image that HB-$(PAA)_n$-*g*-$(PS)_{n+1}$ with a larger n could form a gel-like structure more easily in semi-diluted solution, where the peripheral collapsed short PS chains from different HB-$(PAA)_n$-*g*-$(PS)_{n+1}$ chains are expected to act as physical cross-linking points (Fig. 5.26).

Figure 5.27 shows that HB-$(PAA)_{47}$-*g*-$(PS)_{48}$ chains can form a free-standing gel at a concentration of 90 g/L, while PS-PAA-PS solution is still a flowing fluid. Based on simple vial-inversion experiments, the apparent critical gel concentration (C_g) of HB-$(PAA)_{47}$-*g*-$(PS)_{48}$ and HB-$(PAA)_{10}$-*g*-$(PS)_{11}$ is respectively ~80 and ~130 g/L; while no gel-formation was observed for PS-PAA-PS even the concentration reached to 200 g/L. More quantitatively, Fig. 5.27b shows the storage modulus (G') of

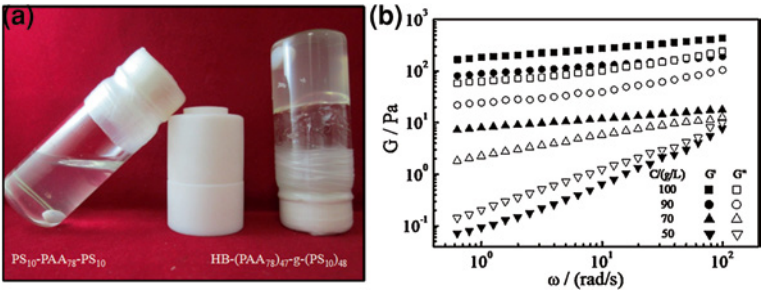

Fig. 5.27 **a** Photograph of 90 g/L aqueous solutions (NaOH/COOH = 1/1) of PS-PAA-PS and HB-$(PAA)_{47}$-*g*-$(PS)_{48}$; and **b** oscillatory frequency dependence of HB-$(PAA)_{47}$-*g*-$(PS)_{48}$ aqueous solution with different polymer concentrations at 25 °C

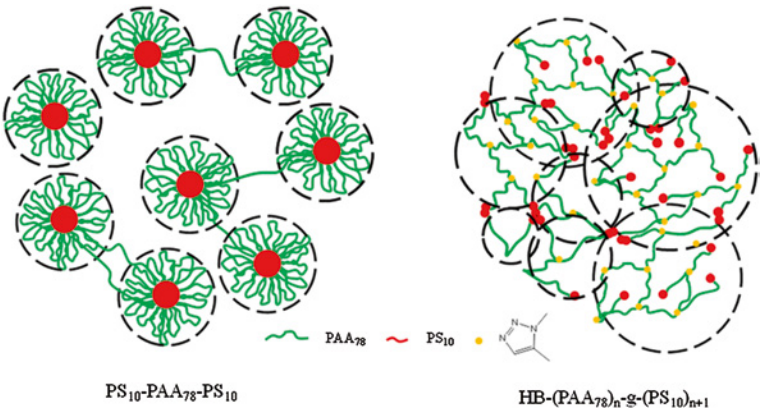

Fig. 5.28 Schematic of interchain association of HB-$(PAA)_n$-*g*-$(PS)_{n+1}$ chains in a semidiluted solution

HB-$(PAA)_{47}$-*g*-$(PS)_{48}$ solution gradually increases with its concentration and finally exceeds its loss modulus (G'') at a concentration of ~70 g/L, implying a sol-gel transition. Figure 5.28 shows the possible gel formation mechanism of HB-$(PAA)_n$-*g*-$(PS)_{n+1}$ chains in concentrated solution.

In aqueous emulsion polymerization, amphiphilic polymers are widely used as polymeric surfactants to stabilize the latex particles, where the hydrophobic blocks can anchor on the particle surface while the hydrophilic blocks extend into the water phase and create a hydrophilic shell [47, 49–52]. Therefore, PS-PAA-PS and HB-$(PAA)_{47}$-*g*-$(PS)_{48}$ copolymers were further used as polymeric surfactants to explore the effect of chain topology on the emulsifying efficiency. The characterization results of solid contents (τ), latex particle sizes ($\langle R \rangle$) and numbers (N_p) are summarized in Table 5.2, Figs. 5.29 and 5.30, where the average particle diameters were carefully determined by DLS at pH ~ 3.2 to ensure the full collapse

Table 5.2 Characterization of the latex particles prepared by using PS-PAA-PS and HB-$(PAA)_{47}$-*g*-$(PS)_{48}$ as emulsifiers

Sample	C/(g/L)	$\langle R_h \rangle$/nm[a]	(τ)/(g/L)	$N_p/(10^{17}L)$	PDI[b]
PS_{10}-PAA_{78}-PS_{10}	0.400	78	92.1	3.03	0.10
	0.800	56	95.3	2.21	0.09
	1.500	46	94.2	1.21	0.11
	3.000	41	93.8	0.45	0.08
HB-$(PAA_{78})_{47}$-*g*-$(PS_{10})_{48}$	0.400	121	95.4	1.45	0.12
	0.800	79	96.3	0.70	0.10
	1.500	68	94.3	0.43	0.10
	3.000	49	92.9	0.14	0.11

[a] All the results were obtained at a scattering angle of 90°, and the relative error for $\langle R_h \rangle$ is ±2 %
[b] Polydispersity index (PDI) was estimated from relative line-width (μ_2) of diffusion coefficient distribution and average diffusion coefficient ($\langle D \rangle$), i.e., $PDI = 1 + 4\mu_2/\langle D \rangle^2$, where $\mu_2 = \int_0^\infty G(D)(D - \langle D \rangle)^2 \, dD$ in DLS, and all the results were obtained at a scattering angle of 90°

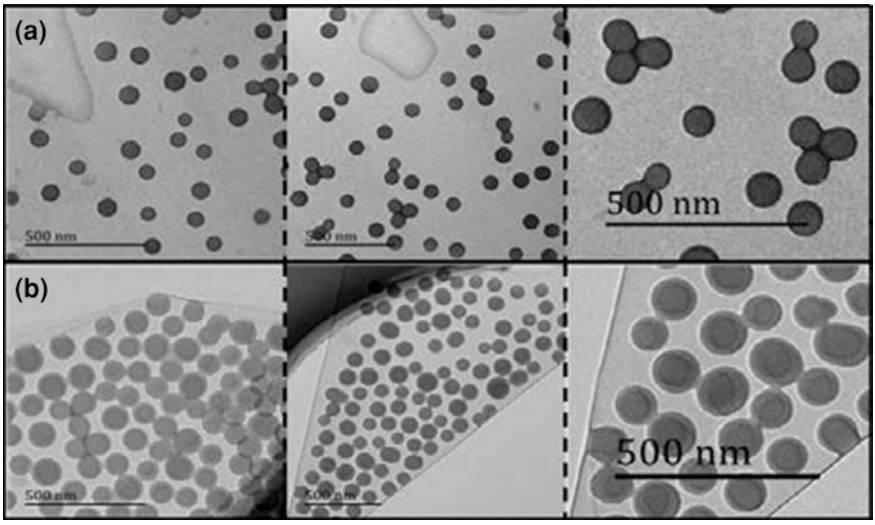

Fig. 5.29 TEM characterization of the latex particles stabilized by **a** PS-PAA-PS and **b** HB-$(PAA)_{47}$-*g*-$(PS)_{48}$, where the $C_{surfactant} = 0.8$ g/L

of PAA-shell. First, TEM characterization (Fig. 5.29) reveals that the latex particles stabilized by both PS-PAA-PS and HB-$(PAA)_{47}$-*g*-$(PS)_{48}$ surfactants are spherical and narrowly dispersed; while the size of the latex particles stabilized by PS-PAA-PS chains are much smaller than that stabilized by HB-$(PAA)_{47}$-*g*-$(PS)_{48}$ for a given concentration, which was further quantitatively verified by DLS measurements (Table 5.2). One classic method for elucidating the effects which

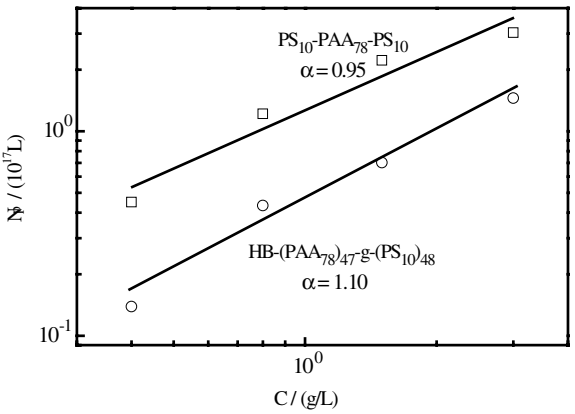

Fig. 5.30 Surfactant concentrations (C) dependence of numbers (N_p) of polystyrene latex particle stabilized by PS-PAA-PS and HB-$(PAA)_{47}$-g-$(PS)_{48}$ chains

a surfactant molecule has on the resultant latex particle size can be found in the exponent value α:

$$N_p \sim C^{\alpha} \tag{5.19}$$

where N_p and C represent the polystyrene latex particle number and surfactant concentration, respectively; exponent α is a variable parameter which correlates to the mobility and nucleation ability of surfactant molecules in the aqueous phase [47]. Experimentally, the values of N_p were calculated according to $N_p = 3\tau/(4\pi\rho\langle R\rangle^3)$, where ρ is 1.05 g/mL for PS latex particles [47]. Moreover, the total surface areas (A_{tot}) of all the latex particles occupied by the surfactant molecules, which is a key parameter to evaluate the surfactant efficiency, can be expressed as:

$$A_{total} = 4\pi\langle R\rangle^2 N_p = 3\tau/(\rho\langle R\rangle) \tag{5.20}$$

Equation 5.20 demonstrates that the surfactant efficiency can be reflected in both of the solid content and particle size. Interestingly, no significant difference among the solid contents was observed between surfactants with different topologies (Table 5.2), which means the efficiency can be simply reflected in $\langle R\rangle$ or N_p.

Figure 5.30 shows the DLS characterization result of how the measured latex number (N_p) depends on surfactant concentration (C). As shown, the calculated exponents α of PS-PAA-PS is slightly smaller than that of HB-$(PAA)_{47}$-g-$(PS)_{48}$, indicating a stronger ability of unimer extraction and diffusion, which is attributed to that diffusion coefficient generally decreases with molar mass. While the observed N_p of PS-PAA-PS is ~2 times larger than that of HB-$(PAA)_{47}$-g-$(PS)_{48}$, disagreeing with what we expected originally because a lager N_p means a larger A_{tot}.

Figure 5.31 shows two possible alignments of a HB-$(PAA)_n$-g-$(PS)_{n+1}$ surfactant molecule on the water/particle interface, i.e., tile- and stand-conformation. In an ideal case, the surface area covered by an individual HB-$(PAA)_n$-g-$(PS)_{n+1}$ chain is the largest when a tile-conformation is adopted, where nearly all the PAA segments and PS grafted chains are on a common plane and the grafted PS chains

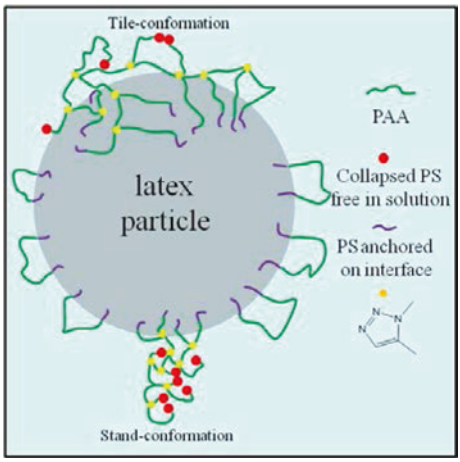

Fig. 5.31 Schematic of two possible alignments of a HB-(PAA)$_n$-*g*-(PS)$_{n+1}$ copolymer chain on the water/particle interface

can insert into the particle/water interface; while such a conformation is probably not favored from a viewpoint of free energy. Based on our experimental result, a stand-conformation is presumed to form and greatly affect the total covered area, where most of the PS grafted chains collapse and are stabilized by PAA segments in free solution, while few of them can anchor on the interface, resulting in a much smaller A_{tot} compared to PS-PAA-PS for a given concentration.

In recent years, amphiphilic assembled structures have received much attention as potential carriers for biologically active ingredients, specially drugs [53–57]. Therefore, we further explored the solubilization ability of HB-(PAA)$_n$-*g*-(PS)$_{n+1}$ copolymers by using pyrene as a model hydrophobic compound. In our experiments, acetone solution of pyrene was first allowed to evaporate overnight from the vial, leaving a thin pyrene film inside. Then, 2 mL of HB-(PAA)$_n$-*g*-(PS)$_{n+1}$ micellar solutions (40 mM Na_2CO_3) were transferred into the vials and vigorously stirred to ensure the achievement of the maximum loading. As shown in Fig. 5.32, the UV–vis spectra of pyrene solutions show two characteristic absorption peak located at 324 and 340 nm, and the peak strength increases with polymer concentration, where the extinction coefficient and saturated solubility of pyrene in pure water is 29,500 M^{-1} cm^{-1} (340 nm) and 6.44 × 10^{-7} M according to literatures [58, 59].

More quantitatively, we plot the normalized concentration ($C_{py,s}/C_{py,w}$) of solubilized pyrene against polymer concentration in Fig. 5.33a, where $C_{py,s}$ and $C_{py,w}$ represent the measured pyrene concentration in micellar solution and the saturated concentration in pure water, respectively. As shown in Fig. 5.33a, $C_{py,s}/C_{py,w}$ linearly increases with polymer concentration for all HB-(PAA)$_n$-*g*-(PS)$_{n+1}$ copolymers with different n values. Moreover $(C_{py,s}/C_{py,w})_{n=1} > (C_{py,s}/C_{py,w})_{n=10} > (C_{py,s}/C_{py,w})_{n=47}$, indicating the solubilization efficiency of HB-(PAA)$_n$-*g*-(PS)$_{n+1}$ copolymers decreases with the size or branching degree of hyperbranched PAA core for a given polymer concentration. As we know, pyrene molecules mainly

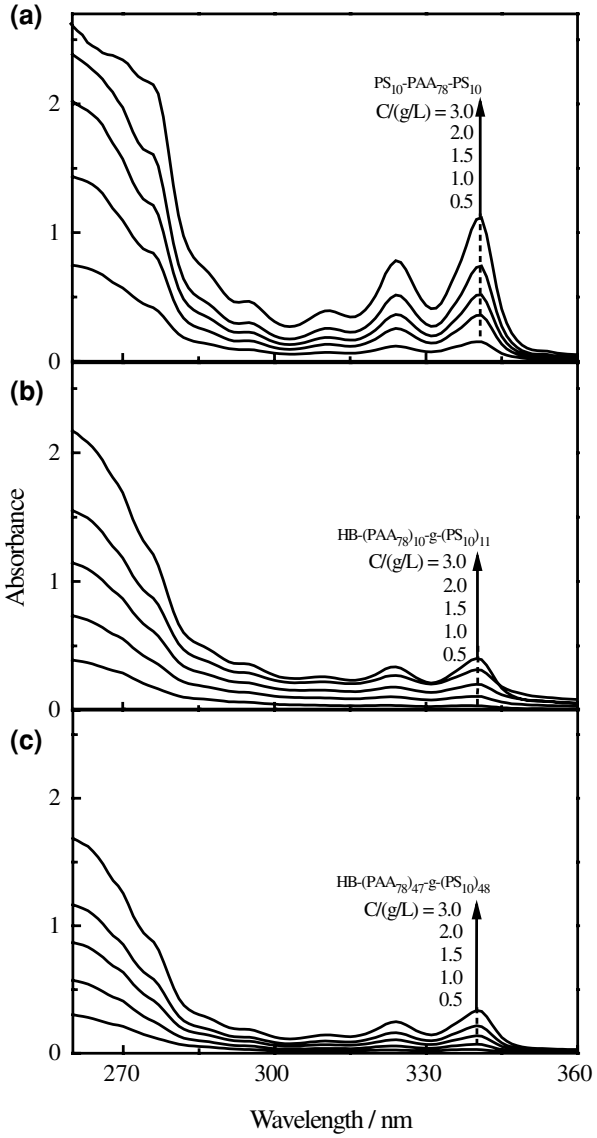

Fig. 5.32 UV–vis spectra of pyrene solutions solubilized by **a** PS-PAA-PS, **b** HB-$(PAA)_{10}$-*g*-$(PS)_{11}$ and **c** HB-$(PAA)_{47}$-*g*-$(PS)_{48}$ chains with different concentrations

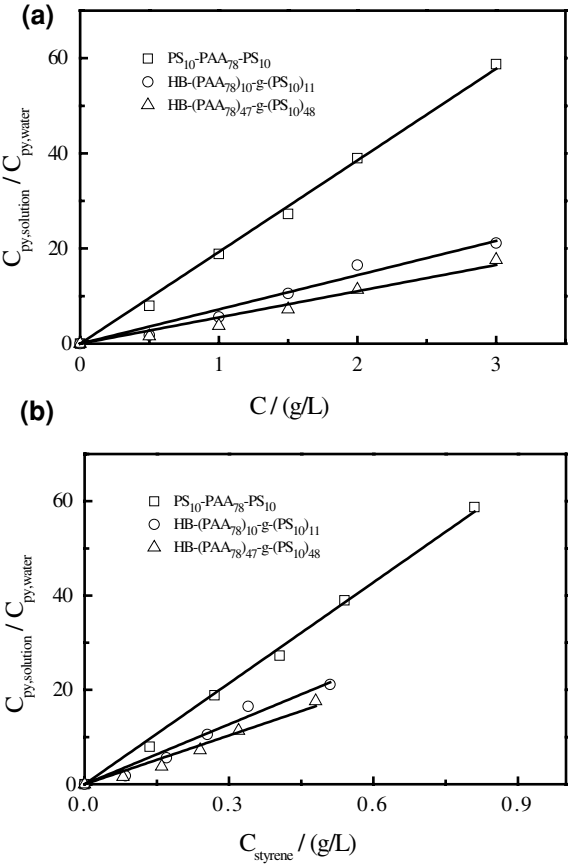

Fig. 5.33 **a** Polymer concentration and **b** styrene component concentration of HB-$(PAA)_n$-g-$(PS)_{n+1}$ copolymers dependence of $C_{py,s}/C_{py,w}$, where $C_{py,s}$ and $C_{py,w}$ represent the dissolved pyrene concentration in micellar solution and pure water, respectively

exist in the PS hydrophobic domains, while we have previously elucidated the weight fraction (wt%) of hydrophobic styrene of HB-$(PAA)_n$-g-$(PS)_{n+1}$ copolymers decreases with n; therefore, an attentive reader may attributed such different solubilization efficiency to the different styrene weight fraction. To clarify this point, we further re-plot $C_{py,s}/C_{py,w}$ against styrene component concentration ($C_{styrene}$) in Fig. 5.33b. As expected, $C_{py,s}/C_{py,w}$ still decreases as n for a given $C_{styrene}$, indicating it is the topology, instead of the styrene weight fraction, that dominates the solubilization ability of amphiphilic copolymers in solution. Actually, it is not hard to understand such topology-dependent solubilization efficiency, namely, previously we have observed the suppression of association of hydrophobic PS chains between different HB-$(PAA)_n$-g-$(PS)_{n+1}$ chains become more and more significant as n increases, which means the formation probability of hydrophobic domains comprising of PS chains also decreases with n, inevitably decreasing the ability of solubilizing water-insoluble molecules.

5.4 Crystallization Property of Hyperbranched Hetero-subchain Copolymer HB-(PS-*b*-PCL)$_n$

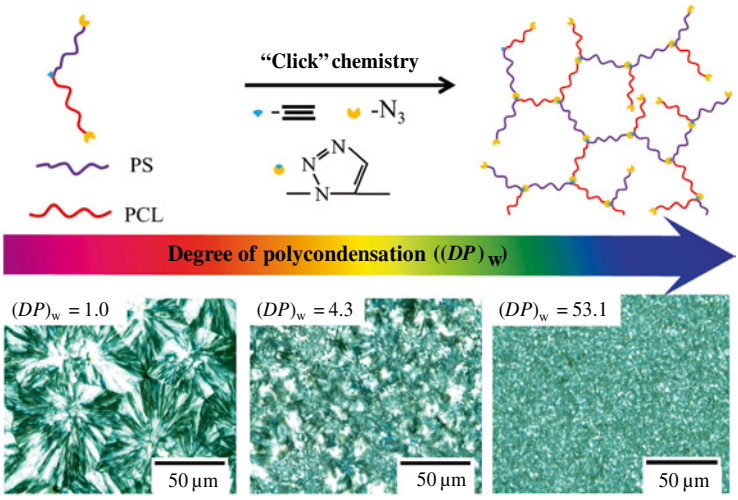

Previous results of hyperbranched polystyrene homopolymers showed that the hyperbranched homopolymer chains keep the fractal structure [60]; namely, their size (R) and intrinsic viscosity ([η]) in toluene are scaled to their overall weight average molar masses (M_w) and the weight average subchain molar mass ($M_{w,s}$) as $R \sim M_w^{\gamma} M_{w,s}^{\varphi}$ with $\gamma = 0.47 \pm 0.01$ and $\varphi = 0.10 \pm 0.01$; and $[\eta] \sim M_w^{\nu} M_{w,s}^{\mu}$ with $\nu = 0.39 \pm 0.01$ and $\mu = 0.31 \pm 0.01$. The question is whether a hyperbranched hetero-subchain copolymer chain with two different and alternative subchains still keeps its fractal character. Figure 5.34 is the first experimental result about such a [η]-M_w relationship, where we also plot the [η]-M_w relationships for linear PCL and PS (dashed lines) for comparison [61, 62]. To the best of our knowledge, there is no theory to predict how [η] is related to M_w for large hyperbranched copolymer chains in solutions up to now.

Figure 5.34 also shows that for both HB-(PS$_{18}$-*b*-PCL$_{28}$)$_n$ and HB-(PS$_{39}$-*b*-PCL$_{28}$)$_n$, log[η] linearly increases with logM_w, indicating that their structures remain fractal-like. The least-square fittings result in $\nu = 0.48 \pm 0.01$ and 0.45 ± 0.01, respectively, for HB-(PS$_{18}$-*b*-PCL$_{28}$)$_n$ and HB-(PS$_{39}$-*b*-PCL$_{28}$)$_n$, much smaller than those for linear homopolymers, as expected because a hyperbranched chain is more compact than its linear counterpart for a given overall molar mass. On the other hand, Fig. 5.34 shows that [η] of HB-(PS$_{18}$-*b*-PCL$_{28}$)$_n$ is lower than that of HB-(PS$_{39}$-*b*-PCL$_{28}$)$_n$ for a given M_w, which is attributed to their different branching densities because shorter subchains lead to a higher branching density.

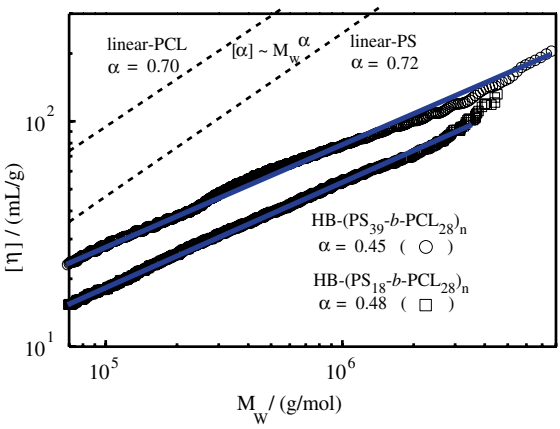

Fig. 5.34 Weight average molar masses (M_w) dependence of intrinsic viscosities ([η]) of HB-(PS$_{39}$-*b*-PCL$_{28}$)$_n$ and HB-(PS$_{18}$-*b*-PCL$_{28}$)$_n$ in THF

PCL can be used for biomedical applications because of its excellent biocompatibility and biodegradability. However, its crystallization has an impact on its degradation rate and affects its application. Therefore, we further studied the crystallization of HB-(PS$_{18}$-*b*-PCL$_{28}$)$_n$ with different molar masses by polarizing optical microscopy (POM) and differential scanning calorimetry (DSC) measurements. As expected, the insertion of each PCL subchain between two branching points should suppress its crystallization. Figure 5.35a shows how the size and shape of the crystalline domain of HB-(PS$_{18}$-*b*-PCL$_{28}$)$_n$ change with its molar mass. For precursor N$_3$-PS$_{18}$-≡-PCL$_{28}$-N$_3$ ($(DP)_w = 1.0$), large integral spherocrystals are formed; for large hyperbranched chains with $(DP)_w = 12.1$, only few fragmentized crystals appear; and for even larger hyperbranched chains with $(DP)_w = 53.1$, no crystal is observed. The branching effect on the crystallization can be better viewed from the evolution of DSC curves (Fig. 5.35b). The precursor N$_3$-PS$_{18}$-≡-PCL$_{28}$-N$_3$ shows a broad crystallization peak at ~14 °C and a large melting peak at ~44 °C. The endothermic peak (the melting transition) at ~44 °C sharply decreases as the hyperbranched chains become larger, quantitatively reflecting in a decrease of the crystallinity degree (χ_c) from 46.3 to 1.0 %, whose calculation is detailed in the Supporting Information, similar to those reported by Kawaguchi et al. [63] for hyperbranched PLA homopolymers. It is interesting to note that a broad exothermic peak attributed to the crystallization is still observable for HB-(PS$_{18}$-*b*-PCL$_{28}$)$_n$ with $(DP)_w < 12.1$, but gradually shifts to a higher temperature as $(DP)_w$ increases. No exothermic peak was detected when $(DP)_w \geq 12.1$, indicating the crystallization was completely prohibited due to the constraint of the branching topology. The observed melting transition temperature (T_m ~ 44 °C) is lower than that of the PCL homopolymer (~64 °C) but similar to those reported by Pan et al. [64] for linear PCL$_{70}$-*b*-PS$_{24}$ diblock copolymer.

Moreover, no glass transition of linear PS$_{18}$ block was detected in both the heating and cooling processes, presumably because the short PS block has a low glass transition temperature (T_g) that is overlapped with the melting process of

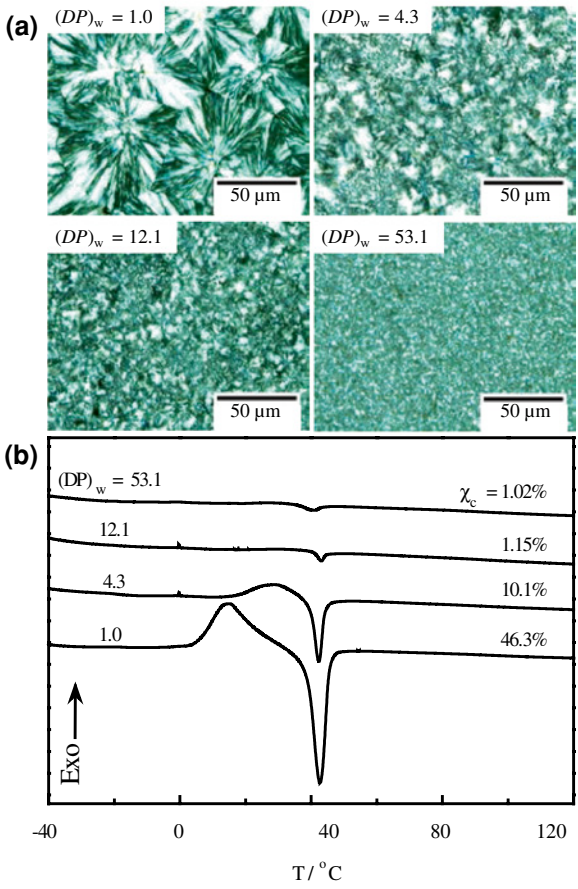

Fig. 5.35 Crystalline properties of HB-(PS_{18}-*b*-PCL_{28})$_n$ with different $(DP)_w$s: (**a**) POM photos and (**b**) DSC curves (10 °C/min) during reheating

PCL. Further, we found that HB-(PS_{39}-*b*-PCL_{28})$_n$ with a longer PS block shows no crystallization in either DSC or POM even for the precursor N_3-PS_{39}-≡-PCL_{28}-N_3 (Fig. 5.36), revealing that using a longer PS block can completely suppress the crystallization of the PCL blocks inside, in consistent with the reported results in literatures [65, 66].

The obtained result indicates that the hyperbranched topology, i.e., confining each PCL block between two branching points that are connected to two PS blocks with a proper length, can adjust or even completely suppress the crystallization of PCL, which makes PCL more suitable for different biomedical applications, i.e., controlling its biodegradation rate. It should be emphasized that this strategy in principle can be applied to any pair of vinyl and ring comonomers that can lead to hydrophobic or hydrophilic; and crystalline or amorphous blocks, e.g., methoxypoly(ethylene glycol) methacrylate and poly(methyl methacrylate).

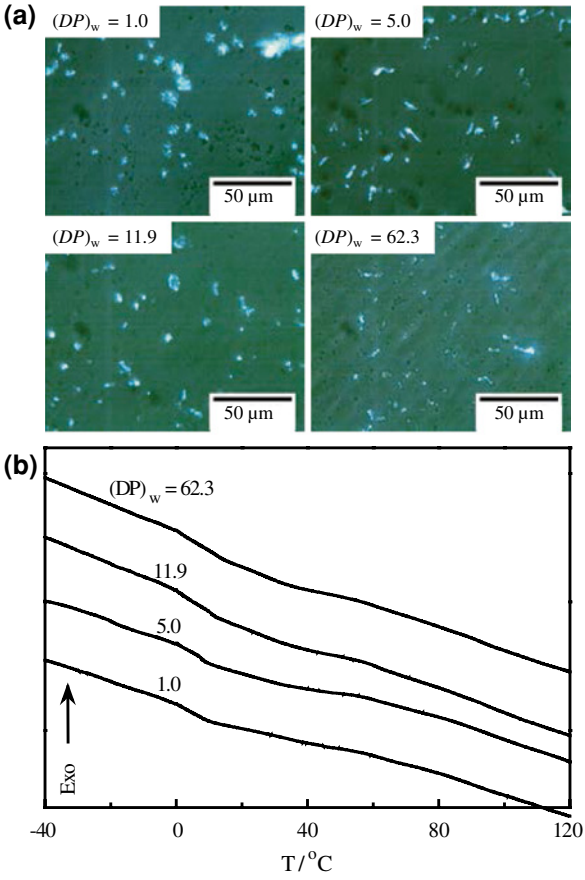

Fig. 5.36 Crystallinity properties of HB-$(PS_{39}$-*b*-$PCL_{28})_n$ with different $(DP)_w$s **a** POM photos and **b** DSC curves (10 °C/min) in the reheating process

5.5 Degradation Property of Degradable Hyperbranched Chains with Cleavable Disulfide Linkages

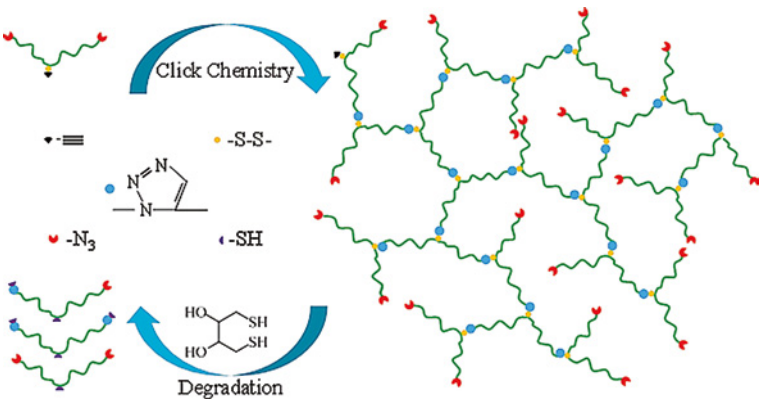

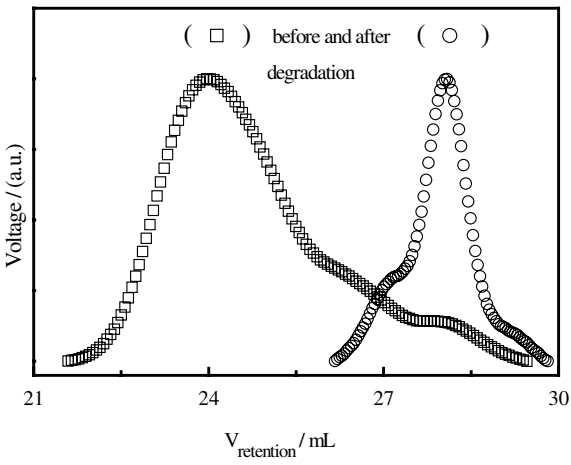

Fig. 5.37 SEC-RI curves of HB-(S-S-PS)$_{35}$ chains before and after 24-h DTT-induced reduction in DMF at 25 °C, where [DTT]/[-S-S-] = 18

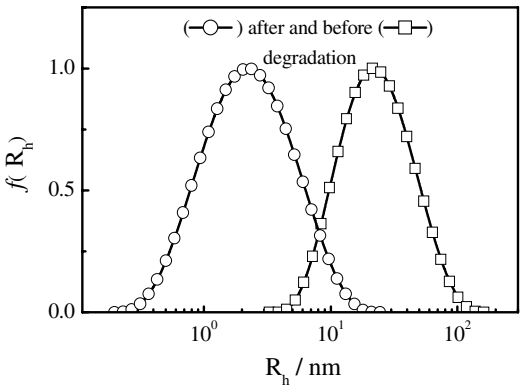

Fig. 5.38 Hydrodynamic radius distributions [$f(R_h)$] of HB-(S-S-PS)$_{35}$ chains before and after 24-h DTT-induced reduction in DMF at 25 °C, where [DTT]/[-S-S-] = 18

As mentioned in the previous chapters, applying our Seesaw-type macromonomer strategy, we have successfully synthesized model hyperbranched polystyrene HB-(S-S-PS)$_n$ chains with uniform subchains and controllably located cleavable disulfide linkages. In this section, the degradation kinetics of the prepared hyperbranched polystyrene chains in various organic solvents will be discussed in detail. There are different choices of reducing reagents, including thiols [67], phosphines [68, 69] and zinc dust [70]. DTT was selected in the current study because (1) its induced disulfide reduction is very efficient owing to its high conformational propensity to form a six member ring with an internal disulfide bond; (2) it is soluble in a range of organic solvents that can also dissolve polystyrene easily [71].

Figures 5.37 and 5.38 show how HB-(S-S-PS)$_{35}$ chains change after the 24-hour DTT induced reduction in DMF at 25 °C. As shown in Fig. 5.37, the elution peak located at ~24 mL completed disappears after the degradation and only the macromonomer peak (maybe contains few dimers) remains, indicating that

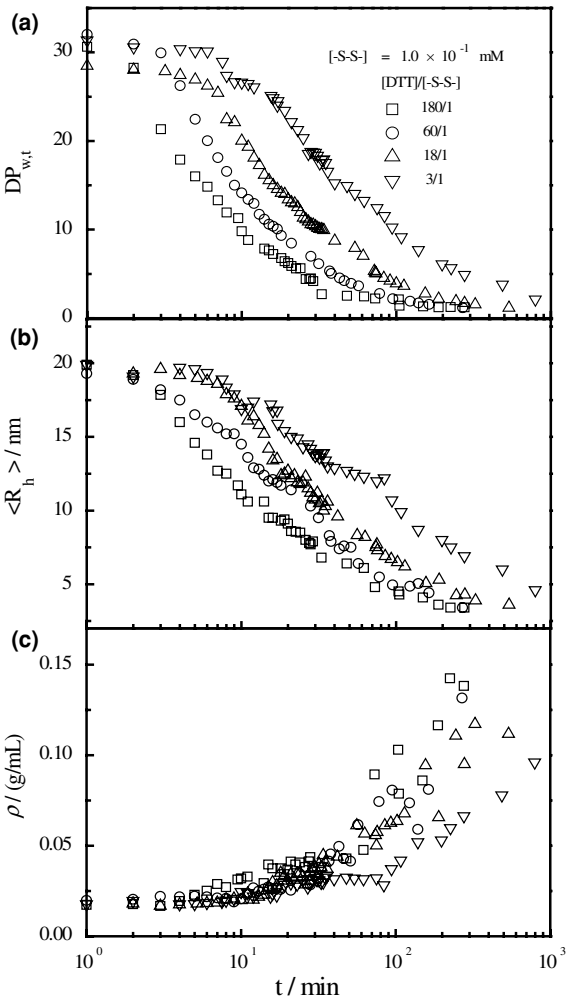

Fig. 5.39 Degradation time (t) dependence of **a** weight average degree of polycondensation ($DP_{w,t}$); **b** average hydrodynamic radius ($\langle R_h \rangle$); and **c** average chain density ($\langle \rho \rangle$) of HB-(S-S-PS)$_{35}$ in DMF at 25 °C

the DTT induced degradation of the initial HB-(S-S-PS)$_{35}$ chains is nearly 100 %. Such chain degradation is also directly reflected in the evolution of the hydrodynamic radius distribution [$f(R_h)$], as shown in Fig. 5.38 i.e., the peak position shifts from ~19 to ~3 nm after degradation. However, it should be noted that the degradation products are similar to the initial seesaw-type linear macromonomers except different end groups.

Figure 5.39 shows how the DP_w, $\langle R_h \rangle$, and average chain density ($\langle \rho \rangle$) of HB-(S-S-PS)$_{35}$ change during the degradation at different molar ratios of [DTT]/[-S-S-]; for the convenience of discussion, $DP_{w,t}$ is used to represent the value of DP_w at time t. As expected, $DP_{w,t}$, and $\langle R_h \rangle$ gradually decreases as the degradation (fragmentation) proceeds for a given [DTT]/[-S-S-] and the degradation rate becomes

higher when more DTT is added. We tested whether all the disulfide bonds can be completely degraded in the range of [DTT]/[-S-S-] = 3–180 and found that most of the initial disulfide bonds were cleaved within 5 h even at [DTT]/[-S-S-] = 3. Figure 5.39c demonstrates that the average chain density ($\langle\rho\rangle$), defined as $M_w/[N_A(4/3)\pi\langle R_h\rangle^3]$, increases with the degradation time, where M_w, $\langle R_h\rangle$ and N_A are the weight average molar mass, the average hydrodynamic radius of hyperbranched chains and the Avogadro's number, respectively. This shows that a branched polymer with a larger size has a lower chain density than its degradation product, and its linear macromonomer has the highest $\langle\rho\rangle$.

To analyze the results in Fig. 5.39, and considering the nature of thiol-disulfide exchanging reaction, we first assumed that the degradation follows the second-order kinetics, i.e.,

$$-\frac{\mathrm{d}[-\mathrm{S}-\mathrm{S}-]_t}{\mathrm{d}t} = k[-\mathrm{S}-\mathrm{S}-]_t[\mathrm{DTT}]_t \tag{5.21}$$

where [-S-S-]$_t$ and [DTT]$_t$ are the molar concentrations of disulfide bond and DTT at time t, respectively, and k is a reaction rate constant. At $t = 0$, [-S-S-]$_t$ = [-S-S-]$_0$; and at $t = \infty$, [-S-S-]$_t$ = 0. Since DTT is excessive, we can treat [DTT]$_t$ = [DTT]$_0$ as a constant in Eq. 5.21 so that we can rewrite it as a pseudo-first-order equation

$$\frac{[-\mathrm{S}-\mathrm{S}-]_t}{[-\mathrm{S}-\mathrm{S}-]_0} = e^{-k[\mathrm{DTT}]_0\, t} \tag{5.22}$$

On the other hand, it is well known that polystyrene is insoluble in diols so that most of DTT are excluded from the interior of HB-(S-S-PS)$_n$. Therefore, those external disulfide bonds would be cleaved first. In principle, the cleavage of each external disulfide bond leads to a decrease of DP_w by one. In this way, we are able to rewrite [-S-S-]$_t$/[-S-S-]$_0$ as $DP_{w,t}/DP_{w,0}$ so that Eq. 5.22 can be rewritten as:

$$DP_{w,t} = DP_{w,0}e^{-Kt} \tag{5.23}$$

where $DP_{w,t}$ and $DP_{w,0}$ are the degrees of polycondensation of hyperbranched chains at $t = t$ and $t = 0$, respectively, and $K = k[\mathrm{DTT}]_0$.

However, Fig. 5.40a shows that the single-exponential fitting of using Eq. 5.23 is not satisfactory, which forces us to include the degradation of those disulfide bonds inside the hyperbranched polystyrene chain. It is expected that the degradation of those internal disulfide bonds would be much slower due to (1) the lower concentration of DTT inside the polystyrene core and (2) the steric effect of the polystyrene segments around each internal disulfide bond. Empirically, we found that adding a slow degradation process into Eq. 5.23 enables us to fit all the curves in Fig. 5.40b by using a double exponential fitting as follows:

$$\frac{DP_{w,t}}{DP_{w,0}} = A_{\mathrm{fast}}e^{-K_{\mathrm{fast}}t} + A_{\mathrm{slow}}e^{-K_{\mathrm{slow}}t} \tag{5.24}$$

where A and K are two constants, representing the relative contributions and rate constants of the slow and fast degradation reactions, respectively;

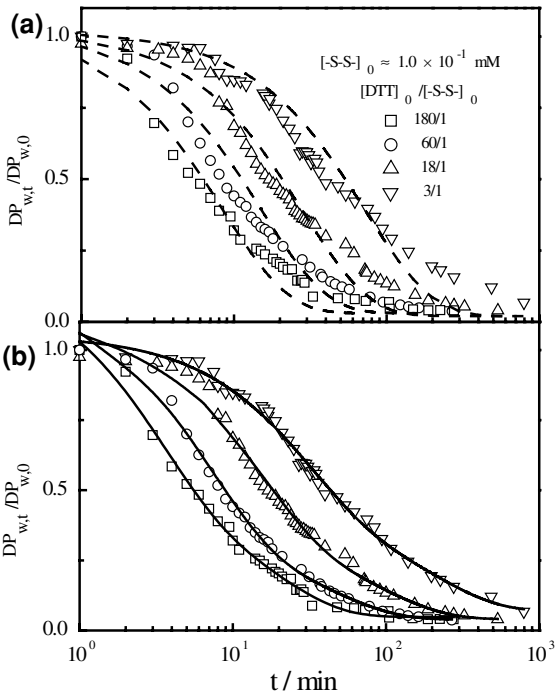

Fig. 5.40 DTT-induced degradation time (t) dependence of normalized weight average degree of polycondensation ($DP_{w,t}/DP_{w,0}$) of HB-(S-S-PS)$_{35}$ in DMF at 25 °C, where **a** (*dash*) and **b** (*continuous lines*) represent a single exponential fitting (Eq. 5.23) and a double exponential fitting (Eq. 5.24), respectively

$A_{fast} + A_{slow} = 1.0$. The reasonable double exponential fitting actually reveals that the degradation of disulfide bonds on the periphery of the hyperbranched chain is much faster than those inside.

Moreover, Fig. 5.41a shows that the fast degradation contributes twice more than the slow one; namely, ~2/3 of the disulfide bonds are on the periphery. It is interesting to find that the contributions of the fast and slow degradations are independent on the DTT concentration, presumably because the distribution of the disulfide bonds inside a hyperbranched chain is not influenced by the presence of DTT. In addition, Fig. 5.41b reveals that both K_{fast} and K_{slow} increase linearly with the DTT concentration, i.e., $K_{fast} = k_{fast}[DTT]_0$ and $K_{slow} = k_{slow}[DTT]_0$, indicating that the cleavage of the disulfide bond on a polymer chain by DTT is very similar to those small molecule thiol-disulfide exchange reactions [72–74]. It is worth noting that both k_{fast} and k_{slow} are much smaller than the apparent rate constants (10^5–10^6 min^{-1} M^{-1}) of small molecule thiol-disulfide exchange reactions in DMF [75].

Finally, we studied the effect of solvent on the degradation kinetics of HB-(S-S-PS)$_{35}$ because it is practically important to choose a proper solvent to degrade a given polymer chain. Figure 5.42 shows that the degradation rate increases with the solvent polarity. To our knowledge, this is the first study of how the solvent polarity affects the degradation kinetics of disulfide-functionalized hyperbranched polymers. Quantitatively, the fast and slow degradation rate constants in DMF

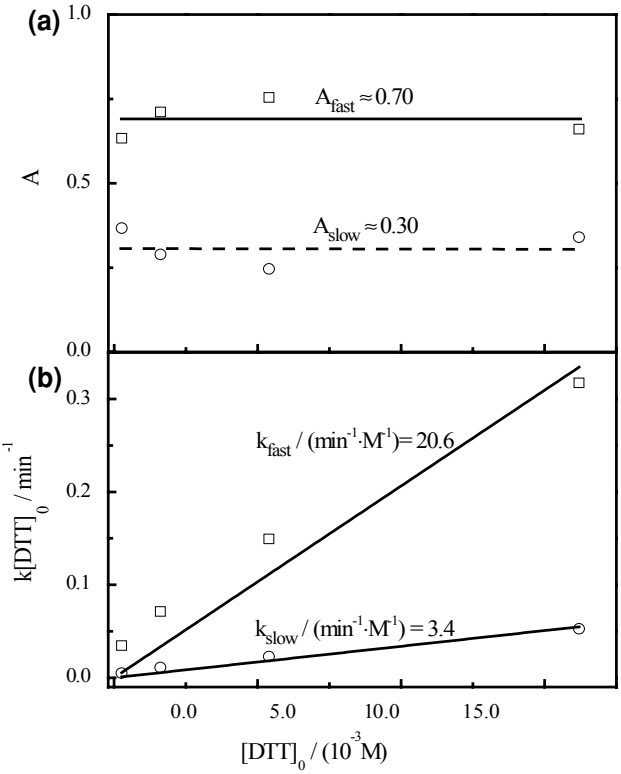

Fig. 5.41 DTT initial concentration ($[DTT]_0$) dependence of **a** relative contributions (A) of fast and slow degradation processes and **b** reaction rate constants k_{fast} and k_{slow} calculated from fitting of data in Fig. 5.40 on the basis of Eq. 5.24

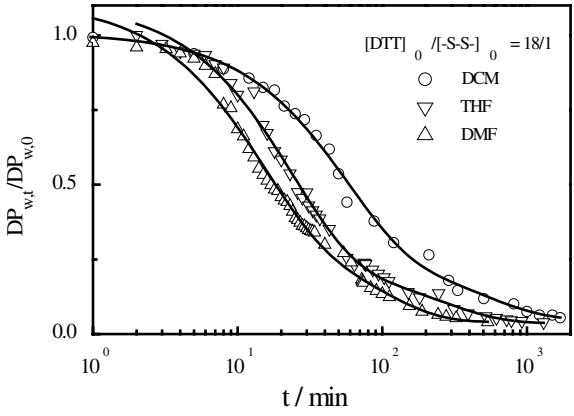

Fig. 5.42 DTT-induced degradation time (t) dependence of normalized weight average degree of polycondensation ($DP_{w,t}/DP_{w,0}$) of HB-(S-S-PS)$_{35}$ in three different solvents at 25 °C, where *lines* represent double exponential fittings of Eq. 5.24

are ~2 and ~5 times higher than those in THF and DCM, respectively. It has been known that the reducing power of DTT depends on how easily the thiol groups of DTT are ionized into the thiolate form -S^- because only a free thiolate can attack the disulfide linkage on a chain. Generally, organic solvents with a higher polarity are able to polarize the thiol group to produce more free thiolate.

This part of work demonstrates that the degradation process presents a fast and slow two-step characteristic, namely, the degradation rate of the external disulfide bonds are much faster than that of the internal ones due to a higher DTT local concentration and weaker steric effect of the polystyrene segments. It should be emphasized that not only the category of monomer and cleavable linkage, but also the coupling method can be varied for our developed synthetic strategy. Thus, our current study provides not only a standard route for the construction of model degradable hyperbranched polymers, but also useful experimental data for further study on the correlation between microscopic structures and macroscopic properties of degradable hyperbranched polymers in the future.

References

1. Rubinstein M, Colby RH (2003) Polymer physics. Oxford University Press, New York
2. Teraoka I (2002) Polymer solutions: an introduction to physical properties. Wiley, NY
3. Lewis ME, Nan S, Mays JW (1991) Macromolecules 24:197
4. Miyaki Y, Einaga Y, Fujita H, Fukuda M (1980) Macromolecules 13:588
5. Kniewske R, Kulicke W-M (1983) Die Makromol Chem 184:2173
6. Mourey TH, Turner SR, Rubinstein M, Frechet JMJ, Hawker CJ, Wooley KL (1992) Macromolecules 25:2401
7. La Ferla R (1997) J Chem Phys 106:688
8. Drew PM, Adolf DB (2005) Soft Matter 1:146
9. Lu Y, Shi T, An L (2011) Acta Polym Sin 9:1069
10. Lu Y, An L, Jin L, Wang Z-G (2013) Macromolecules 46:5731
11. Voit BI, Lederer A (2009) Chem Rev 109:5924
12. Turner SR, Voit BI, Mourey TH (1993) Macromolecules 26:4617
13. Zhang C, Zhou Y, Liu Q, Li S, Perrier S, Zhao Y (2011) Macromolecules 44:2034
14. Zimm BH, Stockmayer WH (1949) J Chem Phys 17:1301
15. Isaacson J, Lubensky TC (1980) J Phys Lett 41:469
16. Burchard W (2004) Macromolecules 37:3841
17. Burchard W (1972) Macromolecules 5:604
18. Burchard W (1977) Macromolecules 10:919
19. Galinsky G, Burchard W (1997) Macromolecules 30:4445
20. Burchard W (1983) Static and dynamic light scattering from branched polymers and biopolymers light scattering from polymers, vol 48. Springer, Berlin, p 1
21. Lu YY, Shi TF, An LJ, Wang ZG (2012) Europhys Lett 97:64003
22. Lu Y, Shi T, An L, Jin L, Wang Z-G (2010) Soft Matter 6:2619
23. Galina H, Lechowicz JB, Walczak M (2002) Macromolecules 35:3253
24. Galina H, Lechowicz JB, Walczak M (2002) Macromolecules 35:3261
25. Burchard W, Khalyavina A, Lindner P, Schweins R, Friedel P, Wiemann M, Lederer A (2012) Macromolecules 45:3177
26. Turner SR, Walter F, Voit BI, Mourey TH (1994) Macromolecules 27:1611
27. Lescanec RL, Muthukumar M (1990) Macromolecules 23:2280

28. Lyulin AV, Adolf DB, Davies GR (2001) Macromolecules 34:3783
29. Pyun CW, Fixman M (1964) J Chem Phys 41:937
30. Wang Y, Teraoka I, Hansen FY, Peters GH, Hassager O (2010) Macromolecules 44:403
31. Ge H, Wu C (2010) Macromolecules 43:8711
32. Cai J, Yue Y, Rui D, Zhang Y, Liu S, Wu C (2011) Macromolecules 44:2050
33. De Gennes PG (1974) J Chem Phys 60:5030
34. Pincus P (1976) Macromolecules 9:386
35. Casassa EF, Tagami Y (1969) Macromolecules 2:14
36. Freed KF (2011) J Chem Phys 135:144902
37. Freed KF, Wu C (2011) Macromolecules 44:9863
38. Ge H, Jin F, Li J, Wu C (2009) Macromolecules 42:4400
39. Ge H, Pispas S, Wu C (2011) Polym Chem 1071:2
40. Gay C, de Gennes PG, Raphael E, Brochard-Wyart F (1996) Macromolecules 29:8379
41. Gennes PGD (1999) Adv Polym Sci 38:92
42. Render S (1979) J Phys A: Math Gen 12:L239
43. Jin F, Wu C (2006) Phys Rev Lett 96:237801
44. Wu C, Li L (2013) Polymer 54:1463
45. Hong L, Zhu F, Li J, Ngai T, Xie Z, Wu C (2008) Macromolecules 41:2219
46. Zhang Q (2008) Macromolecules 41:2228
47. Burguière C, Pascual S, Bui C, Vairon J-P, Charleux B, Davis KA, Matyjaszewski K, Bétremieux I (2001) Macromolecules 34:4439
48. Burguière C, Chassenieux C, Charleux B (2003) Polymer 44:509
49. Gaillard N, Guyot A, Claverie J (2003) J Polym Sci Pol Chem 41:684
50. Riess G, Labbe C (2004) Macromol Rapid Comm 25:401
51. Tan B, Nabuurs T, Feijen J, Grijpma DW (2009) J Polym Sci Pol Chem 47:4234
52. Muñoz-Bonilla A, van Herk AM, Heuts JPA (2010) Macromolecules 43:2721
53. Teng Y, Morrison ME, Munk P, Webber SE, Procházka K (1998) Macromolecules 31:3578
54. Cho SY, Allcock HR (2007) Macromolecules 40:3115
55. Vyhnalkova R, Eisenberg A, van de Ven TGM (2008) J Phys Chem B 112:8477
56. Kannaiyan D, Imae T (2009) Langmuir 25:5282
57. Zhou Z, D'Emanuele A, Lennon K, Attwood D (2009) Macromolecules 42:7936
58. Almgren M, Grieser F, Thomas JK (1979) J Am Chem Soc 101:279
59. Yang H, Morris JJ, Lopina ST (2004) J Colloid Interf Sci 273:148
60. Li L, Lu Y, An L, Wu C (2013) J Chem Phys 138:114908
61. Huang Y, Xu Z, Huang Y, Ma D, Yang J, Mays JW (2003) Int J Polym Anal Charact 8:383
62. Brandrup J, Immergut EH, Grulke EA (1999) Polymer Handbook, 4th edn. Wiley, New York
63. Jikei M, Suzuki M, Itoh K, Matsumoto K, Saito Y, Kawaguchi S (2012) Macromolecules 45:8237
64. Shi G-Y, Sun J-T, Pan C-Y (2011) Macromol Chem Phys 212:1305
65. Zhao Y-F, Fan X, Chen X, Wan X, Zhou Q-F (2005) Polymer 46:5396
66. Heuschen J, Jérôme R, Teyssié PJ (1989) J Polym Sci Pol Phys 27:523
67. Stals PJM, Li Y, Burdyńska J, Nicolaÿ R, Nese A, Palmans ARA, Meijer EW, Matyjaszewski K, Sheiko SS (2013) J Am Chem Soc 135:11421
68. Humphrey RE, Hawkins JM (1964) Anal Chem 1812:36
69. Humphrey RE, Potter JL (1965) Anal Chem 37:164
70. Overman LE, Smoot J, Overman JD (1974) Synthesis 1974:59
71. Tsarevsky NV, Matyjaszewski K (2002) Macromolecules 35:9009
72. Gallogly MM, Starke DW, Mieyal JJ (2009) Antioxid Redox Sign 1059:11
73. Lukesh JC, Palte MJ, Raines RT (2012) J Am Chem Soc 134:4057
74. Wiita AP, Ainavarapu RK, Huang HH, Fernandez JM (2006) Proc Natl Acad Sci USA 103:7222
75. Emrick T, Chang H-T, Fréchet JMJ (1999) Macromolecules 32:6380

Chapter 6
Conclusion

In conclusion, by overcoming the disadvantage of the previous synthetic methods for the preparation of hyperbranched polymers, we designed an all-new Seesaw-type macromonomer strategy to construct "perfect" hyperbranched model samples with uniform subchains. In our study, we successfully prepared various kinds of Seesaw-type macromonomers, such as homopolymers, triblock copolymers and diblock copolymers. Using these macromonomers as precursors, we have further prepared a series of "perfect" hyperbranched homopolymers, block copolymers, graft copolymers and hetero-subchain copolymers by a combination of controlled/living polymerization and "click" chemistry. Various solution properties of these novel hyperbranched (co) polymers in dilute and semidilute solutions have been studied in detail. More specifically, the main achievements of this work are as follows:

1. Successfully synthesized Seesaw-type polystyrene macromonomer and its corresponding "perfect" hyperbranched polystyrene homopolymer; monitored the "click" self-polycondensation process by a combination of size-exclusion-chromatography equipped with a multi-angle-laser-light-scattering detector (SEC-MALLS) and stand-alone laser light scattering (LLS); and found that the reaction follows the 2nd-order kinetics with a time-dependent reaction rate constant; namely, $k_{AB} = k_{AB,0}/[1 + (\beta t)^2]$, where $k_{AB,0}$ is the initial rate constant at $t = 0$, and $1/\beta$ is the time at which k_{AB} decreases to 50 % of its initial value and related to the molar concentration ($[C]$) and molar mass (M) as $1/\beta \sim [C]^{-0.35} M^{0.55}$, implying that the the reaction is governed by the interchain distance and diffusion.
2. Systematically characterized a set of "perfect" fractionated hyperbranched polystyrenes with different subchain lengths by using a combination of LLS and viscosity measurements and found that both the polymerization degrees of the subchain (N_b) and the whole chain (N_t) are scaled to the average radius of gyration ($\langle R_g \rangle$), average hydrodynamic radius ($\langle R_h \rangle$) and the intrinsic viscosity ($[\eta]$) as: $\langle R_g \rangle \sim N_t^{0.46} N_b^{0.11}$, $\langle R_h \rangle \sim N_t^{0.48} N_b^{0.09}$ and $[\eta] = K_\eta M_w^{0.39} M_{w,b}^{0.31}$,

L. Li, *Studies on "Perfect" Hyperbranched Chains Free in Solution and Confined in a Cylindrical Pore*, Springer Theses, DOI: 10.1007/978-3-319-06097-2_6,

respectively. These scaling laws clearly demonstrate the fractal nature of these hyperbranched chains.

3. Directly balanced the confinement and hydrodynamic forces ($f_c = k_B T/\xi$ and $f_h = 3\pi\eta u l_e$) on each "blob" of a polymer chain entrapped inside a small cylindrical tube with a diameter of D under an elongation flow instead of considering the free energy (de Gennes' arguments) to obtain a unified description of how polymer chains with different topologies (linear, star and branched) crawl through such a tube. Namely, the critical flow rate (q_c) is related to the blob size (ξ) and D as $q_c/q_{c,linear} = (D/\xi)^2$. For a confined linear chain, $\xi_{linear} = D$; for a star chain, $\xi_{star} = [2/(f + |f - 2f_{in}|)]^{1/2} D$, where f and f_{in} represent the total arm number and the number of the forwarded arms inserted into the tube; for a hyperbranched chain, $\xi_{branch} = (D/b)^{\alpha'} N_{t,Kuhn}{}^{\beta'} N_{b,Kuhn}{}^{\gamma'}$, where b is the size of one Kuhn segment, $N_{t,Kuhn}$ and $N_{b,Kuhn}$ are respectively the numbers of Kuhn segments of the entire branched chain and the subchain between two neighboring branching points; and the three constant exponents (α', β' and γ') are directly related to the well-known Flory's scaling exponents between the chain size and $N_{t,Kuhn}$ or $N_{t,Kuhn}$.
4. Quantitatively revealed how the N_b and N_t affect the deformation property of one hyperbranched chain, namely, the measured critical flow rate ($q_{c,branch}$) of hyperbranched chains passing through a small cylindrical pore is affected by both N_b and N_t as $q_{c,branch} \sim N_t^{\gamma} N_b^{\varphi}$ with $\gamma = 1.0 \pm 0.1$ and $\varphi = -0.4 \pm 0.1$. In addition, we also found that $q_{c,branch}$ decreases as the pore size D increases. The deviation between our experimental results and previous theoretical predictions is attributed to some inappropriate assumptions used before. Using the difference between the critical flow rates of different chains, we are able to separate hyperbranched chains with a similar hydrodynamic size but different subchain lengths.
5. Further prepared amphiphilic hyperbranched block copolymers and studied the intrachain folding and interchain association of these amphiphilic chains in dilute and semidilute solutions and found that individual hyper-(P*t*BA$_{36}$–PS$_{55}$–P*t*BA$_{36}$)$_{600}$ chains can undergo the intrachain folding in cyclohexane selectively poor for PS at lower temperatures; namely, each PS block collapses into a small globule stabilized by its three neighboring soluble P*t*BA blocks without any intrachain or intrachain association. For hyper-(PAA$_{23}$–PS$_{14}$–PAA$_{23}$)$_n$ chains with different molar masses in water, our results indicate that the average aggregation number (N_{agg}) increases as the weight average degree of polymerization [$(DP)_w$] decreases, i.e., $N_{agg} \sim (DP)_w^{-0.7}$, revealing that smaller chains tend to associate more. Unlike their linear precursors, hyper-(PAA$_{23}$–PS$_{14}$–PAA$_{23}$)$_n$ chains are able to form a physical gel and its strength increases with the initial concentration and molar mass of hyperbranched chains.
6. Successfully constructed amphiphilic hyperbranched graft copolymer made of a large hyperbranched poly(acrylic acid) core and a number of grafted short polystyrene stickers, i.e., (HB–PAA$_n$–g-PS$_{n+1}$) with different n values (n = 1, 10, 47) and found both of the chain topology and styrene content can greatly

affect the solution properties of HB-PAA$_n$–g-PS$_{n+1}$. Namely, the increase of n will lead to a weaker tendency of interchain associatin, a lower emulsifying ability, and a poorer solubilization efficiency.

7. Successfully prepared Seesaw-type diblock macromonomer (N_3–PS–≡–PCL–N_3) and model hyperbranched hetero-subchain copolymer [HB–(PS–*b*-PCL)$_n$] with controllable and uniform PS and PCL subchains, and found that such prepared hyperbranched copolymer chains still have a fractal-like structure, and the PCL subchains inside HB–(PS–*b*-PCL)$_n$ crystallize less as the branching degree increases and the PS subchain becomes longer. This work demonstrates that we can use the chain topology to control the crystallization of PCL subchains inside hyperbranched copolymers to regulate their biodegradation for biomedical applications.
8. Finely prepared degradable hyperbranched model structure with uniform subchains and controlled locations of cleavable disulfide linkages simultaneously, and studied the dithiothreitol (DTT) induced degradation of these chains in various organic solvents, and found that the internal and external disulfide bonds of hyperbranched polystyrene chains contributed to the degradation in two different ways, which is due to the different local concentrations of DTT and PS segment around an individual disulfide bonds inside and outside the PS coil.

Chapter 7
Experimental Part

7.1 Materials

Styrene (St, Sinopharm, 97 %) and *tert*-butyl acrylate (*t*BA, Sinopharm, 97 %) were first passed through a basic alumina column to remove inhibitor and then distilled under reduced pressure over CaH_2. ε-caprolactone (CL, Aladdin, 99 %) were dried over CaH_2 and distilled under a reduced pressure. Dimethylformamide (DMF, Sinopharm, AR) was first dried with anhydrous magnesium sulfate and then distilled under reduced pressure prior to use. Dichloromethane (DCM) and triethylamine (TEA) from Sinopharm were distilled over CaH_2 just prior to use. Acetone was distilled over anhydrous K_2CO_3. Toluene (Sinopharm, 97 %) was refluxed over sodium for 24 h, and then distilled. Copper(I) bromide (CuBr, Alfa, 98 %) was washed with glacial acetic acid to remove soluble oxidized species, filtrated, washed with ethanol and dried under vacuum. Tris(2-(dimethylamino)-ethyl)amine (Me_6TREN, Aldrich, 99 %), *N*,*N*,*N*′,*N*′,*N*″-Pentamethyl-diethylenetriamine (PMDETA, Aldrich, 99 %), anisole (Alfa, 99 %), 2,2′-bipyridine (bpy, Fluka, 99 %), sodium azide (NaN_3, Aldrich, 99 %), 2,2-bis(hydroxymethyl) propionic acid (DMPA, Fluka, 97 %), *N*,*N*-dimethyl-4-amidopyridine (DMAP, Aladdin, 99 %), dicyclohexyl carbodiimide (DCC, Aladdin, 99 %), 2-bromoisobutyryl bromide (Aladdin, 98 %), *p*-toluenesulfonic acid monohydrate (PTSA, Aladdin, 99 %), 2,2-dimethoxypropane (DMP, Aladdin, 99 %), and tin(II)-2-ethylhexanoate ($Sn(EH)_2$, Aladdin, 95 %) were directly used as received. In emulsion polymerization, Milli-Q water was used. In degradation experiments, DMF, THF and DCM were bubbled with nitrogen for 5 h before used. Dithiothreitol (DTT, Aladdin, 99 %) was stored under nitrogen flow at 2–6 °C. Other analytic grade reagents from Sinopharm were used as received.

L. Li, *Studies on "Perfect" Hyperbranched Chains Free in Solution and Confined in a Cylindrical Pore*, Springer Theses, DOI: 10.1007/978-3-319-06097-2_7,

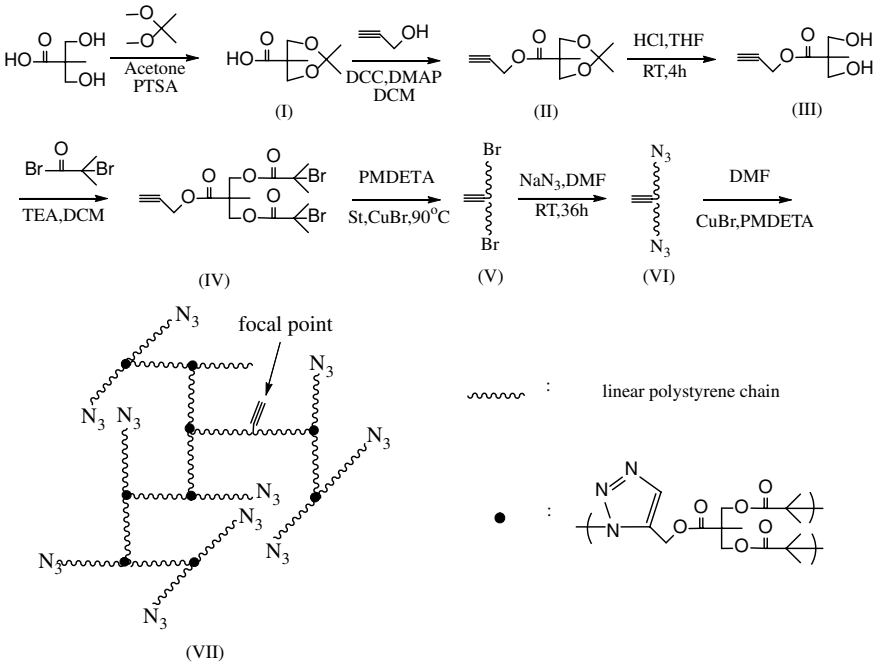

Fig. 7.1 Schematic synthesis of macromonomer and hyperbranched polystyrene

7.2 Experimental Details About Hyperbranched Polystyrene Homopolymers

7.2.1 Synthesis of Macromonomers and Hyperbranched Polymers

Figure 7.1 shows a schematic chemical synthesis of different chemicals required to prepare linear Seesaw-type macromonomer chains with two azide end groups and one middle alkyne group as well as the self-polycondensation via "click" chemistry between azide and alkyne.

Isopropylidene-2,2-bis(methoxy)propionic Acid (I)

2,2-Bis(hydroxymethyl) propionic acid 30.00 g (223.7 mmol), 2,2-dimethoxypropane (41.4 mL, 335.4 mmol) and *p*-toluenesulfonic acid monohydrate (2.10 g, 11.1 mmol) were dissolved in 100 mL of acetone. The mixture was stirred for 4 h at room temperature before 3.0 mL mixture of an ammonia solution (25 %) and EtOH (50/50, v/v)) was added into the reaction mixture to neutralize the catalyst. The solvent was removed by evaporation under reduced pressure at room temperature. The residue was then dissolved in CH_2Cl_2 (600 mL) and extracted with two portions of water (80 mL). The organic phase was dried with anhydrous Na_2SO_4 and evaporated to give **(I)** as white powder (33.0 g, 84 %). The ^{1}H NMR spectra

were recorded on a commercial Bruker AV400 NMR spectrometer using $CDCl_3$ as solvent and tetramethylsilane (TMS) as an internal standard. ^1H NMR ($CDCl_3$, ppm): δ 4.18 (d, 2H, $–CH_2O(CH_3)C(CH_3)OCH_2–$), 3.65 (d, 2H, $–CH_2O(CH_3)C–$ $(CH_3)OCH_2–$), 1.41(s, 3H, $–CH_2O(CH_3)C(CH_3)OCH_2–$), 1.38 (s, 3H, $–CH_2O(CH_3)C(CH_3)–OCH_2–$), 1.20 (s, 3H, $CH_3C(CH_2O–)_2COOH$).

Propargyl 2,2,5-Trimethyl-1,3-dioxane-5-carboxylate (II)

Propargyl alcohol (14.7 mL, 256 mmol), isopropylidene-2,2-bis(methoxy)propionic acid (**I**) (29.8 g, 172 mmol), and DMAP (10.2 g, 84 mmol) was dissolved in 300 mL CH_2Cl_2. After stirring at room temperature for 10 min, DCC (42 g, 204 mmol) dissolved in 100 mL of CH_2Cl_2 was added dropwise into the mixture within 30 min under N_2 flow. Reaction mixture was stirred overnight at room temperature and urea byproduct was filtrated. The solution was then diluted by CH_2Cl_2 (800 mL) and extracted with two portions of water (150 mL), and the organic phase was dried with anhydrous Na_2SO_4. Solvent was evaporated and the remaining product was purified by column chromatography over silica gel eluting with hexane/ethyl acetate (25:1, v/v) to give colorless clear oil: 25.0 g (69 %). ^1H NMR ($CDCl_3$, ppm): δ 4.74 (d, 2H, $CH{\equiv}CCH_2O–$), 4.20 (d, 2H, $–CH_2O(CH_3)C(CH_3)OCH_2–$), 3.67 (d, 2H, $–CH_2O(CH_3)C(CH_3)OCH_2–$), 2.48 (t, 1H, $CH{\equiv}CCH_2O–$), 1.43 (s, 3H, $–CH_2O(CH_3)C(CH_3)OCH_2–$), 1.39 (s, 3H, $–CH_2O(CH_3)C(CH_3)O–CH_2–$), 1.22 (s, 3H, $CH_3\,C(CH_2O–)_2COOH$).

Propargyl 3-Hydroxy-2-(hydroxymethyl)-2-methylpropanoate (III)

Propargyl 2,2,5-tri-methyl-1,3-dioxane-5-carboxylate (II) (10.0 g, 47.5 mmol) was dissolved in a mixture of 1 M HCl (25 mL) and THF (25 mL). The reaction mixture was stirred for 4 h at room temperature. The precipitated product was filtrated off, and reaction mixture was then diluted by CH_2Cl_2 (400 mL) and extracted with two portions of water (70 mL) and the organic phase was dried with anhydrous Na_2SO_4 and concentrated. Hexane was added to the reaction mixture, and it was kept in deep freeze for 48 h to give white solid: 7.0 g (90 %). ^1H NMR ($CDCl_3$, ppm): 4.77 (d, 2H, $CH{\equiv}CCH_2O–$), 3.93 (d, 2H, $–CH_2OH$), 3.74 (d, 2H, $–CH_2OH$), 2.73 (br, 2H, –OH), 2.50 (t, 1H, $CH{\equiv}CCH_2O–$), 1.10 (s, 3H, $–CH_3$).

Propargyl 2,2-Bis((2′-bromo-2′-methylpropanoyloxy)methyl)propionate (IV)

Propargyl 3-hydroxy-2-(hydroxymethylN)-2-methylpropanoate (**III**) (4.5 g, 26.0 mmol) was first dissolved in 90 mL of CH_2Cl_2, and then triethyl amine (8.0 mL, 57.5 mmol) was added. After the mixture was cooled to 0 °C, 2-bromoisobutrylbromide (6.05 g, 26.0 mmol) in 40 mL of CH_2Cl_2 was added dropwise within 30 min. The reaction mixture was stirred overnight. After filtration, the mixture was extracted with CH_2Cl_2 (200 mL) and saturated aq. $NaHCO_3$ (50 mL). The aqueous phase was again extracted with CH_2Cl_2 (100 mL) and the combined organic phase was dried with anhydrous Na_2SO_4. The solution was concentrated and the crude product was purified by column chromatography over silica gel eluting with hexane/ethyl acetate (4:1, v/v) to give white crystal: 7.1 g (87 %). ^1H NMR ($CDCl_3$, ppm): δ 4.74 (d, 2H, $CH{\equiv}CCH_2O–$), 4.37 (m, 4H, $–COOCH_2–$), 2.47 (t, 1H, $CH{\equiv}CCH_2O–$), 1.92 (s, 12H, $–CBr(CH_3)_2$), 1.37 (s, 3H, $–CH_3$).

Polystyrene [Alkyne-(PSt-bromine)$_2$] (V) via an ARGET ATRP

The general procedure was as follows. A three-necked flask equipped with a magnetic stirring bar and three rubber septum was charged with PBMP (0.1 g, 0.210 mmol), St (24 mL, 210.0 mmol), Me_6TREN (55.4 μL, 0.210 mmol), $Sn(EH)_2$ (68.0 μL, 0.210 mmol) and anisole (24 mL). The flask was degassed by four freeze-pump-thaw cycles, and then placed in an oil bath thermostated at 90 °C. After ~2 min, CuBr (3 mg, 0.021 mmol) was introduced to start the polymerization under N_2 flow. After a few hours, the flask was rapidly cooled to room temperature and quenched with $CuBr_2$. The polymer mixture was diluted with THF, and passed through a short column of neutral alumina for the removal of metal salt. After removing all the solvents by a rotary evaporator, the residue was dissolved in THF and precipitated into an excess of methanol. The above purification cycle was repeated twice. After drying in a vacuum oven overnight at room temperature, polystyrene [alkyne-(PSt-bromine)$_2$] (V) was obtained. Yield: 8.1 g (37 %). M_n: 4.50 × 10^4 g/mol and M_w/M_n: 1.13 (by SEC).

Polystyrene [Alkyne-(PSt-azide)$_2$] (VI)

A 100 mL round–bottom flask was charged with alkyne-(PSt-bromine)$_2$ (5.0 g, 0.66 mmol), DMF (30 mL), and NaN_3 (0.325 g, 5 mmol). The mixture was allowed to stir at room temperature for 36 h. After removing most of the solvent under reduced pressure, the remaining portion was diluted with CH_2Cl_2, and then precipitated into an excess of methanol. The sediments were redissolved in CH_2Cl_2 and passed through a neutral alumina column to remove residual sodium salts, and then precipitated into an excess of methanol. After dried in a vacuum oven overnight at room temperature, linear Seesaw-type polystyrene with one alkyne functional group and two azide functional groups was obtained.

"Perfect" Hyperbranched PSt (VII)

The general procedure employed was as follows. A three-necked flask equipped with a magnetic stirring bar and three rubber septum was charged with alkyne-(PSt-azide)$_2$ macromonomer (2 g, 0.263 mmol), PMDETA (109.5 μL, 0.526 mmol) and DMF (13.3 mL). The flask was degassed by four freeze-pump-thaw cycles, and then placed in a water bath thermostated at 35 °C. After ~2 min, CuBr (75 mg, 0.526 mmol) was introduced to start the poly-condensation under N_2 flow. Samples were taken at timed intervals and precipitated into a mixture of methanol/water (90/10, v/v) and the products were washed with excess methanol. After drying in a vacuum oven overnight at 40 °C, the resultant hyperbranched polystyrene was analyzed by SEC and LLS.

7.2.2 Characterization

Size Exclusion Chromatography

The relative number- and weight-average molar masses ($M_{n,SEC}$ and $M_{w,SEC}$) and the absolute number- and weight-average molar masses ($M_{w.MALLS}$ and

$M_{w,MALLS}$) were determined at 35 °C by size exclusion chromatography (SEC, Waters 1,515) equipped with three Waters Styragel columns (HR2, HR4, HR6), respectively, equipped with a refractive index (RI, Wyatt WREX-02, using a conventional universal calibration with linear polystyrene standards) detector and a multi-angle LLS (MALLS, Wyatt DAWN EOS) detector. Note that SEC measures the weight distribution of hyperbranched chains ($W(M)$ or $C(M)$. The values of M_n and M_w are calculated, respectively, using

$$M_{n,MALLS} = \frac{\sum C_i}{\sum C_i/M_i}, \quad M_{w,MALLS} = \frac{\sum C_i M_i}{\sum C_i} \tag{7.1}$$

THF was used as an eluenting agent at a flow rate of 1.0 mL/min. The MALLS detector uses a GaAs laser (685 nm and 30 mW) and has 18 diodes placed at different angles, ranging from 22.5 to 147.0°. The data were analyzed using ASTRA for Windows software (Ver. 4.90.07, Wyatt). The dn/dC of polystyrene in THF was 0.185 mL/g at 30 °C. For both SEC-RI and SEC-MALLS measurements, 1 mL of polymer solution (2–8 mg/mL, depending on the molar mass) was pre-filtered through a 0.2 μm PVDF filters before injection.

Laser Light Scattering

A commercial LLS spectrometer (ALV/DLS/SLS-5022F) equipped with a multi-τ digital time correlator (ALV5000) and a cylindrical 22 mW UNIPHASE He–Ne laser ($\lambda_0 = 632.8$ nm) as the light source was used. In static LLS, the angular dependence of the absolute excess time-average scattering intensity, known as the Rayleigh ratio $R_{VV}(q)$, can lead to the weight-average molar mass (M_w), the root-mean-square gyration radius ($\langle R_g \rangle$), and the second virial coefficient A_2 by using

$$\frac{KC}{R_{VV}(q)} \cong \frac{1}{M_w}\left(1 + \frac{1}{3}\langle R_g^2 \rangle_Z q^2\right) + 2A_2C \tag{7.2}$$

where $K = 4\pi^2(\mathrm{d}n/\mathrm{d}C)^2/(N_A\lambda_0^4)$ and $q = (4\pi/\lambda_0)\sin(\theta/2)$ with C, dn/dC, N_A, and λ_0 being concentration of the polymer solution, the specific refractive index increment, the Avogadro's number, and the wave length of light in a vacuum, respectively. The extrapolation of $R_{VV}(q)$ to $q \to 0$ and $C \to 0$ leads to M_w. The plot of $[KC/R_{VV}(q)]_{C\to 0}$ versus q^2 and $[KC/R_{VV}(q)]_{q\to 0}$ versus C lead to $\langle R_g \rangle$ and A_2, respectively. In a very dilute solution, the term of $2A_2C$ can be ignored. For relatively small scattering objects, the Zimm plot on the basis of Eq. 7.2 incorporates the extrapolations of $q \to 0$ and $C \to 0$ on a single grid. For long polymer chains, i.e., $q\langle R_g \rangle > 1$, the Berry plot is normally used. In static LLS, the scattering intensity was recorded at each angle three times and each time was averaged over 30 s. The scattering angle ranges from 12 to 120°. The refractive index increment of hyperbranched polystyrenes in toluene (dn/d$C = 0.111$ mL/g at 25 °C and 633 nm) was determined by a precise differential refractometer.

In dynamic LLS, the Laplace inversion of each measured intensity–intensity time correlation function $G^{(2)}(q, t)$ in the self-beating mode can lead to a line-width

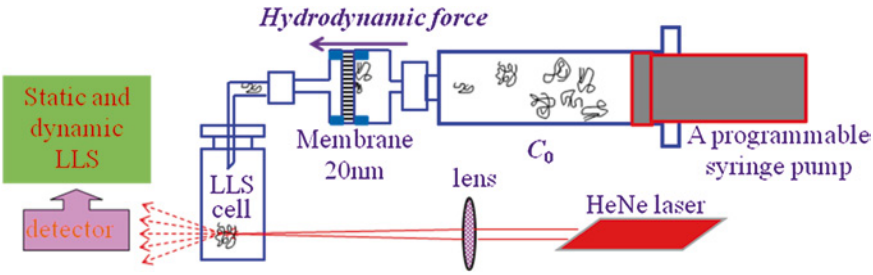

Fig. 7.2 Schematic of ultrafiltration experimental setup

distribution $G(\Gamma)$, where q is the scattering vector. For dilute solutions, Γ is related to the translational diffusion coefficient D by $(\Gamma/q^2)_{q\to 0, C\to 0} \to D$, so that $G(\Gamma)$ can be converted into a transitional diffusion coefficient distribution $G(D)$ or further a hydrodynamic radius distribution $f(R_h)$ via the Stokes–Einstein equation, $R_h = (k_B T/6\pi\eta_0)/D$, where k_B, T and η_0 are the Boltzmann constant, the absolute temperature and the solvent viscosity, respectively. The polydispersity index M_w/M_n was estimated from $M_w/M_n \approx (1 + 4\mu_2/\langle D\rangle^2)$, where $\mu_2 = \int_0^\infty G(D)(D - \langle D\rangle)^2 \mathrm{d}D$. In dynamic LLS experiments, we used a fixed small angle (12°) to ensure that the effect of extrapolating to the zero angle is minimum. The time correlation functions were analyzed by both the cumulants and CONTIN analysis.

Viscosity Measurement

Flow times of polymer solutions were measured using a Ubbelohde capillary viscometer. Relative viscosity (η_r) was obtained from the ratio of the flow times of a solution and the solvent. Before each measurement, a solution in the viscometer was sealed and allowed to equilibrate with a thermostatted water tank for at least 20 min. The temperature fluctuation of the water tank was smaller than 0.1 °C. All samples used for flow time measurements were clarified by filtration through Millipore 0.45 μm PTFE filters. Each polymer solution was measured for three times so that the relative error was less than 0.2 %.

Ultrafiltration

Ultrafiltration membrane (Whatman, Anotop 10), syringe (SGE, 10 mL), holder (Millipore, 13 mm) were assembled as shown in Fig. 7.2. The thicknesses (pore diameters) of the top and bottom layers of ultrafiltration membrane are 59 μm (200 nm) and 1 μm (20 or 100 nm), respectively. The two layers contain a nearly equal number of cylindrical pores; namely, each smaller pore is under a large 200-nm one, which prevents possible interference of the flow fields generated by different small pores at their entrances, i.e., each smaller pore is isolated, so that our study nearly resembles a single pore experiment even many pores are actually used. In each solution, we added an appropriate amount of short linear polystyrene chains with a size smaller than the small pore. They can pass through the small pore by diffusion even without any flow so they served as an internal

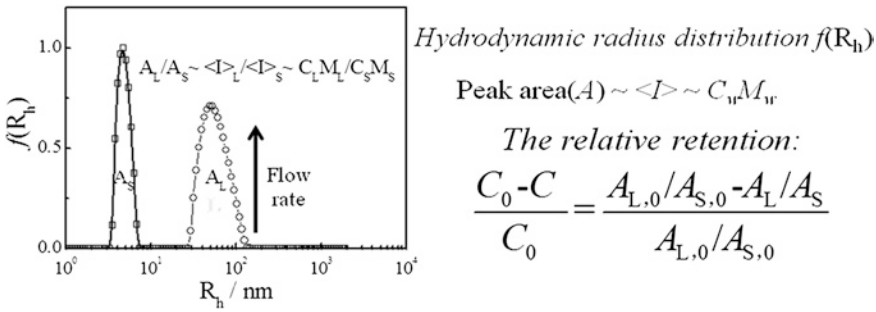

Fig. 7.3 Schematic of characterization of the relative retention concentration $[(C_0 - C)/C_0]$ by dynamic LLS in ultrafiltration experiment

standard. The concentrations of large hyperbranched chains and short linear chains (C_L and C_S) are properly chosen so that the ratio of average light intensity of large and small chains, i.e., $\langle I_L \rangle / \langle I_S \rangle = C_L M_L / C_S M_S \sim 1.5$, where M_L and M_S are the molar masses of hyperbranched and short linear chains, respectively. Note that in dynamic LLS, $\langle I_L \rangle / \langle I_S \rangle$ equals the area ratio of their corresponding peaks in $G(\Gamma)$. Since there is no retention for the short linear chains, a decrease of $\langle I_L \rangle / \langle I_S \rangle$ is related to the retention of large hyperbranched chains, enabling us to calculate their relative retention $[(C_0 - C)/C_0]$ under each flow rate, as shown in Fig. 7.3, where C_0 and C are polymer concentrations before and after the ultrafiltration. The solution temperature and flow rate were controlled by an incubator (Stuart Scientific, S160D) (±0.2 °C) and a syringe pump (Harvard Apparatus, PHD 2000), respectively.

7.3 Experimental Details About Hyperbranched Block Copolymers

7.3.1 Synthesis of Macromonomers and Hyperbranched Polymers

Figure 7.4 schematically shows how linear seesaw-type block copolymer macromonomers with two azide end groups and one middle alkyne group are prepared and "clicked" into large hyperbranched amphiphilic copolymer, hyper-(PAA-PS-PAA)$_n$, after hydrolyzing each tertiary butyl group into a carboxyl group. How to synthesize initiator with one alkyne and two bromine groups was described before. Other synthesis details are outlined as follows.

Synthesis of Uniform Polystyrene Subchain via ATRP

A three-necked flask equipped with a magnetic stirring bar and three rubber septum was charged with initiator (1.0 g, 2.10 mmol), St (24 mL, 210.0 mmol), and PMDETA

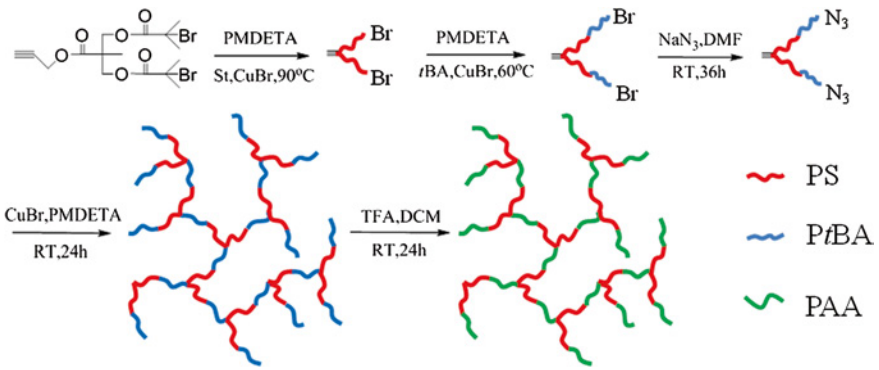

Fig. 7.4 Schematic of synthesis of seesaw type of linear triblock copolymer (macromonomer) and larger hyperbranched amphiphilic copolymers with uniform subchains, hyper-$(PAA\text{-}PS\text{-}PAA)_n$

(435 μL, 2.1 mmol). The flask was degassed by four freeze-pump-thaw cycles, and then placed in an oil bath (90 °C). After ~2 min, CuBr (300 mg, 2.1 mmol) was introduced to start the polymerization under N_2 flow. After a few hours, the flask was cooled and diluted with THF, and passed through a short column of neutral alumina to remove the metal salt. After removing all the solvents by evaporation, the residue was dissolved in THF and precipitated into an excess of methanol. After drying in a vacuum oven overnight at 40 °C, the first PS block with one alkyne and two bromine groups was obtained.

Synthesis of Uniform P*t*BA-PS-P*t*BA Triblock Subchain via ATRP

Into a three-necked flask equipped with a magnetic stirring bar and three rubber septum, linear polystyrene macroinitiator (2.8 g, 1.65 mmol), *t*BA (23.7 mL, 165 mmol), PMDETA(68.7 μL, 0.33 mmol) and acetone (5.93 mL) were charged. The flask was degassed by four freeze-pump-thaw cycles, and then placed in an oil bath thermostated at 60 °C. After ~2 min, CuBr (47.4 mg, 0.33 mmol) was introduced to start the polymerization under N_2 flow. After a few hours, the polymer mixture was cooled and diluted with THF, and then passed through a short column of neutral alumina to remove the metal salt. After removing all the solvents by evaporation, the residue was dissolved in THF and precipitated into a mixture of methanol/water (3/1, v/v). After drying in a vacuum oven overnight at 40 °C, triblock P*t*BA-PS-P*t*BA with one alkyne and two bromine groups was obtained.

Azidation of Triblock Copolymer P*t*BA-PS-P*t*BA

A 100 mL round–bottom flask was first charged with triblock Copolymer P*t*BA-PS-P*t*BA (7.5 g, 0.97 mmol), DMF (30 mL), and NaN_3 (0.63 g, 9.7 mmol). The mixture was allowed to stir at room temperature for 36 h. After removing most of the solvent under reduced pressure, the remaining portion was diluted with CH_2Cl_2,

and then precipitated into a mixture of methanol/water (3/1, v/v). The sediments were dissolved in CH_2Cl_2 and passed through a neutral alumina column to remove the residual sodium salt, and then precipitated into an excess of methanol/water (3/1, v/v). After dried in a vacuum oven overnight at 40 °C, linear seesaw-type triblock Copolymer P*t*BA-PS-P*t*BA with one alkyne and two azide groups was obtained.

Synthesis of Hyperbranched Block Copolymer Hyper-(P*t*BA-PS-P*t*BA)$_n$

A three-necked flask equipped with a magnetic stirring bar and three rubber septum was charged with P*t*BA-PS-P*t*BA macromonomer (7 g, 0.91 mmol), PMDETA (189 μL, 0.91 mmol) and DMF (35 mL). The flask was degassed by four freeze-pump-thaw cycles, and then placed in a water bath thermostated at 35 °C. After ~2 min, CuBr (131 mg, 0.91 mmol) was introduced to start the polycondensation under N_2 flow. After 24 h, the flask was rapidly cooled to room temperature. After removing most of the solvent under reduced pressure, we diluted it with THF, and passed through a short column of neutral alumina to remove the metal salt. After most of the solvents are removed by a rotary evaporator, the residue was precipitated into a mixture of methanol/water (3/1, v/v). After drying in a vacuum oven overnight at 40 °C, hyperbranched block copolymer hyper-(P*t*BA-PS-P*t*BA)$_n$ was obtained.

Fractional Precipitation

Each resultant hyper-(P*t*BA-PS-P*t*BA)$_n$ was fractionated by precipitation as follows. (1) The sample was dissolved in THF at room temperature with a concentration around 0.03 g/mL in a round bottom flask; (2) a mixture of methanol/water (3/1, v/v) was slowly dropped in until the solution became slightly milky; (3) the temperature controlled by a water bath (±0.1 °C) was raised until the solution became clear again; (4) the solution was slowly cooled until it became slightly milky; and (5) the solution temperature was maintained to allow a very small fraction of longest chains to precipitate. The steps 2–5 were repeated to obtain a total of 4 fractions.

Hydrolysis of P*t*BA

Hyper-(P*t*BA-PS-P*t*BA)$_n$ was dissolved in dichloromethane (C ~ 50 g/L) and a 10-fold molar excess of trifluoroacetic acid (TFA) was added. After 24 h, TFA and dichloromethane were removed by a rotary evaporator. The collected polymer was firstly dissolved in 0.5 M Na_2CO_3 solution at 60 °C for 1 h, and then the solution was transferred into presoaked dialysis tubing (MWCO = 3,000 D), dialyzed against deionized water for 5 days. The freeze-drying led to a fluffy white solid.

7.3.2 Characterization

^{1}H nuclear magnetic resonance (NMR) spectra were recorded on a Bruker AV400 spectrometer by using deuterated chloroform ($CDCl_3$) as solvent and tetramethylsilane (TMS) as an internal standard. The relative number- and weight-average

molar masses ($M_{n,RI}$ and $M_{w,RI}$) and the absolute molar masses ($M_{w.MALLS}$ and $M_{w,MALLS}$) were determined at 35 °C by size exclusion chromatography (SEC, Waters 1,515) equipped with three Waters Styragel columns (HR2, HR4, HR6), respectively, equipped with a refractive index detector (RI, Wyatt WREX-02, using a conventional universal calibration with linear polystyrene standards) and a multi-angle LLS detector (MALLS, Wyatt DAWN EOS). THF was used as an eluenting agent at a flow rate of 1.0 mL/min.

Rheological Measurements

Rheological properties were measured with a TA Instruments AR-G2 stress-controlled rheometer. A 40 mm aluminum 1° cone and a Peltier heated plate were used for the oscillatory measurements. The linear viscoelastic regime was established by an oscillatory strain sweep using different frequencies between 0.628 and 628 rad/s. Dynamic strain sweeps were made in the linear regime at 25 °C. The measurement setup was covered with a sealing lid in order to prevent evaporation during the measurement. To prepare samples for rheological measurements, a given amount of freeze-dried hyper-(PAA_{23}-PS_{14}-PAA_{23}) was dissolved in distilled water directly inside a screw capped vial at 80 °C for 10 h in a water bath. After the heating and dissolution, the solution was weighed to correct its concentration for any possible solvent evaporation. The solution was stood at room temperature for 1 day before rheological measurements.

Laser Light Scattering

A commercial LLS spectrometer (ALV/DLS/SLS-5022F) equipped with a multiτ digital time correlator (ALV5000) and a cylindrical 22 mW UNIPHASE He–Ne laser ($\lambda_0 = 632.8$ nm) as the light source was used. In static LLS, the angular dependence of the absolute excess time-average scattering intensity, known as the Rayleigh ratio $R_{VV}(q)$, can lead to the weight-average molar mass (M_w), the root-mean-square gyration radius ($\langle R_g \rangle$) and the second virial coefficient A_2 by using

$$\frac{KC}{R_{VV}(q)} \cong \frac{1}{M_w}\left(1 + \frac{1}{3}\langle R_g^2 \rangle_Z q^2\right) + 2A_2C \tag{7.2}$$

where $K = 4\pi^2(dn/dC)^2/(N_A\lambda_0^4)$ and $q = (4\pi/\lambda_0)\sin(\theta/2)$ with C, dn/dC, N_A, and λ_0 being concentration of the polymer solution, the specific refractive index increment, the Avogadro's number, and the wave length of light in a vacuum, respectively. The extrapolation of $R_{VV}(q)$ to $q \to 0$ and $C \to 0$ leads to M_w. The plot of $[KC/R_{VV}(q)]_{C\to 0}$ versus q^2 and $[KC/R_{VV}(q)]_{q\to 0}$ versus C lead to $\langle R_g \rangle$ and A_2, respectively. In a very dilute solution, the term of $2A_2C$ can be ignored. For our branched and ultra-large hyperbranched polymer chains, i.e., $q\langle R_g \rangle > 1$, the Berry plot is normally used.

In dynamic LLS, the Laplace inversion of each measured intensity–intensity time correlation function $G^{(2)}(q,t)$ in the self-beating mode can lead to a line-width distribution $G(\Gamma)$, where q is the scattering vector. For dilute solutions, Γ is related to the translational diffusion coefficient D by $(\Gamma/q^2)_{q\to 0,C\to 0} \to D$, so that $G(\Gamma)$ can be converted into a transitional diffusion coefficient distribution $G(D)$ or

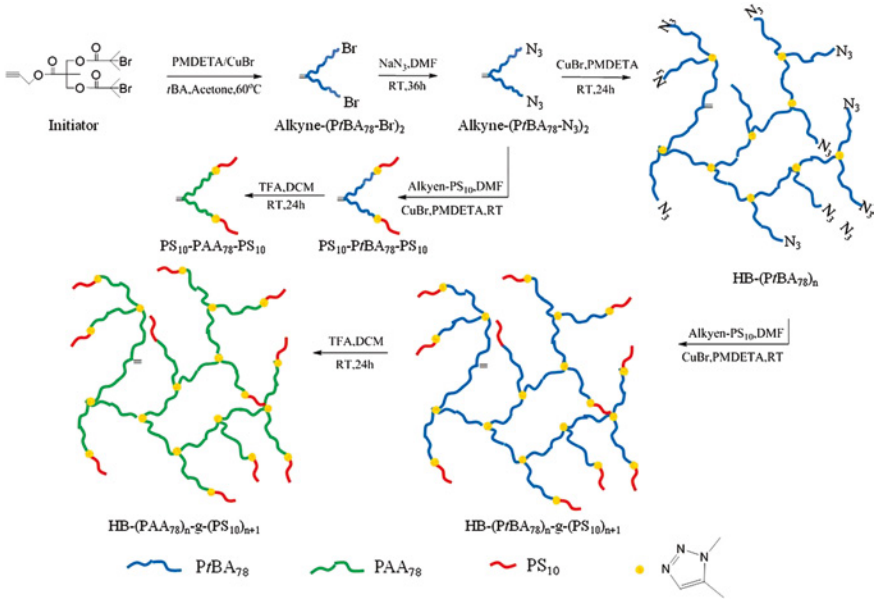

Fig. 7.5 Schematic of synthesis of amphiphilic hyperbranched poly(acrylic acid) grafted with short polystyrene copolymer chains HB-P*t*BA-*g*-PS and HB-PAA-*g*-PS

further a hydrodynamic radius distribution $f(R_h)$ via the Stokes–Einstein equation, $R_h = (k_B T/6\pi\eta_0)/D$, where k_B, T and η_0 are the Boltzmann constant, the absolute temperature and the solvent viscosity, respectively. The time correlation functions were analyzed by both the cumulants and CONTIN analysis.

7.4 Experimental Details About Hyperbranched Graft Copolymers

7.4.1 Synthesis of Macromonomers and Hyperbranched Polymers

Figure 7.5 shows a schematic synthesis of hyperbranched graft copolymers HB-P*t*BA-*g*-PS and HB-PAA-*g*-PS.

Synthesis of Alkyne-(P*t*BA$_{39}$-Br)$_2$ by ATRP

A reaction flask equipped with a magnetic stirrer and a rubber septum was charged with PBMP (0.50 g, 1.05 mmol), *t*BA (13.4 g, 105 mmol), PMDETA (102 μL. 0.52 mmol) and acetone (3.4 g). The flask was degassed by three freeze-pump-thaw cycles and backfilled with N_2, and then placed in an oil bath thermostated at 60 °C. After ~2 min, CuBr (70.3 mg, 0.52 mmol) was introduced to start the

polymerization under N_2 positive pressure. After 8.0 h, the flask was rapidly cooled to room temperature. The polymerization mixture was diluted with THF, and passed through a short column of neutral alumina for the removal of metal salts. After removing the solvents by rotary evaporator, the residue was dissolved in a small amount of THF and precipitated into an excess of cold water/methanol mixture (1/3) twice. After drying in a vacuum oven overnight at 45 °C, alkyne-(P*t*BA$_{39}$-Br)$_2$ was obtained. Yield: 8.0 g (59 %). M_n: 9.30 × 10^3 g/mol and M_w/M_n: 1.08 (by SEC).

Synthesis of Alkyne-(P*t*BA$_{39}$-N$_3$)$_2$ by Azidation Reaction

A 50 mL round–bottom flask was charged with alkyne-(P*t*BA$_{39}$-Br)$_2$ (6 g, 0.57 mmol), DMF (30 mL), and NaN_3 (370 mg, 5.70 mmol). The mixture was allowed to stir at room temperature for 36 h. After removing most of the solvent under reduced pressure, the remaining portion was diluted with CH_2Cl_2, and then precipitated into an excess of cold methanol/water mixture (3/1, v/v). The sediments were re-dissolved in CH_2Cl_2 and passed through a neutral alumina column to remove residual sodium salts, and then precipitated into an excess of cold methanol/water mixture (3/1, v/v). After drying in a vacuum oven overnight at 45 °C, alkyne-(P*t*BA$_{39}$-N$_3$)$_2$ was obtained. Yield: 5.5 g (92 %). M_n: 9.30 × 10^3 g/mol and M_w/M_n: 1.09 (by SEC).

Synthesis of HB-(P*t*BA$_{39}$)$_n$ by "Click" Reaction

The typical procedure is as follows. A three-necked flask equipped with a magnetic stirring bar and three rubber septum was charged with alkyne-(P*t*BA$_{39}$-N$_3$)$_2$ macromonomer (2 g, 0.19 mmol), PMDETA (189 μL, 0.38 mmol) and DMF (5 mL). The flask was degassed by three freeze-pump-thaw cycles, and then placed in a water bath thermostated at 35 °C. After ~2 min, CuBr (54 mg, 0.38 mmol) was introduced to start the reaction under N_2 positive pressure. After 24.0 h, the reaction mixture was cooled to room temperature and diluted with THF, then passed through a short column of neutral alumina to remove the metal salt. After most of the solvents were removed by a rotary evaporator, the residue was precipitated into a mixture of cold methanol/water mixture (3/1, v/v). After drying in a vacuum oven overnight at 40 °C, HB-(P*t*BA$_{78}$)$_{47}$ was obtained. Yield: 1.8 g (90 %). M_n: 2.98 × 10^4 g/mol and M_w/M_n: 6.64 (by SEC). In a similar way, HB-(P*t*BA$_{78}$)$_{10}$ was obtained at the polymer concentration of 0.1 g/L.

Synthesis of Alkyne-PS$_{10}$ by ATRP

A reaction flask equipped with a magnetic stirrer and a rubber septum was charged with the alkyne-functional initiator propargyl 2-bromoisobutyrate (PBIB) (1.00 g, 4.88 mmol), St (10.16 g, 97.6 mmol) and PMDETA (506 μL. 2.44 mmol). The flask was degassed by three freeze-pump-thaw cycles and backfilled with N_2, and then placed in an oil bath thermostated at 90 °C. After ~2 min, CuBr (348 mg, 2.44 mmol) was introduced to start the polymerization under N_2 positive pressure. After 1.0 h, the flask was rapidly cooled to room temperature. The polymer mixture was diluted with THF, and passed through a short column of neutral alumina for the removal of metal salts. After removing the solvents by a rotary evaporator,

the residue was dissolved in a small amount of THF and precipitated into an excess of cold water/methanol mixture (v/v = 1/3) twice. After drying in a vacuum oven overnight at 45 °C, viscous product of alkyne-PS_{10} was obtained. Yield: 4.0 g (40 %). M_n: 9.00 × 10^2 g/mol and M_w/M_n: 1.21 (by SEC).

Synthesis of HB-(P*t*$BA_{78})_n$-*g*-$(PS_{10})_{n+1}$ by "Click" Reaction

The typical procedure is as follows. A reaction flask equipped with a magnetic stirrer and a rubber septum was charged with alkyne-PS_{10} (0.56 g, 0.56 mmol), N_3-functional HB-(P*t*$BA_{78})_{47}$ (1.5 g, ~0.14 mmol N_3 groups), PMDETA (58.3 μL, 0.28 mmol) and DMF (10 mL). The flask was degassed by three freeze-pump-thaw cycles and backfilled with N_2, and then placed in an oil bath thermostated at 35 °C. After ~2 min, CuBr (40.2 mg, 0.28 mmol) was introduced to start the reaction under N_2 positive pressure. After 24.0 h, the flask was cooled to room temperature. The polymer mixture was diluted with THF, and passed through a short column of neutral alumina for the removal of metal salts. After removing the solvents by a rotary evaporator, a mixture of excess alkyne-PS_{10} and target product HB-(P*t*$BA_{78})_{47}$-*g*-$(PS_{10})_{48}$ was obtained. Yield: 1.90 g (92 %). M_n: 4.57 × 10^4 g/mol and M_w/M_n: 6.88 (by SEC).

Synthesis of PS_{10}-P*t*BA_{78}-PS_{10} Triblock by "Click" Reaction

The typical procedure is as follows. A reaction flask equipped with a magnetic stirrer and a rubber septum was charged with alkyne-PS_{10} (2.80 g, 2.8 mmol), alkyne-(P*t*BA_{39}-$N_3)_2$ (0.75 g, ~0.14 mmol N_3 groups), PMDETA (58.3 μL, 0.28 mmol) and DMF (10 mL). The flask was degassed by three freeze-pump-thaw cycles and backfilled with N_2, and then placed in an oil bath thermostated at 35 °C. After ~2 min, CuBr (40.2 mg, 0.28 mmol) was introduced to start the reaction under N_2 positive pressure. After 24.0 h, the flask was cooled to room temperature. The polymer mixture was diluted with THF, and passed through a short column of neutral alumina for the removal of metal salts. After removing the solvents by a rotary evaporator, a mixture of excess alkyne-PS_{10} and target product PS_{10}-P*t*BA_{78}-PS_{10} was obtained. Yield: 3.2 g (90 %). M_n: 1.20 × 10^4 g/mol and M_w/M_n: 1.15 (by SEC).

Synthesis of HB-$(PAA_{78})_n$-*g*-$(PS_{10})_{n+1}$ and PS_{10}-PAA_{78}-PS_{10} Triblock by Hydrolyzing *t*BA into AA Moiety

The typical procedure is as follows. The mixture of alkyne-PS_{10} and target product PS-P*t*BA-PS/HB-(P*t*$BA_{78})_n$-*g*-$(PS_{10})_{n+1}$ obtained in the previous step was dissolved in CH_2Cl_2 (C ~ 100 g/L) and a 5-fold molar excess (*t*BA unit) of trifluoroacetic acid (TFA) was added under N_2 positive pressure. After 36.0 h, TFA and dichloromethane were removed by a rotary evaporator. The collected polymer was firstly dissolved in THF, and then precipitated into cyclohexane three times to remove the residual alkyne-PS_{10}. Finally, the product was dissolved in water/THF mixture (v/v, 5/1) and transferred into dialysis tubing (MWCO = 3,000), and dialyzed against deionized water for 5 days. After the freeze-drying, a fluffy white solid PS_{10}-PAA_{78}-PS_{10}/HB-$(PAA_{78})_n$-*g*-$(PS_{10})_{n+1}$ was obtained.

Emulsion Polymerization

A stock micellar solution of PS_{10}-PAA_{78}-PS_{10} or HB-$(PAA_{78})_n$-g-$(PS_{10})_{n+1}$ copolymer was prepared by directly adding the copolymer into 40 mM Na_2CO_3 aqueous solution at 70 °C for 120 min. Then the solution was weighed to correct its concentration for any possible solvent evaporation. Batch emulsion polymerizations of styrene were performed in a 50 mL three-neck round–bottom flask immersed in a thermostated oil bath and equipped with a reflux condenser, a nitrogen inlet, and a thermometer. The typical procedure is as follows. The micellar solution (27 mL) was bubbled with nitrogen for 20 min at room temperature. Then, 3 g of styrene was added, and after 10 min an aqueous solution of initiator ($K_2S_2O_8$, 0.039 g) in 3 mL of deionized water was introduced to start the polymerization. The emulsion polymerizations were conducted at 70 °C. The reactions were stopped after 4 h to ensure complete conversion.

Characterization of the Latexes

The final latexes were characterized by their polymer solid content τ (g/L) measured by gravimetry and by the average particles radius $\langle R \rangle$ (nm) obtained by dynamic LLS in HCl aqueous solution (pH ~ 3.2). The final latex particle number (N_p) (L^{-1}) was calculated according to

$$N_p = 3\tau / \left(4\pi\rho\langle R\rangle^3\right) \tag{7.3}$$

where ρ is 1.05 g/mL for PS latex particles.

Solubilization Measurement

The typical procedure is as follows. First, 0.1 mL of pyrene anhydrous acetone solution with a concentration of 2.0 g/L was added into a vial. Acetone was allowed to evaporate overnight from the vial, leaving a thin pyrene film inside. Afterwards, 2 mL of PS_{10}-PAA_{78}-PS_{10} (40 mM Na_2CO_3) were transferred to the vials and vigorously stirred at 50 °C for 12 h, and then at room temperature for another 12 h. The excess of pyrene was removed by a 0.45 μm PTFE filter before UV–vis measurement. The concentration of pyrene in the loaded micelles was evaluated by UV-vis spectroscopy.

7.4.2 Characterization

^{1}H nuclear magnetic resonance (^{1}H NMR) spectra were recorded on a Bruker AV400 spectrometer by using deuterated chloroform ($CDCl_3$) as solvent and tetramethylsilane (TMS) as an internal standard. Fourier transform infrared (FT-IR) spectra were recorded on a Bruker VECTOR-22 IR spectrometer. The relative number- and weight-average molar masses (M_n and M_w) were determined at 35 °C by

size exclusion chromatography (SEC, Waters 1,515) equipped with three Waters Styragel columns (HR2, HR4, HR6) and equipped with a refractive index detector (RI, Wyatt WREX-02), using a conventional universal calibration with linear polystyrene standards. THF was used as an eluent at a flow rate of 1.0 mL/min. A commercial LLS spectrometer (ALV/DLS/SLS-5022F) equipped with a multi-digital time correlator (ALV5000) and a cylindrical 22 mW UNIPHASE He-Ne laser ($\lambda_0 = 632.8$ nm) as the light source was employed for dynamic and static laser light scattering (LLS) measurements. In dynamic LLS, scattered light was collected at a fixed angle of 90° for duration of 600 s. Average hydrodynamic radius ($\langle R_h \rangle$) and distribution ($f(R_h)$) were computed using cumulants analysis and CONTIN routines. In static LLS, the scattering intensity was recorded at each angle three times. The dn/dc values of HB-(PtBA)$_n$ in THF was determined as 0.080 mL/g; the dn/dc values of HB-(PAA$_{78}$)$_n$-g-(PS$_{10}$)$_{n+1}$ in 40 mM Na_2CO_3 were 0.190 ($n = 1$), 0.166 ($n = 10$) and 0.158 mL/g ($n = 47$) at 25 °C. Latex particle morphology was observed on a transmission electron microscopy (TEM, JEOL JEM-2100). Before the TEM observation, each latex was directly diluted to ~50 ppm, and then a drop was placed on a carbon-coated copper grid and dried at T = 40 °C in a desiccator. Rheological properties were measured with a TA Instruments AR-G2 stress-controlled rheometer. A 40 mm aluminum 1° cone and a Peltier heated plate were used for the oscillatory measurements (oscillatory strain was set to 1.0 %). The measurement setup was covered with a sealing lid to prevent evaporation during the measurement. To prepare samples for rheological measurements, a given amount of freeze-dried HB-(PAA$_{78}$)$_{47}$-g-(PS$_{10}$)$_{48}$ was dissolved in distilled water (NaOH/COOH = 1/1) directly inside a screw capped vial at 70 °C in a water bath and stirred for 2 h, then the solution was weighed to correct its concentration for any possible solvent evaporation.

7.5 Experimental Details About Hyperbranched Hetero-Subchain Copolymers

7.5.1 Synthesis of Macromonomers and Hyperbranched Polymers

Figure 7.6 shows a schematic synthesis of diblock macromonomer N_3-PS-b-PCL-N_3 and its resultant hyperbranched chain HB-(PS-b-PCL)$_n$.

Preparation of (≡, Br)-PCL-OH by Ring Opening Polymerization (ROP)

0.72 g initiator (2.2 mmol), 7.72 g ε-caprolactone (67.7 mmol) and 0.18 g tin(II)-2-ethylhexanoate (0.4 mmol) were added into a 100 mL three-neck bottle, and then 40 mL anhydrous toluene was added. The mixture was stirred for 5 h at 100 °C under argon atmosphere. Then the solvent was removed by rotary evaporation and the product was redissolved in THF. The polymer solution was precipitated into an excess of the mixture of cold methanol/water (3/1, v/v). White solid (≡, Br)-PCL-OH (7.4 g, Yield ~90 %) was obtained after drying under vacuum for 24 h.

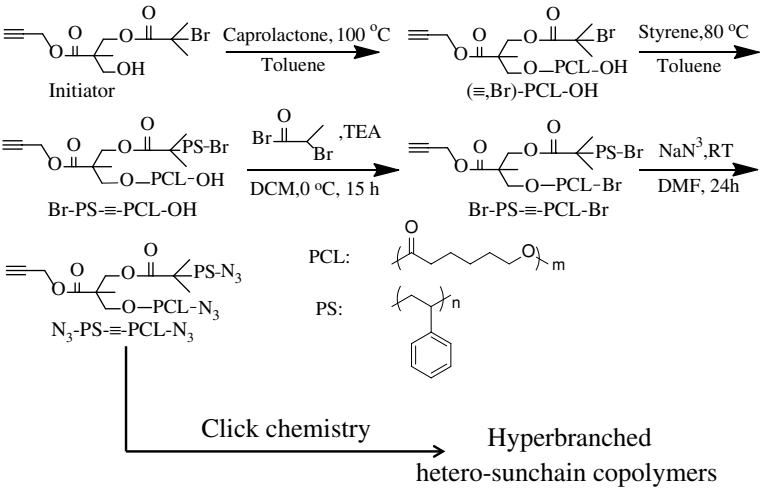

Fig. 7.6 Schematic of synthesis of seesaw-type diblock macromonomer N_3-PS-*b*-PCL-N_3 and an resultant hyperbranched chain HB-(PS-*b*-PCL)$_n$

Preparation of Br-PS-≡-PCL-OH by Atom Transfer Radical Polymerization (ATRP)

1.0 g (≡, Br)-PCL-OH (0.33 mmol), 3.46 g St (33.6 mmol), 31 mg Me_6TREN (0.13 mmol), 54 mg $Sn(EH)_2$ (0.13 mmol) and 2 mL anhydrous toluene were added into a 15 mL glass tube with a magnetic stirrer. After degassed by three freeze-vacuum-thaw cycles, 5 mg CuBr (0.033 mmol) was added into the tube with a hot funnel, then the tube was sealed under vacuum. The mixture was stirred for 1.5 h (or 0.5 h to get smaller PS block) at 80 °C in water bath. Then the tube was rapidly cooled to room temperature. The mixture was diluted with THF and passed through a short neutral alumina column to remove the metal salt. After removing all the solvents by rotary evaporator, the residue was dissolved in THF and precipitated into an excess of the mixture of cold methanol/water (3/1, v/v). White solid Br-PS-≡-PCL-OH (2.1 g, Yield ~88 %) was obtained after drying under vacuum for 24 h.

Preparation of Br-PS-≡-PCL-Br by Bromination Reaction

1.4 g Br-PS-≡-PCL-OH (0.2 mmol), 0.30 g TEA (3 mmol) and 15 mL anhydrous DCM were added into a 50 mL three-neck bottle. 2-Bromopropiomyl bromide 0.63 g (3 mmol) dissolved in 5 mL anhydrous DCM was added dropwise with a constant pressure funnel in 1 h at 0 °C. After 24 h, the solvent was removed. The residue was redissolved in THF. After the removal of insoluble salts by filtration, the filtrate was concentrated by rotary evaporator. The polymer was precipitated into an excess amount of the cold methanol/water mixture (3/1, v/v). Light yellow solid Br-PS-≡-PCL-OH (1.2 g, Yield ~85 %) was obtained after drying under vacuum for 24 h.

Preparation of N_3-PS-≡-PCL-N_3 by Azidation

1.0 g Br-PS-≡-PCL-Br (0.14 mmol), 0.2 g NaN_3 (3.1 mmol) were added into a 50 mL three-neck bottle, and then 18 mL anhydrous DMF was added. The mixture was stirred for 24 h under argon atmosphere at room temperature. After that, the solvent was removed by rotary evaporation and the product was re-dissolved in THF. The polymer solution was precipitated into an excess of the mixture of cold methanol/water (3/1, v/v) after centrifugation. The product N_3-PS-*b*-PCL-N_3 (0.85 g, 86 %) was light yellow power after drying under vacuum overnight.

Preparation of HB-(PS-*b*-PCL)$_n$ by "Click" Reaction

0.1 g N_3-PS-*b*-PCL-N_3 (0.014 mmol), 15 μL PMDETA (0.069 mmol) and 0.5 mL DMF was added into a 2 mL glass tube with a magnetic stirrer. 10 mg CuBr (0.069 mmol) was added into the tube immediately with a hot funnel after degassed by three freeze-vacuum-thaw cycles, and then the tube was sealed under vacuum. The mixture was stirred for 24 h at 60 °C in water bath. After that, the tube was rapidly cooled to room temperature. The mixture was diluted with THF and passed through a short neutral alumina column to remove the metal salt. After removing all the solvents by rotary evaporator, the residue was re-dissolved in THF and precipitated into an excess of the mixture of cold methanol/water (3/1, v/v). White solid HB-(PS-*b*-PCL)$_n$ (68 mg, Yield ~68 %) was obtained after drying under vacuum for 24 h.

7.5.2 Characterization

Proton Nuclear Magnetic Resonance Spectroscopy (^{1}H NMR)

^{1}H NMR spectra of all samples were performed employing a Bruker AV400 NMR spectrometer using $CDCl_3$ as solvent and tetramethylsilane (TMS) as an internal standard. The concentrations of all polymers were 10–20 g/L.

Fourier Transform Infrared Spectroscopy (FT-IR)

FT-IR spectra were performed on a Bruker VECTOR-22 IR spectrometer. The spectra of all samples were collected at 64 scans with a spectral resolution of 4 cm^{-1} by the KBr disk method.

Gel Permeation Chromatography (GPC) with Triple Detectors

The relative number and weight average molar masses ($M_{n,RI}$ and $M_{w,RI}$), the absolute number and weight average molar masses ($M_{n.MALLS}$ and $M_{w,MALLS}$) and the intrinsic viscosity ([η]) were determined at 35 °C by gel permeation chromatography (GPC, Waters 1,515) equipped with three Waters Styragel columns (guard, HR 0.5, HR 1 and HR 4), a Waters 717 PLUS autosampler, a Waters 2,414 differential refractometer, a multi angle laser light scattering (MALLS) detector and a Wyatt ViscoStar viscometer. Tetrahydrofuran (THF) was used as the eluent

at a flow rate of 1.0 mL/min. The specific refractive index increments (dn/dC) of HB-(PS-*b*-PCL)$_n$ copolymers in THF were estimated from the additive rule:

$$\mathrm{d}n/\mathrm{d}C = W_{\mathrm{PS}} \times (\mathrm{d}n/\mathrm{d}C)_{\mathrm{PS}} + W_{\mathrm{PCL}} \times (\mathrm{d}n/\mathrm{d}C)_{\mathrm{PCL}} \tag{7.4}$$

where W_{PS} and W_{PCL} are the weight fractions of PS and PCL and $(\mathrm{d}n/\mathrm{d}C)_{\mathrm{PS}}$ and $(\mathrm{d}n/\mathrm{d}C)_{\mathrm{PCL}}$ in THF are 0.185 and 0.07 mL/g, respectively.

Differential Scanning Calorimeter (DSC)

DSC was performed on a TA Instruments Q2000 differential scanning calorimeter. The samples were prepared by dropping the polymer THF solution onto glass slides and followed by evaporation at room temperature for 24 h. First, the sample was heated to 150 °C to remove the thermal history, and then each sample was reheated after cooling down from 150 to −90 °C at 10 °C/min. The exothermic and the endothermic maximum temperatures were taken as the crystallization temperature (T_c) and the melting temperature (T_m), respectively. The degree of crystallinity (χ_c) is calculated according to the equation as follows:

$$\chi_c = \Delta H_m / \left(W_{\mathrm{PCL}} \times \Delta H_{m,0}\right) \tag{7.5}$$

where ΔH_m is the heat of fusion per gram of copolymers determined based on the endothermic peak. $\Delta H_{m,0} = 136.4$ J/g is the heat of fusion of 100 % crystalline PCL. W_{PCL} is the weight fraction of PCL in the copolymer which was calculated by ^{1}H NMR integral.

Polarizing Optical Microscopy (POM)

The polarizing optical microscopy images were taken by Olympus polarizing microscope with BX51 F system. The film was prepared by dropping the polymer THF solution onto glass slides and followed by evaporation at room temperature for 24 h.

7.6 Experimental Details About Degradable Hyperbranched Homopolymers with Clevable Disulfide Linkages

7.6.1 Synthesis of Macromonomers and Hyperbranched Polymers

Figure 7.7 schematically shows how the Seesaw-type macromonomers and degradable hyperbranched polymers with clevable disulfide linkages are prepared. The detailed synthetic processes are as follows.

Synthesis of Intermediate Compound (I)

The general procedure was outlined as follows. 30.0 g 2,2-bis(hydroxymethyl) propionic acid (223.7 mmol), 41.4 mL 2,2-dimethoxypropane (DMP) (335.4 mmol) and 2.1 g *p*-toluenesulfonic acid monohydrate (*p*-TSA, 11.1 mmol) were dissolved

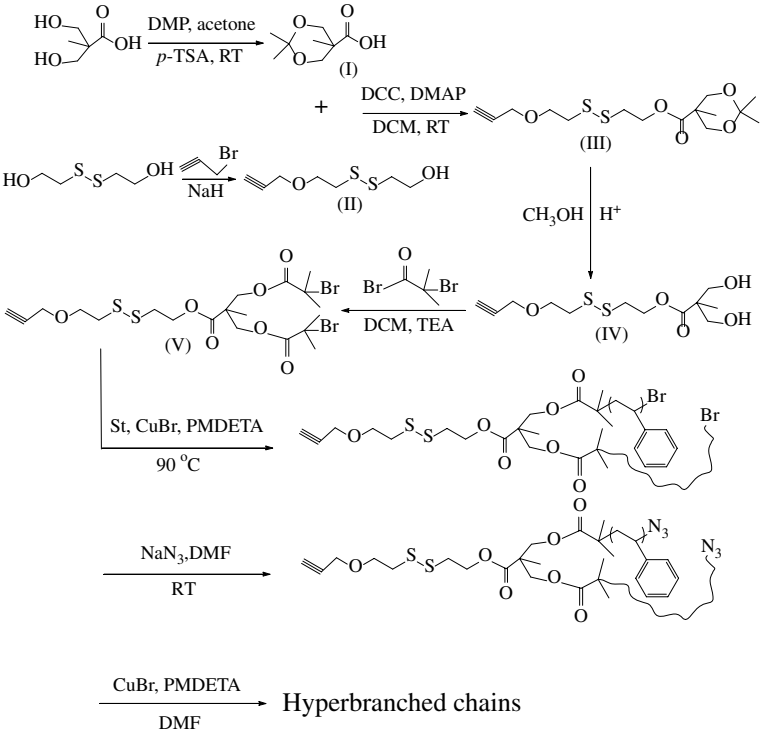

Fig. 7.7 Schematic illustration of the synthesis of disulfide-functionalized seesaw-type polystyrene macromonomer ≡-S-S-(PS-N_3)$_2$ and the resultant hyperbranched polymers

in 100 mL of acetone. The mixture was stirred for 4 h at room temperature before 3.0 mL mixture of an ammonia aqueous solution (25 %) and ethanol (50/50, v/v)) was added into the reaction mixture to neutralize the catalyst. The solvent was removed by evaporation under a reduced pressure at room temperature. The residue was then dissolved in DCM (600 mL) and extracted with two portions of water (80 mL). The organic phase was dried with anhydrous Na_2SO_4 and then evaporated to give white powder (33.0 g, 84 %).

Synthesis of Intermediate Compound (II)

The general procedure was outlined as follows. 20.0 g 2-hydroxyethyl disulfide (130 mmol) and 3.6 g propargyl bromide (65 mmol) were mixed in 200 mL of THF. 3.0 g NaH powder (80 wt%, 98 mmol) was added into the reaction mixture in three successive batches under nitrogen within 3 h at 0 °C. The mixture was further stirred for another 7 h at room temperature before a few drops of water were added to stop the reaction. The mixture was filtrated and the solvent was removed by evaporation under a reduced pressure at 50 °C. The crude product was purified by column chromatography to give a pale-yellow clear oil: 6.5 g (52 %).

Synthesis of Intermediate Compound (III)

The general procedure was outlined as follows. 20.0 g 2-hydroxyethyl disulfide (130 mmol) and 3.6 g propargyl bromide (65 mmol) were mixed in 200 mL of THF. 3.0 g NaH powder (80 wt%, 98 mmol) was added into the reaction mixture in three successive batches under nitrogen within 3 h at 0 °C. The mixture was further stirred for another 7 h at room temperature before a few drops of water were added to stop the reaction. The mixture was filtrated and the solvent was removed by evaporation under a reduced pressure at 50 °C. The crude product was purified by column chromatography to give a pale-yellow clear oil: 6.5 g (52 %).

Synthesis of Intermediate Compound (IV)

The general procedure was outlined as follows. 8.0 g compound (III) (25.0 mmol) dissolved in 100 mL of methanol was added with an excess of activated acidic styrene cation exchange resin (amberlite IR-120, Aladdin). The mixture was stirred for 4 h at room temperature. After the resin was filtrated, the solvent was removed by evaporation. The crude product was purified by column chromatography to give a pale-yellow oil: 7.1 g (89 %).

Synthesis of Compound (V), Seesaw-type initiator

The general procedure was outlined as follows. 6.5 g compound (IV) (21.1 mmol) and 2.6 g TEA (25.3 mmol) were dissolved in 150 mL of DCM. 11.6 g α-bromoisobutyryl bromide (50.6 mmol) dissolved in 50 mL of DCM was added into the reaction mixture under nitrogen flow at 0 °C within 0.5 h. The mixture was stirred overnight. After filtration, the mixture was diluted with 100 mL of DCM and extracted with 50 mL of saturated sodium bicarbonate aqueous solution. The organic phase was dried with anhydrous sodium sulfate. After removing the solvent by evaporation, the crude product was purified by column chromatography to give a dark-yellow oil: 9.0 g (71 %).

Preparation of Macromonomer ≡-S-S-(PS-Br)$_2$ by ATRP

The general procedure was outlined as follows. A three-necked flask equipped with a magnetic stirring bar and three rubber septa was charged with 0.4 g initiator (**V**) (0.66 mmol), 12.1 mL styrene (105.9 mmol) and 124 μL PMDETA (0.66 mmol). The flask was degassed by three freeze-pump-thaw cycles, and then placed in an oil bath thermostated at 90 °C. After ~2 min, 93.7 mg CuBr (0.66 mmol) was added under nitrogen flow to start the polymerization. Samples were withdrawn at different times during the polymerization for SEC and monomer conversion measurements by weighing method. After a few hours, the flask was rapidly cooled in liquid nitrogen. The polymer mixture was diluted with THF, and passed through a short column of neutral alumina to remove metal salt. The solvent was removed by evaporation, and the residue was dissolved in THF and precipitated into an excess of methanol and recovered by filtration. The above purification cycle was repeated twice. After drying in a vacuum oven overnight at

40 °C, macromonomer ≡-S-S-(PS-Br)$_2$ was obtained. Yield: 6.15 g (54 %). M_n: 9.4 × 10^3 g/mol and M_w/M_n: 1.14 (by SEC); M_n: 9.0 × 10^3 g/mol.

Preparation of Macromonomer ≡-S-S-(PS-N$_3$)$_2$ by Azidation

The general procedure was outlined as follows. A 100 mL round–bottom flask was charged with 5.0 g ≡-S-S-(PS-Br)$_2$ (0.45 mmol), 40 mL DMF, and 0.29 g sodium azide (4.5 mmol). The mixture was allowed to stir at room temperature for 24 h under nitrogen flow. After removing DMF under a reduced pressure, the remaining portion was diluted with DCM and passed through a neutral alumina column to remove residual sodium salts. The solvent was removed by evaporation, and the residue was dissolved in THF and precipitated into an excess of methanol. After drying in a vacuum oven overnight at 40 °C, azido-terminated polymer was obtained and named as ≡-S-S-(PS-N$_3$)$_2$. Yield: 4.7 g (94 %). M_n: 9.3 × 10^3 g/mol and M_w/M_n: 1.12 (by SEC).

Preparation of Degradable Hyperbranched Polymer HB-(S-S-PS)$_n$ by "Click" Chemistry

The general procedure was outlined as follows. A 25 mL three-necked flask equipped with a magnetic stirring bar and three rubber septa was charged with 4.5 g macromonomer ≡-S-S-(PS-N$_3$)$_2$ (~0.43 mmol, $M_{w,macromonomer}$ = 1.04 × 10^4 g/mol), 83 μL PMDETA (0.40 mmol) and 15.0 mL DMF. The flask was degassed by three freeze-pump-thaw cycles, and then placed in a water bath thermostated at 35 °C. After ~2 min, 57.5 mg CuBr (0.40 mmol) was added under nitrogen flow to start the polymerization. Samples were withdrawn at different times and precipitated into a mixture of methanol/water (90/10, v/v) for SEC measurements. After 24 h, the flask was cooled in liquid nitrogen. The polymer mixture was diluted with THF, and passed through a short column of neutral alumina for the removal of metal salt. The solvent was removed by evaporation, and the residue was dissolved in THF and precipitated into an excess of methanol. After drying in a vacuum oven overnight at 40 °C, hyperbranched polymer HB-(S-S-PS)$_n$ was obtained. The resultant polydispersed HB-(S-S-PS)$_n$ was further purified by fractional precipitation in a mixed solution of toluene/methanol to remove most of the low-molar-mass-fractions. Finally, hyperbranched HB-(S-S-PS)$_n$ fraction with a M_w of ~3.7 × 10^5 g/mol ($n \simeq 35$) was obtained and used in the degradation kinetics study.

DTT-induced Degradation of HB-(S-S-PS)$_{35}$ Chains

The DTT-induced degradation of HB-(S-S-PS)$_{35}$ was conducted in situ inside the LLS cuvette. Stock DMF solutions of HB-(S-S-PS)$_{35}$ (1.0 g/L) and DTT (25.0 g/L) were purged by nitrogen to replace oxygen and respectively clarified with 0.45 μm Millipore PTFE filters to remove dust. In a typical experiment, a proper amount of dust-free DTT DMF solution was rapidly added into 3.0 mL of dust-free HB-(S-S-PS)$_{35}$ DMF solution to start the degradation. Both the scattered intensity and $G^{(2)}(q, t)$ were recorded during the degradation for at least 1,000 min.

7.6.2 Characterization

^{1}H nuclear magnetic resonance (^{1}H NMR) spectra were recorded using a Bruker AV400 spectrometer with tetramethylsilane (TMS) as an internal standard and deuterated chloroform ($CDCl_3$) as solvent. Fourier transform infrared spectra (FTIR) were recorded using a Bruker VECTOR-22 IR spectrometer and each spectrum was collected over 64 scans with a spectral resolution of 4 cm^{-1}.

Size Exclusion Chromatography (SEC)

The relative number- and weight-average molar masses ($M_{n,RI}$ and $M_{w,RI}$), and the absolute number- and weight-average molar masses ($M_{n.MALLS}$ and $M_{w,MALLS}$) were determined at 35 °C by size exclusion chromatography (SEC, Waters 1,515) equipped with three Waters Styragel columns (HR2, HR4 and HR6), a refractive index detector (RI, Wyatt WREX-02) and a multi-angle laser light scattering detector (MALLS, Wyatt DAWN EOS). THF was used as the eluent at a flow rate of 1.0 mL/min and linear narrowly distributed polystyrenes were used as standards.

Laser Light Scattering

A commercial LLS spectrometer (ALV/DLS/SLS-5022F) equipped with a multi-τ digital time correlator (ALV5000) and a cylindrical 22 mW UNIPHASE He–Ne laser ($\lambda_0 = 632.8$ nm) was used as the light source. In static LLS, the angular dependence of the absolute excess time-average scattering intensity, known as the Rayleigh ratio $R_{VV}(q)$, can lead to the weight-average molar mass (M_w), the root-mean-square gyration radius ($\langle R_g \rangle$) and the second virial coefficient A_2 by using

$$\frac{KC}{R_{VV}(q)} \cong \frac{1}{M_w}\left(1 + \frac{1}{3}\langle R_g^2\rangle_Z q^2\right) + 2A_2C \tag{7.2}$$

where $K = 4\pi^2 n^2 (\mathrm{d}n/\mathrm{d}C)^2/(N_A\lambda_0^4)$ and $q = (4\pi n/\lambda_0)\sin(\theta/2)$ with n, C, $\mathrm{d}n/\mathrm{d}C$, N_A, and λ_0 being the refractive index, the concentration of the polymer solution, the specific refractive index increment, the Avogadro's number, and the wavelength of light in a vacuum, respectively.

In dynamic LLS, the Laplace inversion of each measured intensity–intensity time correlation function $G^{(2)}(q, t)$ in the self-beating mode can result in a line-width distribution $G(\Gamma)$. $G(\Gamma)$ can be converted into a translational diffusion coefficient distribution $G(D)$ or further a hydrodynamic radius distribution $f(R_h)$ via the Stokes–Einstein equation, $Rh = (kBT/6\pi\eta_0)/D$, where kB, T and η_0 are the Boltzmann constant, the absolute temperature and the solvent viscosity, respectively. The time correlation functions were analyzed by both the cumulants and CONTIN analysis.